Adhesion

a sticky way of understanding Large Scale Structure

Johan Hidding
Supervisor: Rien van de Weijgaert

July 26, 2010

Contents

List of Figures

Chapter 1

Introduction

The story of the Big Bang has many sides. It is not only the Story of the creation of Life, the Universe and Everything; it is also one of the greatest success stories of science in the twentieth century and it sets the stage on which the formation of structure in the Universe plays its part.
Questions on the origin of structure have haunted many a philosopher, but since developments in quantum mechanics have shaken our understanding of causality, this theory serves us well in finding answers to these questions. Tiny quantum fluctuations were blown out of proportion by cosmic inflation during the first moments after the Big Bang. By gravitational interaction these fluctuations then grew to become the structures we now find our selves embedded in. It is our mission to describe this process. Current observations show us both ends of the pipeline, but relatively little of what is in between. Moreover, the largest agent of gravitational collapse, dark matter, is also the largest unknown.
At the one end we see the *cosmic microwave background* radiation (fig. 1.1), which shows the conditions of the Universe only 340000 years after the Big Bang.
At the other end we can look at the distribution of galaxies as it is now (or up-to a few billion years in the past). In figure 1.2 we see a slice of the Sloan survey. In this image we see a web-like structure consisting of clusters interwoven by filaments and walls, leaving vast volumes of empty space: the voids. This structure we call the *Cosmic Web*. (van de Weygaert and Bond, 2005a,b)
Knowing the statistics of the conditions in the Universe at the time of recombination, given the right physics, we should be able to derive the statistics of the cosmic web. However, even if we knew the right physics, this problem is mathematically very hard.
One way to treat this problem is to run N-body simulations of which we see a famous example in figure (1.3). The results can then be compared to obser-

Figure 1.1: WMAP 5 year CMB temperature anisotropy map: The fluctuations are of the order of a ten thousandth of a degree. This is the fingerprint of the pristine condition the Universe was in when it was only 340000 years old. (Komatsu et al., 2009) Source: `http://lambda.gsfc.nasa.gov/`

vations. Even though the structures found largely agree with what we see in surveys, the simulations don't get it quite right. Despite the immense difficulties in either measuring dark matter halo properties in real galaxies, or putting virtual galaxies inside simulated haloes, there are numerous inconsistencies.

There is to much substructure in the simulations. Galaxies should be populated by numerous dark matter sub-haloes, and should be accompanied with a large body of satellite dwarfs. These dwarfs are not seen in the numbers predicted by the N-body simulations (Klypin et al., 1999). A possibly related problem is that voids seem to be more empty than seen in simulations (Peebles, 2001). Dark matter halo profiles have a sharp cusp in simulations, while observations suggest that the profile should show a cut-off (Navarro et al., 1996; de Blok, 2010). Furthermore it is unknown how galaxies get there angular momentum. (Perivolaropoulos 2008 gives a review of several problems in ΛCDM cosmology.)

To understand where these discrepancies come from, we need both analytic and heuristic models. The theory of the cosmic web describes how small perturbations grow into the different morphological structures we observe today. What property of the initial conditions at one location made it a cluster, and at another a filament? Given this problem, the theory of adhesion can be useful in several distinct ways.

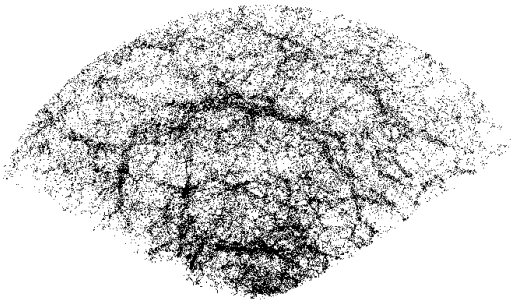

Figure 1.2: Slice from SDSS: Numerous surveys have mapped the distribution of galaxies in our neighbourhood. One of the most famous is the Sloan Digital Sky Survey, of which a slice is shown above. We can clearly see in this picture the foam like structure of the distribution of galaxies. (Abazajian et al., 2009)

1.1 Goals of this project

Given the output of an N-body code, we need to be able to detect and classify the structures that we have no trouble spotting with our own eyes. Numerous algorithms exist that detect voids, filaments and clusters (Platen et al., 2007; Aragón-Calvo et al., 2007a; Aragon-Calvo et al., 2010). These have to be tested against a sample of which the morphological composition is known beforehand. This can be done using the Voronoi model. A more versatile option is to use the adhesion model to this end. Adhesion is a first order non-linear method to approximate the early stages of gravitational instability.

The theory of the Cosmic Web tries to predict the presence of morphological structures directly from the initial conditions. The main tools to achieve this (Press-Schechter, peak-patch and others) are of a local character. They study several properties of the initial conditions filtered at different scales. Adhesion is probably the simplest approximation that incorporates the global evolution of the Cosmic Web. As such it can serve to test these tools as well as giving a physical interpretation to approximations that often are of a highly abstract nature.

Third, since adhesion is physically very simple, yet relatively accurate, we can see whether we can reproduce results from N-body simulations. This would eliminate possible explanations from more elaborate physics.

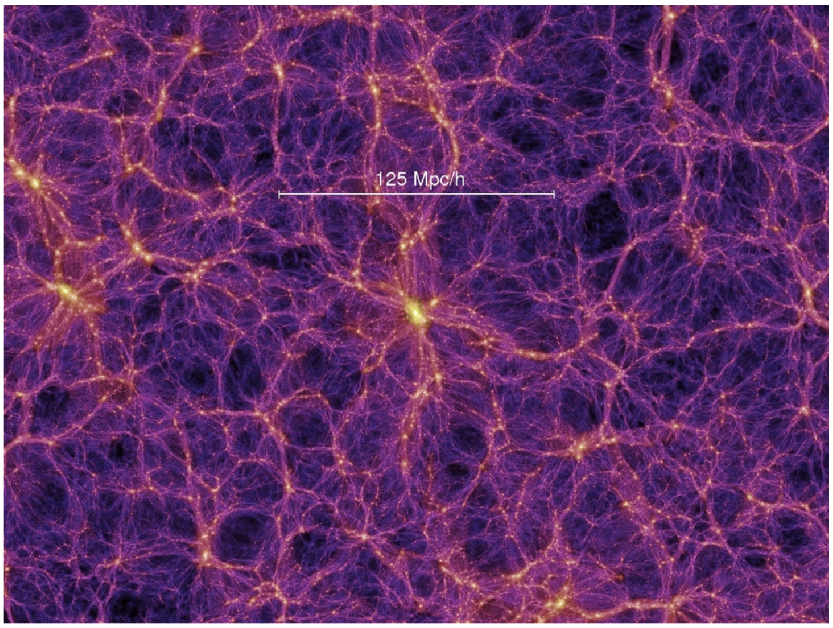

Figure 1.3: Slice from the Millennium simulation: (Springel et al. 2005). We clearly see the same foam-like structure as in figure (1.2).

1.2 Outline

This work is organised in eight chapters. We start by giving a qualitative narrative of the subject, after which we dive into the theory of LSS. In chapter 3 & 4 we will abstract more and more into the realm of a solid theoretical framework applied to some toy models. Chapter 5 covers the numerical techniques in detail. In chapter 6 we treat the qualitative aspects of the dynamics of the cosmic web, folowed by a more quantitative study for different initial conditions. We wrap up discussing the possibilities and limitations of the model. Note that nearly all equations and derivations are written down for the three dimensional model. It is however often more instructive to illustrate the concepts in one or two dimensions.

Chapter 2

Theory of modern cosmology and large scale structure

We start with a concise introduction to LSS making the reader familiar with important quantities, as well as giving a derivation of the most important equations. This section can be skipped if the reader is already familiar with the subject; conventions are summarised in the appendix.

2.1 Standard cosmology

For a science trying to describe the dynamics of the entire Universe, standard cosmology has surprisingly little ingredients.

Most of the equations we work with, ultimately derive from the theory of general relativity, which describes gravitational interaction. Though it should be emphasised that the Newtonian equations suffice for deriving all of the equations we use in this project.

We assume the cosmological principle which states that the Universe is homogeneous and isotropic on the largest scales. There is a large body of evidence that this is a correct assumption, including cosmic gamma-ray bursts, the microwave background and quasar surveys. The standard model of particle physics describes the other three fundamental forces, that is, the electromagnetic, weak nuclear, and strong nuclear force.

The previous ingredients form what we could call *classical cosmology*, which suffers from a number of problems that are elegantly solved by having the Universe undergo a period of very rapid expansion called inflation. From these ingredients we need to make two basic assumptions with respect to the formation of structure. The main process responsible for the formation

of structure is gravitational instability. The density perturbations that initiate this instability are small and Gaussian, as can be derived from inflation.
The geometry of the Universe is described by the Robertson-Walker metric

$$ds^2 = c^2dt^2 - a^2(t)\left(dr^2 + S_k^2\left(\frac{r}{R_0}\right)d\Omega^2\right) \tag{2.1}$$

where

$$S_k\left(\frac{r}{R_0}\right) = \begin{cases} \sin\left(\frac{r}{R_0}\right) & (k=1) \\ \frac{r}{R_0} & (k=0) \\ \sinh\left(\frac{r}{R_0}\right) & (k=-1) \end{cases}$$

and R_0 is the curvature radius at present time.
The expansion of the Universe is described by the Friedman equations

$$\left(\frac{\dot{a}}{a}\right)^2 = \frac{8\pi G}{3}\rho(t) - \frac{kc^2}{R_0^2}\frac{1}{a(t)^2} + \frac{\Lambda c^2}{3} \tag{2.2}$$

$$\frac{\ddot{a}}{a} = -\frac{4\pi G}{3}\left(\rho(t) + \frac{3p}{c^2}\right) + \frac{\Lambda c^2}{3} \tag{2.3}$$

which can be derived from the Einstein equation. The precise way the Universe evolves depends on the different constituents that make up the cosmic inventory, each with it's own equation of state

$$P = w\rho c^2$$

One of the more important numbers that we need is the *critical density*

$$\rho_{\text{crit}} = \frac{3H_0^2}{8\pi G} = 5.5 \times 10^{41}\frac{h^2\text{kg}}{\text{Mpc}^3}$$

Which is roughly equal to the mass of the Galaxy per cubic Mpc.
The Friedman equations in case of 'dust' are easily derived from the Poisson and continuity equations. Often these equations are written in terms of $H = \dot{a}/a$ and

$$\Omega = \rho/\rho_{\text{crit}} = \frac{8\pi G}{3H_0^2}\rho$$

which are measurable quantities. The first Friedman equation can be rewritten as

$$\left(\frac{H}{H_0}\right)^2 = \Omega_r a^{-4} + \Omega_m a^{-3} + \Omega_c a^{-2} + \Omega_\Lambda$$

Where Ω_i are the different energy components of the Universe.

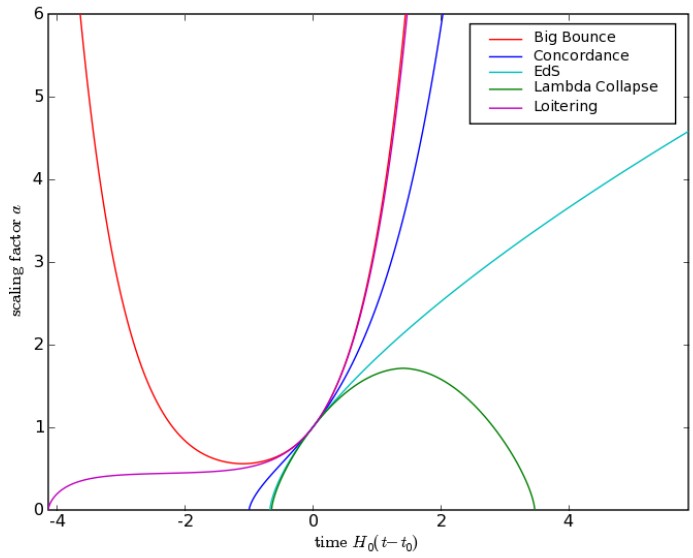

Figure 2.1: Scale factor: Solutions to the Friedman equation. The Friedman equation allows for many types of solutions, depending on the energy contents of the Universe.

2.2 Concordance model

There are several key observations that led to the current picture of the Big Bang. The CMB anisotropy (Komatsu et al., 2009), large scale clustering (Eisenstein et al., 2005), Big Bang nucleosynthesis (Schramm and Turner, 1998), and measurement of distant supernovae (Riess et al., 1998; Perlmutter et al., 1999) consistently point to a model with flat space-time curvature, a dominant 70% dark energy contribution and only 30% matter of which 4% baryonic. The other 26% matter is hypothesised to be *cold dark matter*. This unknown substance should be nearly pressureless, and have small velocity dispersion (hence cold). It is the main agent of gravity in our Universe.

2.3 Co-moving coordinates and density perturbation

Structure forms on the background of a homogeneous and expanding universe. This background is described by the Friedman equation and is the part that we're *not* interested in for the moment. This is why we separate the Friedman equation out of those of LSS. That is, we assume this separation to

be possible and neglect possible effects of inhomogeneities on the FRW universe. Recently several papers have been published that argue the inverse of this assumption, the presence of a *cosmic back-reaction* (Clifton et al., 2008), even so the effect should be negligible for our purpose. Inhomogeneities are then described by the density perturbation

$$1 + \delta(\boldsymbol{x}) \equiv \frac{\rho(\boldsymbol{x})}{\bar{\rho}}. \tag{2.4}$$

Also we would like to describe everything in coordinates that are independent of the Hubble expansion. This is done using *co-moving coordinates*

$$\boldsymbol{r} \equiv a\boldsymbol{x}, \tag{2.5}$$

where $\boldsymbol{r}$ are the physical and $\boldsymbol{x}$ the comoving coordinates. This also affects the derivative

$$\boldsymbol{\nabla}_r = \frac{\boldsymbol{\nabla}_x}{a}. \tag{2.6}$$

These two transformations will lead to basic equations that look slightly different from their more familiar counterparts. But first we have to define some new quantities.
If we look at physical velocity in terms of comoving coordinates

$$\boldsymbol{u} = \dot{r} = a\dot{\boldsymbol{x}} + \dot{a}\boldsymbol{x} = \boldsymbol{v} + \boldsymbol{v}_{\mathbf{H}}$$

We see that we can separate into peculiar velocity $\boldsymbol{v}$ and Hubble flow.

$$\boldsymbol{v} \equiv a\dot{\boldsymbol{x}}. \tag{2.7}$$

To move from standard gravitational potential to a perturbation, we need to subtract the global contribution from the potential.

$$\ddot{a}\boldsymbol{x} = -\frac{\boldsymbol{\nabla}_x}{a}\Phi_u,$$

$$\Phi_u = -\frac{1}{2}a\ddot{a}x^2,$$

thus the potential perturbation is given by

$$\phi \equiv \Phi + \frac{1}{2}a\ddot{a}x^2. \tag{2.8}$$

The peculiar acceleration is defined as

$$\boldsymbol{g}(\boldsymbol{x}, t) \equiv -\frac{\boldsymbol{\nabla}_x \phi}{a}. \tag{2.9}$$

Let's say the physical acceleration comes from a universal contribution $\ddot{a}\boldsymbol{x}$ together with the peculiar acceleration.

$$\ddot{\boldsymbol{r}} = \ddot{a}\boldsymbol{x} + 2\dot{a}\dot{\boldsymbol{x}} + a\ddot{\boldsymbol{x}} = \ddot{a}\boldsymbol{x} + \boldsymbol{g}(\boldsymbol{x}, t),$$

and

$$\dot{\boldsymbol{v}} = \dot{a}\dot{\boldsymbol{x}} + a\ddot{\boldsymbol{x}},$$

then

$$\boldsymbol{g}(\boldsymbol{x}, t) = \frac{1}{a}\frac{d(a\boldsymbol{v})}{dt}. \tag{2.10}$$

2.4 Initial conditions

We know from the CMB that the early universe can be accurately described as a *Gaussian random field* (Komatsu et al., 2003). This has been predicted by inflation theories (Guth, 1981; Linde, 1982), but can also be justified using the central limit theorem.
Given a field with m points, having coordinates $\boldsymbol{x}_1, \boldsymbol{x}_2, \ldots \boldsymbol{x}_m$, and values $f_1, f_2, \ldots f_m$. A Gaussian random field has all of its statistical properties described by the means $\langle f_i \rangle$ and the covariance matrix $M_{ij} \equiv \langle \Delta f_i \Delta f_j \rangle$, where $\Delta f_i \equiv f_i - \langle f_i \rangle$. The covariance matrix can be seen as a multidimensional extension of the standard deviation σ. The joint probability that the value at $\boldsymbol{x}_i$ lies in the interval $[f_i, f_i + df_i]$ is given by the multivariate Gaussian

$$P(f_1, \ldots f_m) df_1 \ldots df_m = \frac{\exp\left[1/2 \ \sum_i \sum_j \ \Delta f_i \ (M^{-1})_{ij} \ \Delta f_j\right]}{\sqrt{(2\pi)^m \det(M)}} df_1 \ldots df_m. \tag{2.11}$$

We have defined the density perturbation to have $\langle \delta \rangle = 0$ and using the added knowledge of isotropy and homogeneity,

$$M_{ij} = \langle \delta(\boldsymbol{x}_i)\delta(\boldsymbol{x}_j) \rangle \equiv \xi(|\boldsymbol{x}_j - \boldsymbol{x}_i|), \tag{2.12}$$

where $\xi(r)$ is the *two-point correlation function*.
It is often convenient to express density fields in Fourier space

$$\hat{f}(\boldsymbol{k}) = \int d\boldsymbol{x} f(\boldsymbol{x}) e^{i\boldsymbol{k}\cdot\boldsymbol{x}} \tag{2.13}$$

$$f(\boldsymbol{x}) = \int \frac{d\boldsymbol{k}}{(2\pi)^3} \hat{f}(\boldsymbol{k}) e^{-i\boldsymbol{k}\cdot\boldsymbol{x}} \tag{2.14}$$

We find the *power spectrum* to be the Fourier transform of the two-point correlation function,

$$\xi(r) = \int \frac{d^3\boldsymbol{k}}{(2\pi)^3} P(k) e^{i\boldsymbol{k}\cdot\boldsymbol{r}}, \tag{2.15}$$

where

$$\langle \hat{\delta}(\boldsymbol{k}) \hat{\delta}^*(\boldsymbol{k}') \rangle = (2\pi)^3 P(\boldsymbol{k}) \delta_D(\boldsymbol{k} - \boldsymbol{k}') \tag{2.16}$$

Again because of homogeneity, in Fourier space the phases need to be uniformly random and the moduli should be Rayleigh-distributed. This means the imaginary and real part are independent and Gaussian-distributed with $\sigma^2 = P(k)$.
In this study we will use pure power-law, as well as CDM power spectra. A pure power-law power spectrum is given by

$$P(k) = Ak^n. \tag{2.17}$$

Whereas a CDM power spectrum includes a transfer function representing post-inflation physics:

$$P(k) = AT^2(k)k^n. \tag{2.18}$$

Throughout this project we use the transfer function by Bardeen et al. (1986), which is an analytic fit to numerical simulations solving the Boltzmann equation.

$$T_{\mathrm{CDM}} = \frac{\ln(1+2.34q)}{2.34}\left[1+3.89q+(16.1q)^2+(5.46q)^3+(6.71q)^4\right]^{-\frac{1}{4}}, \tag{2.19}$$

where $q = k/\Omega h^2$.

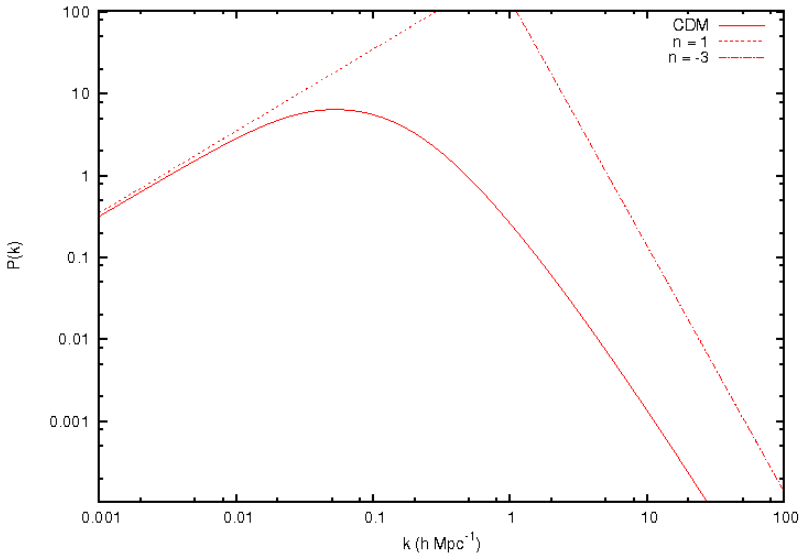

Figure 2.2: CDM power spectrum: the CDM power spectrum as given in BBKS. In the limits of $k \to 0$ the slope tends to $n = 1$, whereas in the limit to infinity (smallest scales) it behaves as a power law with $n = -3$.

The convention is to normalise the power spectrum using the linearly extrapolated value of σ_8.

$$\sigma_8 = \left[\int_0^\infty dk 4\pi k^2 P(k) \hat{W}_{\mathrm{TH}}^2(k) \right]^{1/2}, \tag{2.20}$$

where $\hat{W}_{\mathrm{TH}}$ is the Fourier transform of a spherical top-hat function of radius $R = 8\ h^{-1}$ Mpc

$$\hat{W}_{\mathrm{TH}}(k) = \frac{3(\sin 2\pi kR - 2\pi kR \cos 2\pi kR)}{(2\pi kR)^3}. \tag{2.21}$$

A standard choice is $\sigma_8(t_0) \approx 1$. To normalise the initial conditions this value is extrapolated linearly as $\sigma_8(t) = D_+ \sigma_8(t_0)$. Where D_+ is the growing mode solution (see section 2.6).

2.5 Equations of motion

We start with the standard Newtonian fluid equations describing the evolution of the matter distribution in the Universe.

$$\nabla_r^2 \Phi = 4\pi G\rho \qquad \text{Poisson} \tag{2.22}$$

$$\frac{d\boldsymbol{u}}{dt} = -\frac{\boldsymbol{\nabla}_r p}{\rho} - \boldsymbol{\nabla}_r \Phi \qquad \text{Euler} \tag{2.23}$$

$$\frac{d\rho}{dt} = -\rho \boldsymbol{\nabla}_r \cdot \boldsymbol{v} \qquad \text{Continuity} \tag{2.24}$$

In comoving coordinates these are transformed to a very similar form (see appendix).

$$\nabla_x^2 \phi = 4\pi G a^2 \bar{\rho} \delta \qquad \text{Poisson} \tag{2.25}$$

$$\frac{d\boldsymbol{v}}{dt} + \frac{\dot{a}}{a}\boldsymbol{v} = -\frac{\boldsymbol{\nabla}_x}{a}\phi \qquad \text{Euler} \tag{2.26}$$

$$\frac{d\delta}{dt} + (1+\delta)\frac{\boldsymbol{\nabla}_x}{a}\boldsymbol{v} = 0 \qquad \text{Continuity} \tag{2.27}$$

The most important change is the term $H\boldsymbol{v}$ in the Euler equation. It is known as the *Hubble drag*.

2.6 Linear theory

The set of derived equations is non-linear in two respects

- there is a cross-term of $\boldsymbol{\nabla}\delta\boldsymbol{v}$ in the continuity equation
- $(\boldsymbol{v}\cdot\boldsymbol{\nabla})\boldsymbol{v}$ in the Euler equation is higher order.

To get rid of these we assume $|\delta| \ll 1$ and $(\boldsymbol{v}\cdot\boldsymbol{\nabla})\boldsymbol{v}$ be negligible. Then we are left with the set of linearised equations

$$\nabla^2\phi = 4\pi G\bar{\rho}a^2\delta \qquad \text{Poisson} \tag{2.28}$$

$$\dot{\boldsymbol{v}} + \frac{\dot{a}}{a}\boldsymbol{v} = -\frac{1}{a}\boldsymbol{\nabla}\phi \qquad \text{Euler} \tag{2.29}$$

$$\dot{\delta} + \frac{1}{a}\boldsymbol{\nabla}\cdot\boldsymbol{v} = 0 \qquad \text{Continuity} \tag{2.30}$$

If we take the divergence of the Euler equation and combine with Poisson,

$$\frac{\partial}{\partial t}(\boldsymbol{\nabla}\cdot\boldsymbol{v}) + \frac{\dot{a}}{a}(\boldsymbol{\nabla}\cdot\boldsymbol{v}) = -\frac{1}{a}\nabla^2\phi = -4\pi G a\bar{\rho}\delta$$

and we know from continuity that

$$\boldsymbol{\nabla}\cdot\boldsymbol{v} = -a\frac{\partial\delta}{\partial t}$$

then

$$-a\frac{\partial^2\delta}{\partial t^2} - 2\dot{a}\frac{\partial\delta}{\partial t} = -4\pi G a\bar{\rho}\delta$$

or

$$\ddot{\delta} + 2\frac{\dot{a}}{a}\dot{\delta} = 4\pi G\bar{\rho}\delta \tag{2.31}$$

We are still in a matter only universe so $\rho \propto a^{-3}$ and to put all FRW dynamics in one parameter a we can substitute

$$4\pi G\bar{\rho} = \frac{3}{2}\Omega H^2 = \frac{3}{2}\frac{1}{a^3}\Omega_0 H_0^2$$

and get

$$\ddot{\delta} + 2\frac{\dot{a}}{a}\dot{\delta} = \frac{3}{2}\frac{1}{a^3}\Omega_0 H_0^2\delta \tag{2.32}$$

Given a function $a(t)$ to describe the dynamics of the Universe as a whole, we can solve the linearised equations of LSS. In general this gives two solutions known as the *growing mode* and *decaying mode*. The latter one is usually ignored as decay tends to be a self-destructive feature. Also both modes are separable in spatial and time evolution

$$\delta(\boldsymbol{x},t) = D_+(t)\Delta_+(\boldsymbol{x}) + D_-(t)\Delta_-(\boldsymbol{x})$$

Although adhesion theory along with Zel'dovich approximation is a slightly more non-linear approach (they are derived from the non-linear basis equations), we will see that the growing mode solution comes back in these formalisms and acts as *de facto time parameter*. That is, from now on we will forget about the dynamics of the Universe as a whole. The growing mode will act as be it time, but it can always be remapped to standard time units like expansion factor, redshift or Gyr, given the ingredients of any FRW universe. The Einstein-de Sitter universe is one of the simplest possible as it has $\Omega_m = \Omega_0 = 1$ and can be solved "on the back of an envelope". The growing mode solution in an EdS universe is proportional to the expansion factor and can be normalised to

$$D_+(t) = a(t). \tag{2.33}$$

In general, one can show that the growing mode solution is approximated by

$$D_+(t) = H(t) \int \frac{dt}{a^2(t)H^2(t)} \tag{2.34}$$

for any model having just matter and Λ contributions. In a universe dominated by dark energy with $-1 < w < -1/3$, there is no linear growth in structure. This also holds for the future of the concordance universe where D_+ peters out to ~ 1.35. (see fig. 2.3)

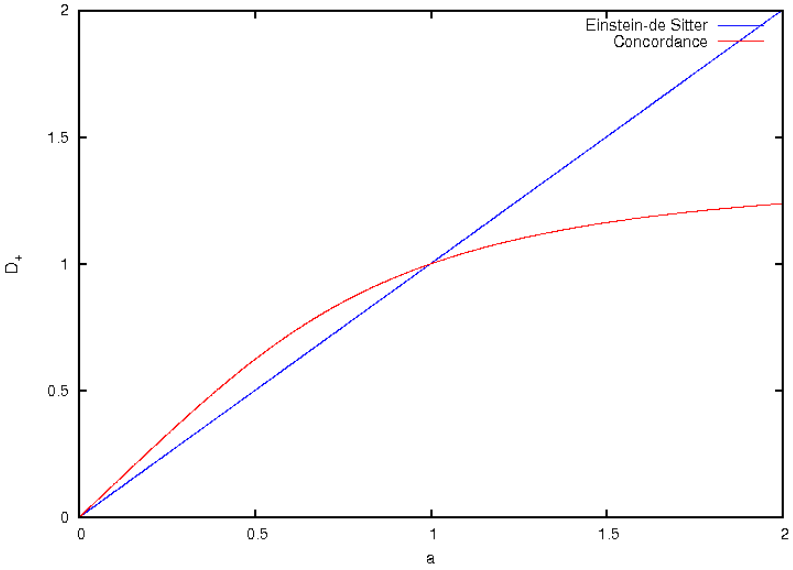

Figure 2.3: Growing mode solution in Einstein-de Sitter and Concordance model. Notice that in the Concordance model linear structure formation eventually stops, leveling off at $D_+ \sim 1.35$.

2.7 Non-linear structure formation

After perturbations grow to $\delta > 1$ we enter the non-linear regime. This regime is characterised by the following complications.

- anisotropic collapse
- hierarchical multiscale behaviour
- asymmetry between voids and clusters

We want to obtain a good description qualitative as well as quantitative of the large scale structure formation, despite the non-linearities.

Chapter 3

Zel'dovich approximation

The Zel'dovich approximation (hf. ZA) is the first step from the basic equations of structure formation to the adhesion approximation. We will derive it from the Lagrangian perturbation and show its mirth in simplifying the first stages of non-linear collapse. We will then see that ZA breaks down at some stage. It is in trying to see when and where ZA breaks down, that we will find the origin of adhesion.

In 1970 Zel'dovich (Zel'Dovich, 1970) published this very simple approximation to structure formation. The linearised equations describe the change of density in each individual volume element. A different approach is to take mass elements, and see how they occupy space. This way a single volume element might contain multiple particles streaming in different directions. This is the Lagrangian approach. In this particular Lagrangian approximation particles are given an initial velocity (or displacement), and this velocity does not change.

$$\boldsymbol{x} = \boldsymbol{q} + D_+ \boldsymbol{v}_0(\boldsymbol{q}) \tag{3.1}$$

The greatest virtue but also the main problem with the Zel'dovich approximation is that it is a local theory. Whenever global effects start to play a role it breaks down. Particles start to cross paths and at very late times all that remains is a thermal gas.

More than just a first approximation of how particles would move in a quasi linear regime, Zel'dovich comes with an important formalism that describes anisotropic collapse to first order. To understand where the Zel'dovich approximation comes from we need to elaborate on the Lagrangian formalism.

3.1 Eulerian vs. Lagrangian

There are two important perspectives when studying fluid dynamics of any sort. There is the "normal" view of coordinates fixed to some kind of reference: *Eulerian*. When describing ocean currents, we could use fixed coordinates of latitude and longitude to describe the gyros of the northern pacific. Next there is the view of moving along with the fluid elements, which is referred to as *Lagrangian*. Again using the ocean metaphor, we could dump a freight container of rubber ducks in the sea (this happens so now and then (Ebbesmayer et al., 2007)) and follow the conditions of each duck, and also find the proximity of the surrounding ducks as a measure for duck-density. The transition to-and-fro Lagrangian view is pivotal to this project.

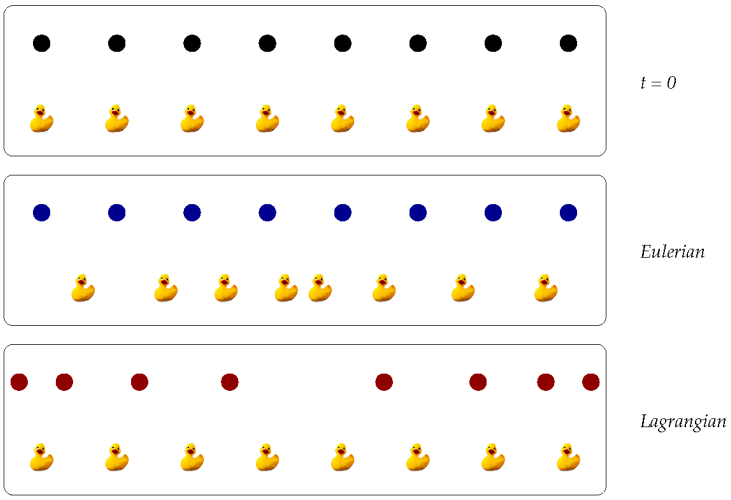

Figure 3.1: Eulerian and Lagrangian representations of a one-dimensional duck-universe.

When dealing with equations, this transition is embodied in the *full convective time derivative*

$$\frac{d}{dt} = \frac{\partial}{\partial t} + \boldsymbol{u} \cdot \boldsymbol{\nabla}_{\boldsymbol{r}}. \tag{3.2}$$

In comoving coordinates we get an extra $1/a$,

$$\frac{d}{dt} = \frac{\partial}{\partial t} + \frac{1}{a}\boldsymbol{v} \cdot \boldsymbol{\nabla}_{\boldsymbol{x}}. \tag{3.3}$$

To transform from Lagrangian view to Eulerian coordinates we have to integrate velocities over time

$$\boldsymbol{x}(\boldsymbol{q}, t) = \boldsymbol{q} + \int_0^t \boldsymbol{v}(\boldsymbol{q}, t')dt'$$

Lagrangian and Eulerian representations also embody two different numerical approaches. Lagrangian coordinates allow for a discretisation of mass, Eulerian coordinates for that of volume.

3.2 Expansion, vorticity and shear

If we decide to see the structure formation in terms of mass elements, it is not enough to think of rigid particles. During the evolution, elements are deformed. We can expand the equations of motion into three modes of deformation: expansion θ, vorticity ω_{ij} and shear σ_{ij}.

$$\frac{1}{a}\frac{\partial v_i}{\partial x_j} = \frac{1}{3}\theta\delta_{ij} + \sigma_{ij} + \omega_{ij}. \tag{3.4}$$

The tensor $\partial_j v_i/a$ has trace θ, a traceless symmetric part σ_{ij} and ω_{ij} is its anti-symmetric part,

$$\theta \equiv \frac{1}{a}\partial_i v^i \tag{3.5}$$

$$\sigma_{ij} \equiv \frac{1}{2a}\left(\partial_j v_i + \partial_i v_j\right) - \frac{1}{3}\partial_k v^k \delta_{ij} \tag{3.6}$$

$$\omega_{ij} \equiv \frac{1}{2a}\left(\partial_j v_i - \partial_i v_j\right) \tag{3.7}$$

Any two of these tensors multiplied will give 0, so any cross-terms in calculations using these quantities will drop out.

3.3 Lagrangian perturbation

Suppose we take a particle that adheres to the aforementioned non-linear equations of structure formation. We follow this particle from the start of our simulation at t_0 to some later time t. At t_0 this particle is situated at comoving coordinates $\boldsymbol{q}$. Since these coordinates leave no ambiguity as to which particle we are talking about we can use the vector $\boldsymbol{q}$ as a label for this particle and it's immediate differential surroundings, even at later times. We can make a map $\boldsymbol{x}(\boldsymbol{q}, t)$ to find the current Eulerian coordinates of the particle

$$\mathcal{L}(t) : \boldsymbol{q} \rightarrow \boldsymbol{x}(\boldsymbol{q}, t) \tag{3.8}$$

which we will refer to as the Lagrangian map. We now wish to make a perturbational expansion of this map. First we define the displacement $\boldsymbol{s} \equiv \boldsymbol{x} - \boldsymbol{q}$

$$\boldsymbol{x}(\boldsymbol{q}, t) = \boldsymbol{q} + \boldsymbol{s}'(\boldsymbol{q}, t) + \boldsymbol{s}''(\boldsymbol{q}, t) + \ldots \tag{3.9}$$

where

$$1 \gg \left|\frac{\partial \boldsymbol{s}'}{\partial \boldsymbol{q}}\right| \gg \left|\frac{\partial \boldsymbol{s}''}{\partial \boldsymbol{q}}\right| \gg \dots$$

Out of mass conservation

$$\rho(\boldsymbol{x}, t)d\boldsymbol{x} = \bar{\rho}(t)d\boldsymbol{q},$$

we find the density from the Jacobian of the Lagrangian map

$$1 + \delta(\boldsymbol{x}, t) = \frac{\rho}{\bar{\rho}} = \det\left(\frac{\partial \boldsymbol{x}}{\partial \boldsymbol{q}}\right)^{-1}$$

Using the perturbation from equation (3.9) we can find that

$$\frac{\partial \boldsymbol{x}}{\partial \boldsymbol{q}} = \mathbf{1} + \frac{\partial \boldsymbol{s}'}{\partial \boldsymbol{q}} + \dots$$

and

$$\det\left(\frac{\partial \boldsymbol{x}}{\partial \boldsymbol{q}}\right) \approx 1 + \boldsymbol{\nabla}_q \cdot \boldsymbol{s}' + \dots$$

then

$$\delta'(\boldsymbol{x}, t) = -\boldsymbol{\nabla}_q \cdot \boldsymbol{s}' \tag{3.10}$$

We may insert this expression into the Poisson equation with the potential perturbation ϕ'.

$$\nabla^2\phi' = 4\pi G\bar{\rho}a^2\delta' = -4\pi G\bar{\rho}a^2\boldsymbol{\nabla}_q \cdot \boldsymbol{s}'$$

If we then assume that the displacement is a potential field $\boldsymbol{s}' = \boldsymbol{\nabla}\chi$, that is $\boldsymbol{\nabla}_q \times \boldsymbol{s}' = 0$, we can invert the Poisson equation to

$$\boldsymbol{\nabla}\phi' = -4\pi G\bar{\rho}a^2\boldsymbol{s}'$$

If we then combine this with the linearised Euler equation, we get

$$\ddot{\boldsymbol{s}}' + 2\frac{\dot{a}}{a}\dot{\boldsymbol{s}}' = 4\pi G\bar{\rho}\boldsymbol{s}' \tag{3.11}$$

Which is identical to equation (2.31). We can use the same growing and decaying mode solutions we found earlier. Ignoring the decaying mode again

$$\boxed{\boldsymbol{x} = \boldsymbol{q} + D_+(t)\boldsymbol{u}_0(\boldsymbol{q})} \tag{3.12}$$

Note, from now on we will drop the time parameter from the notation of D, as the growing mode solution will act as the new de facto time parameter. Where $\boldsymbol{u}_0(\boldsymbol{q})$ is the *displacement field*, which we can relate to a *displacement potential* because of the earlier assumption of potential motion

$$\boldsymbol{u}_0(\boldsymbol{q}) = -\boldsymbol{\nabla}_q \Phi_0(\boldsymbol{q}) \tag{3.13}$$

Next we would like to relate the displacement potential to the gravitational potential and the peculiar velocity.

$$\boldsymbol{v} = a\dot{\boldsymbol{x}} = -a\dot{D}_+ \boldsymbol{\nabla}_q \Phi_0 = -aD_+ H f(\Omega) \boldsymbol{\nabla}_q \Phi_0$$

where $f(\Omega) \equiv a\dot{D}_+ / \dot{a}D_+ = d\log D_+ / d\log a$ is the dimensionless *linear velocity growth factor*, which is often approximated as a power law (Peebles, 1980)

$$f(\Omega_m) \approx \Omega_m^{0.6}$$

Using the result that in the linear regime $\boldsymbol{v} \propto \boldsymbol{g}$,

$$\boldsymbol{v} = \frac{2f(\Omega)}{3\Omega H} \frac{\boldsymbol{\nabla}_x \phi}{a}$$

we get

$$\Phi_0(\boldsymbol{q}) = \frac{2}{3D_+ a^2 H^2 \Omega} \phi(\boldsymbol{x}, t) \equiv A\phi(\boldsymbol{x}, t) \tag{3.14}$$

where $A^{-1} = 3/2D_+ a^2 H^2 \Omega$.
In Fourier space we find the following relations. Say

$$\delta_0(\boldsymbol{x}) = \int \frac{d\boldsymbol{k}}{(2\pi)^3} \hat{\delta}_0(\boldsymbol{k}) e^{-i\boldsymbol{k}\cdot\boldsymbol{x}},$$

then

$$\hat{\Psi}(\boldsymbol{k}) = \frac{1}{k^2} \hat{\delta}(\boldsymbol{k}),$$

$$i\hat{\boldsymbol{u}}_0(\boldsymbol{k}) \ = -i\frac{\boldsymbol{k}}{k^2} \hat{\delta}(\boldsymbol{k}),$$

and

$$\hat{d}_{ij}(\boldsymbol{k}) = -\frac{k_i k_j}{k^2} \hat{\delta}(\boldsymbol{k}).$$

3.4 Generalised Zel'dovich formalism

There is another more general approach to the Zel'dovich approximation. We introduce a new comoving velocity $\boldsymbol{u} \equiv (d\boldsymbol{x}/dD_+)$ and rewrite the equations of motion in terms of $\boldsymbol{u}$

$$\boldsymbol{v} = a\dot{\boldsymbol{x}} = a\dot{D}_+ \boldsymbol{u}$$

Then we can rewrite Euler's equation

$$\frac{\partial \boldsymbol{u}}{\partial D_+} + (\boldsymbol{u}\cdot\boldsymbol{\nabla}_x)\boldsymbol{u} = \frac{1}{(a\dot{D}_+)^2}(B\boldsymbol{u} - \boldsymbol{\nabla}_x \phi) \tag{3.15}$$

where $B = -(2a\dot{a}\dot{D}_+ + a^2\ddot{D}_+) = -\frac{\partial}{\partial t}\left(a^2\dot{D}_+\right)$.
If we then take equation (3.12), which implies $\dot{\boldsymbol{x}} = \dot{D}_+\boldsymbol{u}$ and using

$$-\boldsymbol{\nabla}_x\phi = \partial(a\boldsymbol{v})/\partial t = 2a\dot{a}\dot{\boldsymbol{x}} + a^2\ddot{\boldsymbol{x}}$$

then

$$\boldsymbol{\nabla}_x\phi = B\boldsymbol{\nabla}_x\Phi = B\boldsymbol{u}$$

and the right-hand term in equation (3.15) drops out, leaving

$$\boxed{\frac{\partial \boldsymbol{u}}{\partial D_+} + (\boldsymbol{u}\cdot\boldsymbol{\nabla}_x)\boldsymbol{u} = 0} \tag{3.16}$$

Also from equation (3.14) this leads us to quantify $B = A^{-1}$. This can be understood as the gravitational acceleration being cancelled by the Hubble flow.
If we take a step back, we can rewrite equation (3.15) (which is still the full Euler equation) to the case of potential motion using $\boldsymbol{u} = -\boldsymbol{\nabla}_x\Phi$ and integrating

$$\frac{\partial\Phi}{\partial D_+} + \frac{1}{2}(\boldsymbol{\nabla}_x\Phi)^2 = -\frac{1}{a\dot{D}_+^2}(\Phi + A\phi) \tag{3.17}$$

This is often referred to as the Bernoulli equation (Kofman and Pogosyan, 1995). We can appreciate the right hand side vanishing for the Zel'dovich approximation, but we could imagine other approaches from this point. The reason why non-linear LSS is so complicated is because it is non-local. It is precisely the non-local term in the Bernoulli equation that is set to nil in the case of the Zel'dovich approximation. Other members of the family include higher order Lagrangian perturbation, truncated Zel'dovich, frozen flow, and last but not least adhesion approximation. Every member has a distinct way of dealing with the non-local right hand term (see Sahni and Coles, 1995, for a review). Different approaches have been tested against N-body simulations in comparative studies. (Coles et al., 1993; Melott et al., 1994)

3.5 Anisotropic collapse

Along with the equation comes a beautiful interpretation of early structure formation, namely that of collapsing ellipsoids. To see what a local perturbation will do; collapse as a wall, filament, cluster or expand to become void, we can study the eigenvalues of the deformation tensor.
If we look at the density evolution in the Zel'dovich approximation, as before

$$\frac{\rho}{\bar{\rho}} = \det\left(\frac{\partial \boldsymbol{x}}{\partial \boldsymbol{q}}\right)^{-1}$$

and using expression (3.12)

$$\frac{\rho}{\bar{\rho}} = \det\left(\delta_{ij} - D_+ d_{ij}\right)^{-1}$$

where we defined the *deformation tensor*

$$d_{ij} \equiv \frac{\partial^2 \Phi_0}{\partial q_i \partial q_j}$$

We know this determinant to be equal to that of the diagonalised Jacobian matrix.

$$\boxed{\rho(\boldsymbol{q}, t) = \frac{\bar{\rho}}{(1 - D_+\lambda_1(\boldsymbol{q}))(1 - D_+\lambda_2(\boldsymbol{q}))(1 - D_+\lambda_3(\boldsymbol{q}))}} \tag{3.18}$$

where $\lambda_1 > \lambda_2 > \lambda_3$ are the eigenvalues of the deformation tensor.

Figure 3.2: Ellipsoidals: each signature of eigenvalues corresponds to a mode of ellipsoidal collapse.

As can be seen in figure (3.2), the signatures of the eigenvalues indicate the shape of an ellipsoidal overdensity. The corresponding eigenvectors give the direction of the principal axes of the ellipsoid.
Equation (3.18) contains singularities where eigenvalues are positive. Locally the density becomes infinite when $D_+ = 1/\lambda_1$. At this moment the structure is collapsed in one direction but still free-streaming in two other directions. In the Zel'dovich formalism this signals the formation of a *pancake*. If $\lambda_1 \approx \lambda_2$, the ellipsoid will collapse in two directions at the same time, and a filament forms. At a density peak all eigenvalues will be positive: a cluster appears. If all of the eigenvalues are negative, the particle will never collapse and can be said to live in a void. The distribution of eigenvalues in Gaussian random fields was calculated by Doroshkevich (1970), giving the probability of 8% that all eigenvalues are negative (van de Weygaert and Bond, 2005a) (by symmetry, this also gives a probability of 8% that all eigenvalues are positive, and 42% both for the two remaining signatures).

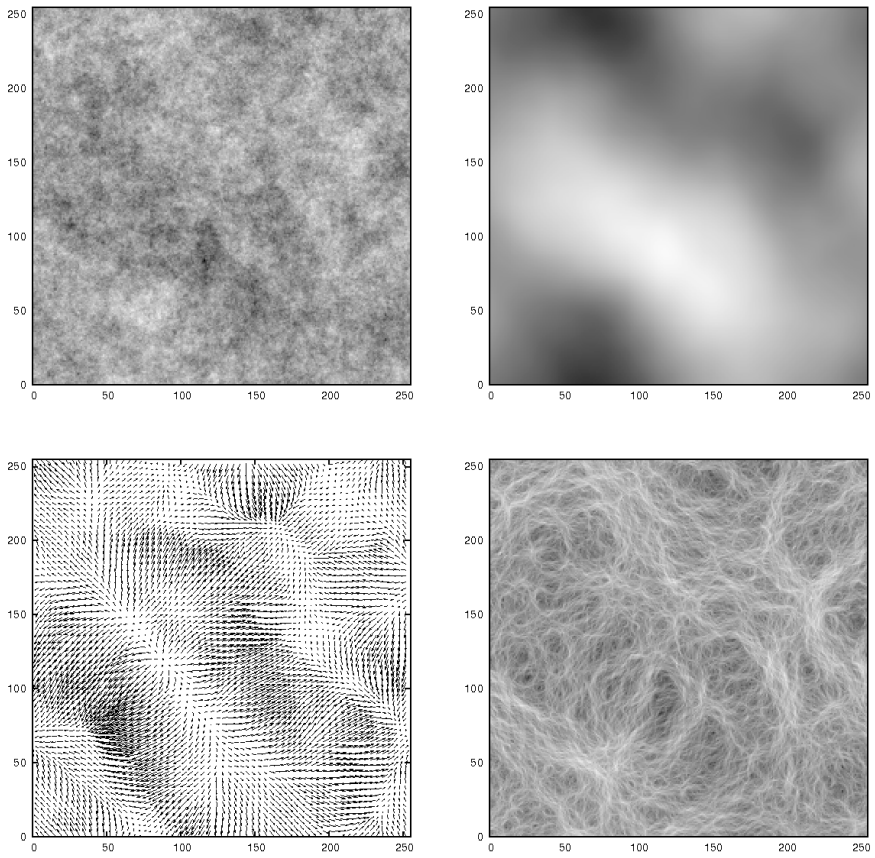

Figure 3.3: Integrals of the density: from left to right, top to bottom: a primordial Gaussian density field with $P(k) = k^{-1}$, the potential, displacement field and the maximum eigenvalue of the deformation tensor.

3.6 Caustics

From equation (3.18) we can see that the density in a gravitationally collapsing pressureless medium develops singularities. A singularity will then develop into a region where particles are streaming in multiple directions. The caustics that form this way can be described by *catastrophe theory*.

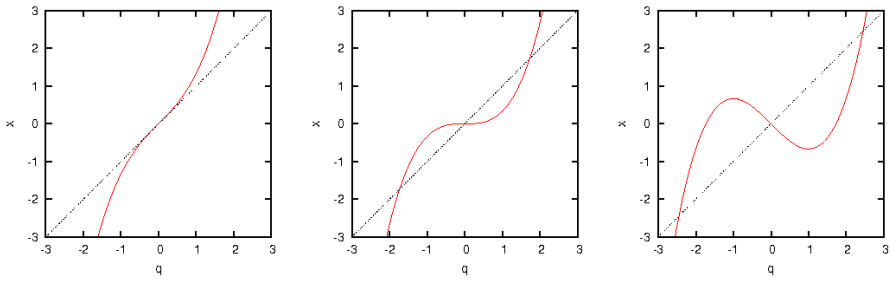

Figure 3.4: Multistream region: the function $x = \frac{1}{3}q^3 + \alpha q$ with $\alpha = +1, 0, -1$ shows how a multistream region develops. From the second panel onward the density reaches infinity locally: a caustic is formed.

The theory was developed by René Thom, and further extended by Vladimir Arnold. Catastrophes can be classified using Arnold's ADE classification on the potential generating the caustic. One of the most common singularity of this type is the cusp singularity, illustrated in figure (3.5). Zel'dovich attracted the attention of Arnold to the problem of singularities in the large scale structure. They produced an overview of all possible singularities in 2-D structure formation (Arnold et al., 1982).
Since the application of caustics in large scale structure formation has a somewhat turbulent past, a historic note is appropriate. The concept was used by the proponents of the Hot Dark Matter top-down scenario of structure formation. This theory was discarded for the Cold Dark Matter hierarchical scenario, in which large scale structure is build from the bottom up, by series of mergers. However, the use of CDM does not mean there will be no caustics. Caustics will emanate from any pressureless medium with a sufficiently heterogenic velocity field. The question remains what role the dark matter caustics play in the Universe in the context of hierarchical structure formation. For example, there are dark matter models that predict the annihilation of dark matter in caustics (Hogan, 2001), this might in turn cause the Universe to reionise (Belikov and Hooper, 2009). Attempts to detect caustics using weak lensing (Gavazzi et al., 2006) have thus far not been successful. Also caustics are usually not resolved in cosmic N-body simulations.

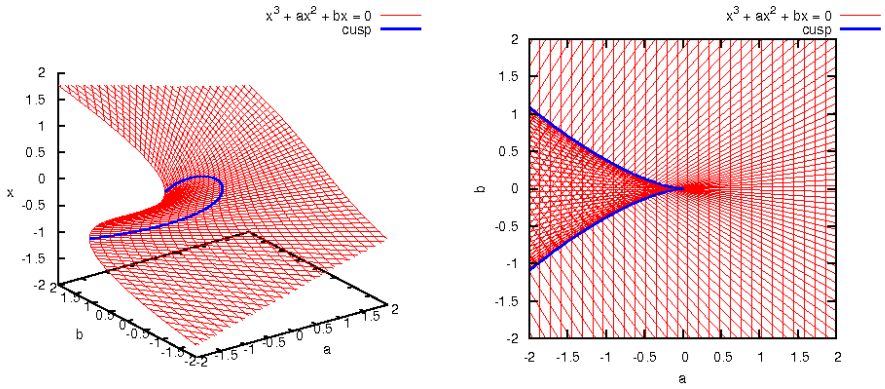

Figure 3.5: Cusp singularity: The canonical example of a cusp singularity, in isometric and top-down projection. The green line marks the singularity that separates the free-flow from the multi-stream area. At the cusp, the density is infinite.

Figure 3.6: Caustics in a swimming pool: Caustics can be found in daily life. Notice the similarity with figure (**??**b). (courtesy of Rob Patrick: `http://www.flickr.com/photos/alkalinezoo/`)

Chapter 4

Burgers' dynamics

We saw how ZA has the potential of predicting how the first structures are formed. Voids start growing at locations with a divergent velocity field. In between these voids we find pancakes and where pancakes intersect filaments that connect a field of galaxy clusters. ZA does *not* tell us what happens *after* the formation of the first shocks. If we take the ZA equation of motion

$$\frac{\partial \boldsymbol{u}}{\partial D_+} + (\boldsymbol{u} \cdot \boldsymbol{\nabla}_x)\boldsymbol{u} = 0 \tag{4.1}$$

and add a viscosity term

$$\frac{\partial \boldsymbol{u}}{\partial D_+} + (\boldsymbol{u} \cdot \boldsymbol{\nabla}_x)\boldsymbol{u} = \nu \nabla_x^2 \boldsymbol{u} \qquad \text{(Burger's equation)} \tag{4.2}$$

we arrive at Burgers' equation. The viscosity term would prevent particle orbit crossing, thus preserving shocks after they form. This allows us to track the emergence of the cosmic web to much later times than ZA is capable of.

The use of Burgers' equation as a model for large scale structure was introduced by Gurbatov and Saichev (1984) and was advocated mainly by Soviet astrophysicists in the late 80's and early 90's (Shandarin, 1988; Gurbatov et al., 1989; Shandarin and Zeldovich, 1989; Kofman et al., 1990; Shandarin, 1991; Kofman et al., 1992).

Adhesion theory is also referred to as the "sticky particle" model, but since it is not dealing with particles as such this is something of a misnomer. What we mean by the word "particle" is a test particle or bead moving with the fluid. Moreover we will see, once particles are inside shocks, they lose their "sticking" ability. That is why we prefer the name "Burgers' dynamics".

4.1 Burgers' equation

Burgers' equation was put forward by the Dutch mathematician Johannes Martinus Burgers around 1940 as a possible model for describing certain cases of turbulence.

$$\frac{\partial \boldsymbol{u}}{\partial D_+} + (\boldsymbol{u} \cdot \boldsymbol{\nabla}_x)\boldsymbol{u} = \nu \nabla_x^2 \boldsymbol{u} \qquad \text{(Burger's equation)} \tag{4.3}$$

We study the case of potential flow, where $\boldsymbol{u} = -\nabla\Phi$. Using the Hopf-Cole transformation (Hopf, 1950)

$$U = e^{\Phi/2\nu},$$

this transforms Burgers' equation into the diffusion equation

$$\frac{\partial U}{\partial D_+} = \nu \nabla^2 U \tag{4.4}$$

Which leads to the following solution.

$$\boldsymbol{u}(\boldsymbol{x}, D_+) = -2\nu \nabla \ln U(\boldsymbol{x}, D_+) \tag{4.5}$$

$$U(\boldsymbol{x}, D_+) = \int \exp\left[\frac{\Phi_0(\boldsymbol{q})}{2\nu}\right] \exp\left[\frac{-(\boldsymbol{x}-\boldsymbol{q})^2}{4D_+\nu}\right] d^3\boldsymbol{q} \tag{4.6}$$

this last term can also be written as a convolution with a Gaussian kernel

$$U(\boldsymbol{x}, D_+) = \left(U_0 * K_{D_+\nu}\right)$$

$$K(\boldsymbol{q}; D_+, \nu) = \exp\left[-\frac{q^2}{4D_+\nu}\right]$$

Transformed back, the entire expression expands to

$$\boldsymbol{u}(\boldsymbol{x}, D_+) = \frac{\int_{-\infty}^{\infty} \frac{\boldsymbol{x}-\boldsymbol{q}}{D_+} \exp\left[G/(2\nu)\right] d^3\boldsymbol{q}}{\int_{-\infty}^{\infty} \exp\left[G/(2\nu)\right] d^3\boldsymbol{q}} \tag{4.7}$$

where

$$G(\boldsymbol{x}, \boldsymbol{q}, D_+) \equiv \Phi_0(\boldsymbol{q}) - \frac{(\boldsymbol{x}-\boldsymbol{q})^2}{2D_+}$$

4.2 Inviscid limit

In the inviscid limit we take the limit of $\nu \to 0$ [1]. So all contribution of the integral comes from the point where $G(x, q, t)$ has a global maximum. Using steepest descent method to calculate the limit $\nu \to 0$ one gets

[1] this is different from $\nu = 0$, because that would bring us back to the pure Zel'dovich approximation.

$$\Phi(\boldsymbol{x}, D_+) = \max_q \left[\Phi_0 - \frac{(\boldsymbol{x} - \boldsymbol{q})^2}{2D_+} \right] \tag{4.8}$$

This is often illustrated by means of a parabola scanning the velocity potential as in figure (4.1). We could imagine scanning the initial velocity potential with a parabolic needle. The apex of this needle gives the coordinate $\boldsymbol{x}$, while it is touching the potential at point $\boldsymbol{q}$. Whenever the parabola has two touching points (given the 1-D example), two particles occupy the same location. This means that at that location there is a shock containing all particles in between the two touching points. The thickness of the needle depends on time, making particles and shocks move.

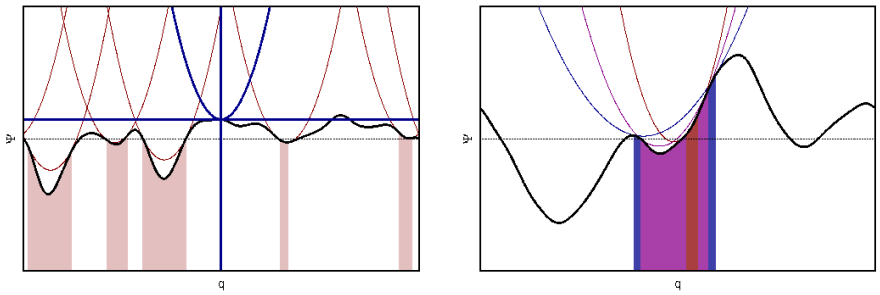

Figure 4.1: Parabolic interpretation: The interpretation of the Hopf-Cole solution by means of a scanning parabola. The width of the parabola is proportional to D_+. The shaded area gives the particles in Lagrangian space that have collapsed to form structure. We can see this area evolve when we increase D_+ in the second figure.

We model the movement of a particle by putting it at the apex of a parabola that touches the velocity potential; to fix the derivative

$$\boldsymbol{x} = \boldsymbol{q} - D_+ \boldsymbol{\nabla}_q \Phi_0$$

then integrate and call the constant of integration h

$$\Phi_0(\boldsymbol{q}) = \frac{(\boldsymbol{x} - \boldsymbol{q})^2}{2D_+} + h(\boldsymbol{x}, D_+)$$

When parabola from different particles $\boldsymbol{q}$ coincide, the particles 'stick' and have to move on together. So in stead of just calculating $\boldsymbol{x}$ from the above relation we have to find a global fit

$$\Phi(\boldsymbol{x}, D_+) = \max_q \left[\Phi_0(\boldsymbol{q}) + \frac{(\boldsymbol{x} - \boldsymbol{q})^2}{2D_+} \right]$$

which shows that equation (4.8) behaves as intended. This reduces the problem to finding points on the surface of the potential where the parabola has multiple touching points.

4.3 Dynamics of shocks

In the one dimensional case, the parabola will have two touching points where there is a shock. If we call these points a and b, the mass of the shock will be the *Lagrangian interval* $m_s = \bar{\rho}(|\boldsymbol{q}_b - \boldsymbol{q}_b|)$ and have position $\boldsymbol{x}_s$. We are recording the exact moment the particles a and b collide (see figure 4.3). The parabola

$$P = \frac{(\boldsymbol{x} - \boldsymbol{q})^2}{2D_+} + h$$

then has two touching points with Φ_0 at a and b. This gives two equations with two unknowns

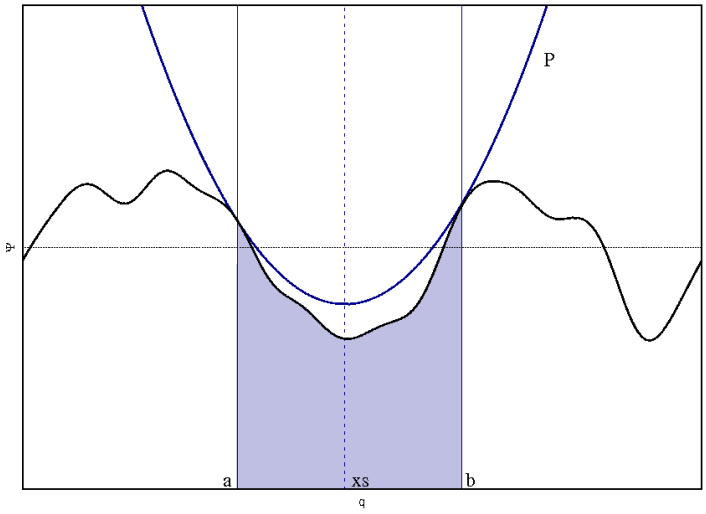

$$\frac{(\boldsymbol{x}_s - \boldsymbol{q}_a)^2}{2D_+} + h = \Phi_a$$
$$\frac{(\boldsymbol{x}_s - \boldsymbol{q}_b)^2}{2D_+} + h = \Phi_b$$

then we subtract them

$$\frac{-\boldsymbol{x}_s(\boldsymbol{q}_b - \boldsymbol{q}_a)}{D_+} = \Phi_b - \Phi_a$$

and

$$\boxed{\boldsymbol{u}_s = \frac{\partial \boldsymbol{x}_s}{\partial D_+} = -\frac{\Phi_b - \Phi_a}{\boldsymbol{q}_b - \boldsymbol{q}_a}} \tag{4.9}$$

that is, momentum is conserved in shocks. However easy this may seem in the case of a point singularity, the dynamics within filaments and sheets is non-trivial. (Bogaevsky, 2004; Bec and Khanin, 2007) As degrees of freedom remain, densities within shocks continue to evolve.

4.4 Convex hull interpretation

However, it was shown by Vergassola et al. (1994) that when we rewrite the formulas, there is a more powerful interpretation in the form of the Legendre transform. We can write down an expression for the velocity potential

$$\Phi(\boldsymbol{x}, D_+) = \max_q \left[\Phi_0(\boldsymbol{q}) - \frac{(\boldsymbol{x}-\boldsymbol{q})^2}{2D_+}\right] \tag{4.10}$$

$$= \max_q \left[\Phi_0(\boldsymbol{q}) - \frac{x^2 - 2\boldsymbol{x}\cdot\boldsymbol{q} + q^2}{2D_+}\right] \tag{4.11}$$

Since $\boldsymbol{x}$ and D_+ are constants in the expression we can manipulate them within the maximum without consequence.

$$D_+\Phi(\boldsymbol{x}, D_+) = \max_q \left[D_+\Phi_0(\boldsymbol{q}) - \frac{q^2}{2} + \boldsymbol{x}\cdot\boldsymbol{q}\right] - \frac{x^2}{2} \tag{4.12}$$

$$\equiv H(\boldsymbol{x}, D_+) - \frac{x^2}{2} \tag{4.13}$$

We define the Lagrangian potential

$$\varphi(\boldsymbol{q}, D_+) \equiv D_+\Phi_0(\boldsymbol{q}) - \frac{q^2}{2} \tag{4.14}$$

and its counterpart

$$H(\boldsymbol{x}, D_+) \equiv D_+\Phi + \frac{x^2}{2}. \tag{4.15}$$

Then

$$H(\boldsymbol{x}, D_+) = \max_q \left[\varphi(\boldsymbol{q}, D_+) + \boldsymbol{x}\cdot\boldsymbol{q}\right], \tag{4.16}$$

that is, H is the Legrendre transform of φ. The coordinate $\boldsymbol{q}$ at which the maximum is found gives us the Eulerian map $\mathcal{E} : \boldsymbol{x} \mapsto \boldsymbol{q}$

$$\boldsymbol{q}(\boldsymbol{x}, D_+) = \arg\max_q \left[\varphi(\boldsymbol{q}, D_+) + \boldsymbol{x}\cdot\boldsymbol{q}\right]$$

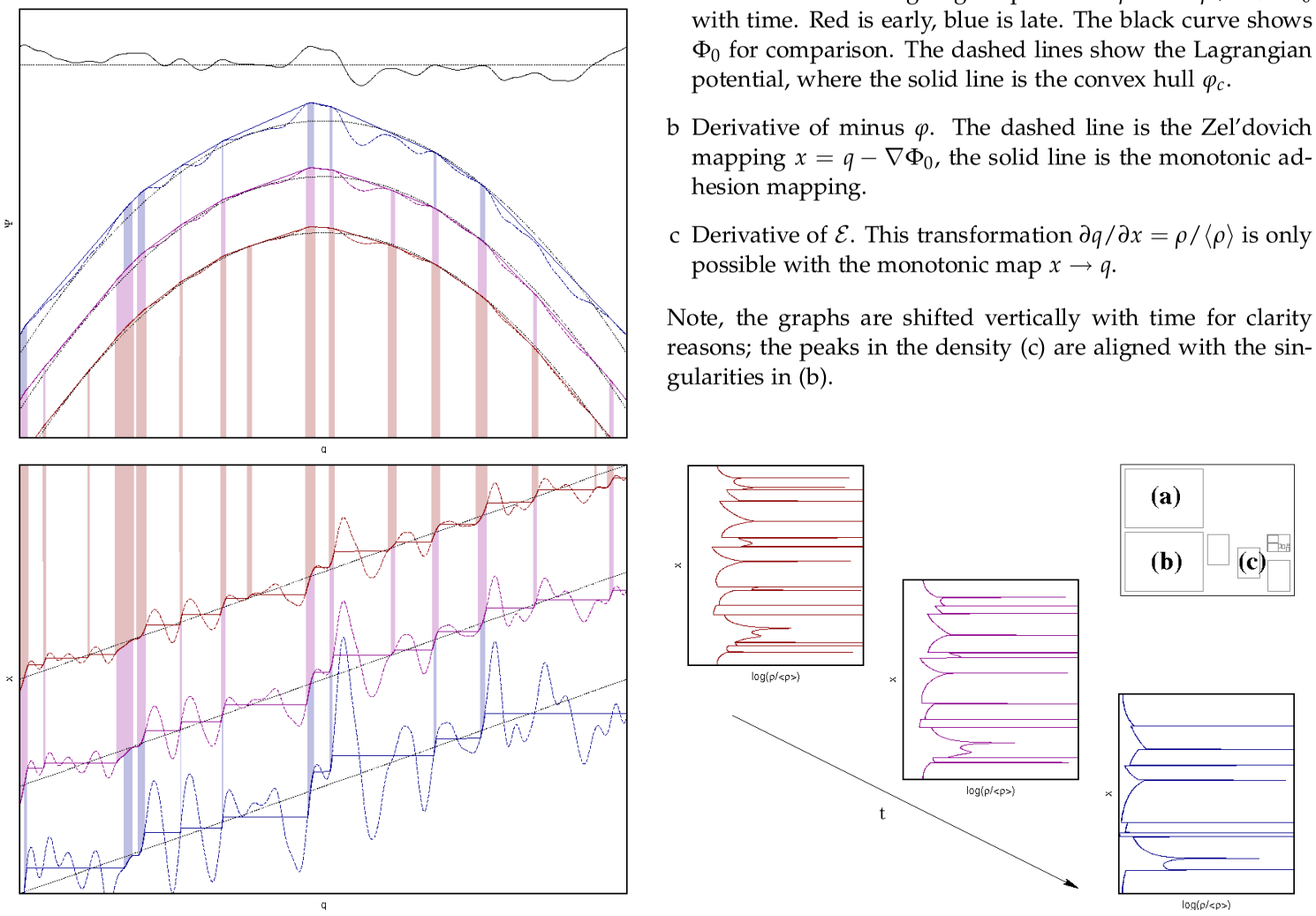

a Evolution of the Lagrangian potential $\varphi = -q^2/2 + t\Phi_0$ with time. Red is early, blue is late. The black curve shows Φ_0 for comparison. The dashed lines show the Lagrangian potential, where the solid line is the convex hull φ_c.

b Derivative of minus φ. The dashed line is the Zel'dovich mapping $x = q - \nabla\Phi_0$, the solid line is the monotonic adhesion mapping.

c Derivative of $\mathcal{E}$. This transformation $\partial q/\partial x = \rho/\langle\rho\rangle$ is only possible with the monotonic map $x \to q$.

Note, the graphs are shifted vertically with time for clarity reasons; the peaks in the density (c) are aligned with the singularities in (b).

Figure 4.2: Convex hull interpretation.

The Legendre transform has the property that only the convex part of the Lagrangian potential has a contribution. If we perform an inverse Legendre transform on H we can retrieve the convex hull of the Lagrangian potential.

$$\varphi_c(\boldsymbol{q}, D_+) = \min_x \left[H(\boldsymbol{x}, D_+) - \boldsymbol{x} \cdot \boldsymbol{q} \right]$$

To represent the solution in the form of a convex hull problem stresses a few properties that were neglected up to this point. The problem is one of global minimisation. We are helped by the fact that we are looking for a monotonic map

$$\text{if} \quad q_a \leq q \leq q_b \quad \text{then} \quad x_a \leq x \leq x_b.$$

This monotonicity is a necessity to calculate the inverse map, and also it is a property of the convex hull.
The entire construction is illustrated in figure 4.2. This figure should be followed starting at the top-left at the potential, going down to the coordinate mapping and then right to the densities. Panel (a) shows the velocity potential Φ_0 in black, and the Lagrangian potential φ and its convex hull φ_c for three different time-steps, increasing from red to blue. The anchor points of the convex hull with the Lagrangian potential are the regions that are still non-singular. These are shaded accordingly and can be followed down towards the mapping in panel (b). Here we can see the Zel'dovich mapping over-plotted with the adhesion mapping. In the non-singular (shaded) regions these two mappings coincide. These regions can be seen to shrink, and disappear, with time increasing. From the mapping we move to the densities, where we can see the peaks coincide with the singular regions in the mapping. As non-singular (shaded) regions disappear in panels (a) and (b), peaks in the density merge in a tree of hierarchical collapse. We will now highlight some aspects of each of the three panels in this figure.

4.4.1 Legendre-Fenchel conjugate and convex hulls

The Legendre-Fenchel conjugate

$$f^*(y) = \max_x \left[f(x) - xy \right],$$

also known as the Legendre transform, was first used by Legendre to express a function in terms of its own derivative

$$f^*(f'(x)) = f(x).$$

This is only possible if the map $M : x \mapsto f'(x)$ is one-to-one. Suppose $f'(x)$ is continuous, then $f(x)$ needs to be a *convex* function and $f'(x)$ is monotonic. We can still find the Legendre transform for non-convex functions. Let $f_c(x)$ be the convex hull of $f(x)$, then $f^*(y) = f_c^*(y)$. The convex hull is defined as the shortest enclosing path around a set of points.

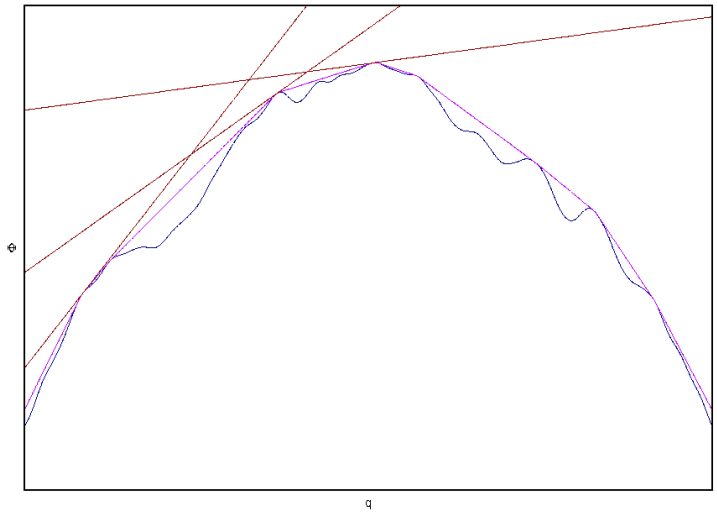

Figure 4.3: Construction of convex hull: for each line, we find the unique touching point, such that the line does not intersect the potential somewhere else.

For each slope y, we take the line $k : x \to xy$ and let it drop onto $f(x)$, then $f^*(y)$ attains the value where the line first touches $f(x)$ (see figure 4.3).

4.4.2 Maxwell's rule

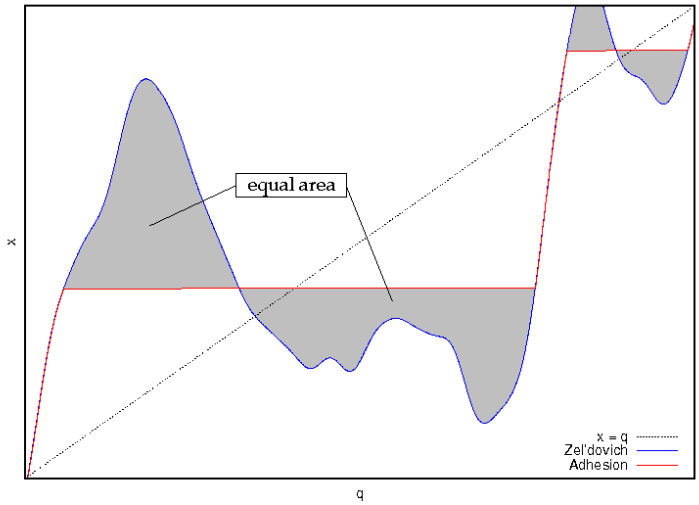

Figure 4.4: Maxwell's rule: the total area of the Zel'dovich mapping minus the adhesion mapping should vanish. This can also be seen in figure (4.2b).

The conservation of momentum can also be seen in figure (4.2b). We look at this part in more detail in figure (4.4). The location of the shock follows Maxwell's rule, which states that the integrated area of the Zel'dovich mapping over the shock interval should be equal to that of the adhesion mapping.

4.4.3 Hierarchical collapse

Figure 4.2 shows a formal method of taking an initial density perturbation, and turning it into a system of hierarchical collapse. We need little imagination to see that this tool can indeed be very powerful to understand the formation of structure in the Universe. From the Eulerian map, we retrieve the density

$$\frac{\rho}{\bar{\rho}} = \det\left[\frac{\partial \boldsymbol{q}}{\partial \boldsymbol{x}}\right].$$

This can be seen in figure 4.2, comparing panel *b* with panel *c*. The simplest case is that of one-dimensional self-similar collapse as illustrated in figure 4.5.

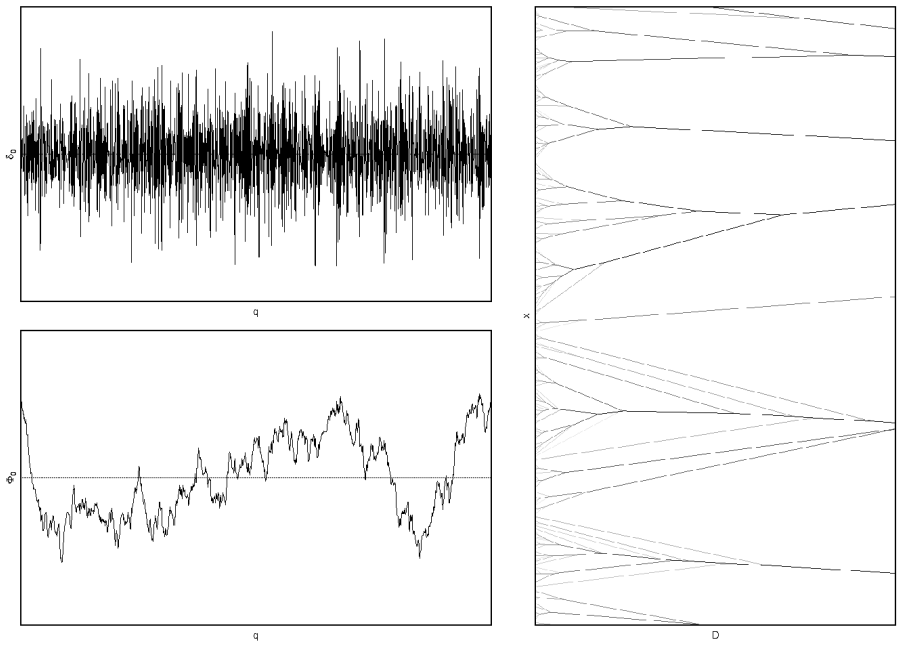

Figure 4.5: Merger cascade: A cascade of a 1D self-similar model with $n = 1$ (brown noise). This shows hierarchical collapse in it's purest form.

In the top panel of figure (4.5) is the initial density, which is very noisy. Below the density is the potential, which is still sharply peaked. The sharp peaks result in a density evolution that is singular from the first moment. This results in a cascade of clusters, which is shown in the right panel. The direction of

the clusters change when there is a merger, according to the conservation of momentum. Since the collisions are completely inelastic, energy is not conserved.

Chapter 5

Numerical Algorithms

While Burgers' equation has an analytical solution, it only gives velocities in integral form, so we still need some numerical techniques to calculate this solution. In the case of the inviscid limit, we need to find a global minimum for each particle. Or if $\nu > 0$, we need to integrate over time. We followed two algorithms, to compute the corresponding structure and implemented these into C++ codes.

5.1 Periodic boundary conditions

All of our simulations are done using *periodic boundary conditions*. Players of games, may recognise the Universe Pacman lives in. The topology of this universe can be described as the surface of a torus. This method only resembles the real Universe if the *minimum image criterion* is observed, this means there are no interactions that reach over half of the simulation box. For ΛCDM scenarios this forces us to choose box a size large enough to contain the largest non-linear Fourier modes. In the case of the scale free scenarios, we need to take care when $n + d \rightarrow 0$. Periodic boundary conditions make it easy to create initial conditions in Fourier space. We don't need to bother about boundary effects in the numerous tools we use to analyse our simulations. [1]

5.2 Convolution method

This method is described by Weinberg and Gunn (1990). It solves the viscid Burgers' equation and is relatively easy to implement. They observed that the

[1] It does add a few complications in the implementation some of the algorithms. Most of these complications are solved using binary number tricks, assuming the box size to be 2^n.

solution

$$\boldsymbol{u}(\boldsymbol{x}, D_+) = \frac{\int_{-\infty}^{\infty} \frac{\boldsymbol{x}-\boldsymbol{q}}{D_+} \exp\left[G/(2\nu)\right] d^3\boldsymbol{q}}{\int_{-\infty}^{\infty} \exp\left[G/(2\nu)\right] d^3\boldsymbol{q}} \tag{5.1}$$

is nothing more than a Gaussian convolution of the transformed potential.

$$U = e^{\Phi/2\nu}$$

$$U(\boldsymbol{x}, D_+) = \left(U_0 * K_{D_+\nu}\right) = \int U_0(\boldsymbol{x}-\boldsymbol{q}) K(q) d\boldsymbol{q}$$

$$K(\boldsymbol{q}; D_+, \nu) = \exp\left[-\frac{q^2}{4D_+\nu}\right]$$

First we transform the initial potential Φ_0 to U_0. Then for every time step we create a Gaussian kernel and perform a convolution. A convolution is usually done in Fourier space using the convolution theorem

$$(f * g) = \mathcal{F}^{-1}(\hat{f}\hat{g})$$

However Weinberg & Gunn argue that numerical precision is lost in the process of transforming to-and-fro Fourier space. We want to utilize every bit of numerical significance we can get, to keep ν as low as possible. So instead we perform the convolution in real space. This is possible because the kernel is symmetric. The convolution is simply performed, first in the x-direction then y and last z. This makes the operation nearly as fast as the Fourier based alternative. We are then left with a straight forward time integration of

$$\boldsymbol{u} = \frac{1}{2\nu} \boldsymbol{\nabla}_x \log U$$

There are numerous algorithms to do this, but a simple leap-frog scheme suffices for our purposes (Weinberg and Gunn, 1990). We emphasise that this algorithm is very fast and easy to implement.

5.3 Discrete scale-space

There are two places where careful application of scale-space analysis is in order. The first is when solving the heat equation

$$\frac{\partial u}{\partial t} = \alpha \nabla^2 u \tag{5.2}$$

in the Weinberg & Gunn model. The following argument is extracted from an article Lindeberg (1990) [2]

[2] which has restricted access, however there are several non-reviewed articles on the subject available on Lindeberg's website.

If we are to solve such an equation numerically, there is an intuitive method of getting the analytical solution which is the aforementioned Gaussian convolution. However because we have a grid sampled potential field, it is not enough to simply convolve with a sampled Gaussian. To do this thoroughly one needs to solve the discretised diffusion equation. Then the resulting convolution is no longer with a pure Gaussian but with a *discrete Gaussian*.

$$T(x_n; t) = e^{-t} I_n(t) \tag{5.3}$$

where $I_n(t)$ are the modified Bessel functions of integer order. The difference between the true discrete Gaussian and a sampled continuous Gaussian are the greatest when σ is small. This applies to both solving the discrete diffusion equation and doing scale-space analysis on a grid. Neglecting this numerical effect on the WG model, results in wiggly shock fronts.

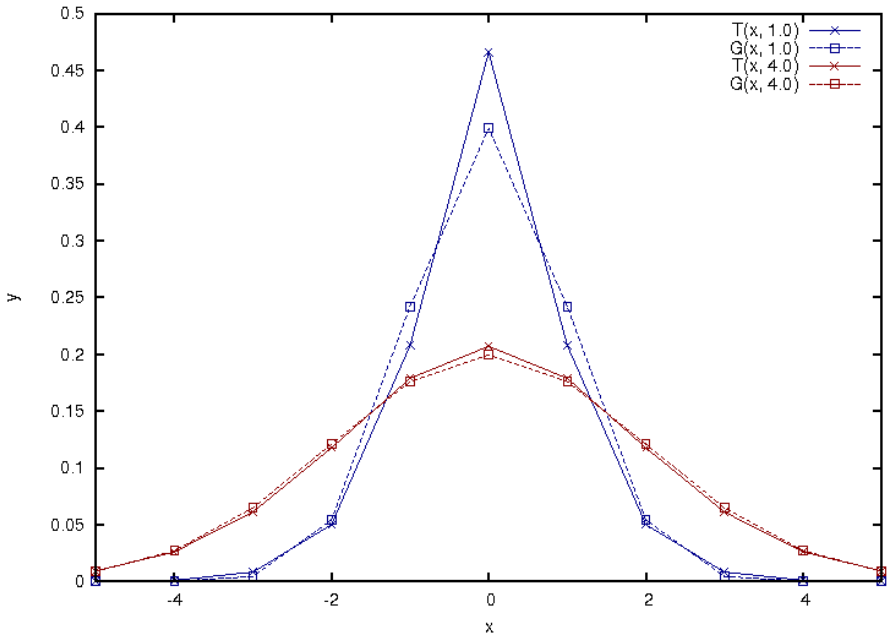

Figure 5.1: Discrete Gaussian kernel: This figure shows the difference between the sampled and discrete Gaussian kernels.

To do the convolution in the Fourier domain we need the Fourier transform of the kernel T(n, t)

$$\hat{T}(k, t) = e^{t(\cos k - 1)} \tag{5.4}$$

5.4 Fast Legendre Transform

There are several packages available on the web that compute a convex hull. One of the best ones is part of CGAL (cga). However, these are not entirely suitable to perform a Legendre transformation on a grid, since they are based on triangulations. These tend to become degenerate on a perfect grid. One solution is to offset each particle by a tiny amount. Yet conventional algorithms are not optimized for a gridded situation, since they are made for problems with point sets that occupy the full variety of their n-dimensional space. A faster algorithm was presented, in detail, by Noulez & Vergassola (hf. NV) (Noullez and Vergassola, 1994). It uses the fact that the Lagrangian map is monotonic

$$\text{if} \quad x_a \leq x \leq x_b \quad \text{then} \quad q_a \leq q \leq q_b$$

or in case of larger dimension, more precisely

$$(\boldsymbol{q}_b - \boldsymbol{q}_a) \cdot (\boldsymbol{x}_b - \boldsymbol{x}_a) \leq 0$$

It is important to realise that the monotonicity relation is true, even componentwise. Then, finding the Legendre transform can be done using an incremental algorithm not dissimilar to the Fast Fourier Transform. We start in the middle, finding the map $x \rightarrow q$ on one axis, thereby splitting the search area for the following part in two. Then repeat this process on increasingly smaller searching areas. The algorithm has a running time $O((N \log_2 N)^d)$.

5.4.1 Sub-pixel post minimization

We saw previously that the Eulerian and Lagrangian perspectives embody two different discretisations, that of volume and mass. The initial conditions are both; or to put it more precisely: during the linear stage of structure formation, the distinction between Lagrangian and Eulerian coordinates is superfluous. Yet we can assign two meanings to this data. Either we have velocities or spacial deformations of mass elements, or we have the change in density of volume elements. In the Lagrangian case this gives us non-discretised (or floating point) information on the location of each individual particle. In the Eulerian case this should then give us floating point density maps. However, the NV algorithm transforms discrete coordinates only. If we calculate the Legendre transform of the Lagrangian potential using FLT, the result is a map from integer to integer vectors. This is in fact a waste of information since we should be able to extract a map from integer to floating point vectors.
To resolve this, we added a second minimization step to the algorithm using a interpolation of the potential. The minimum within the LT would shift on sub-pixel level due to the xq term in the LT. Thus it is meaningful to find this

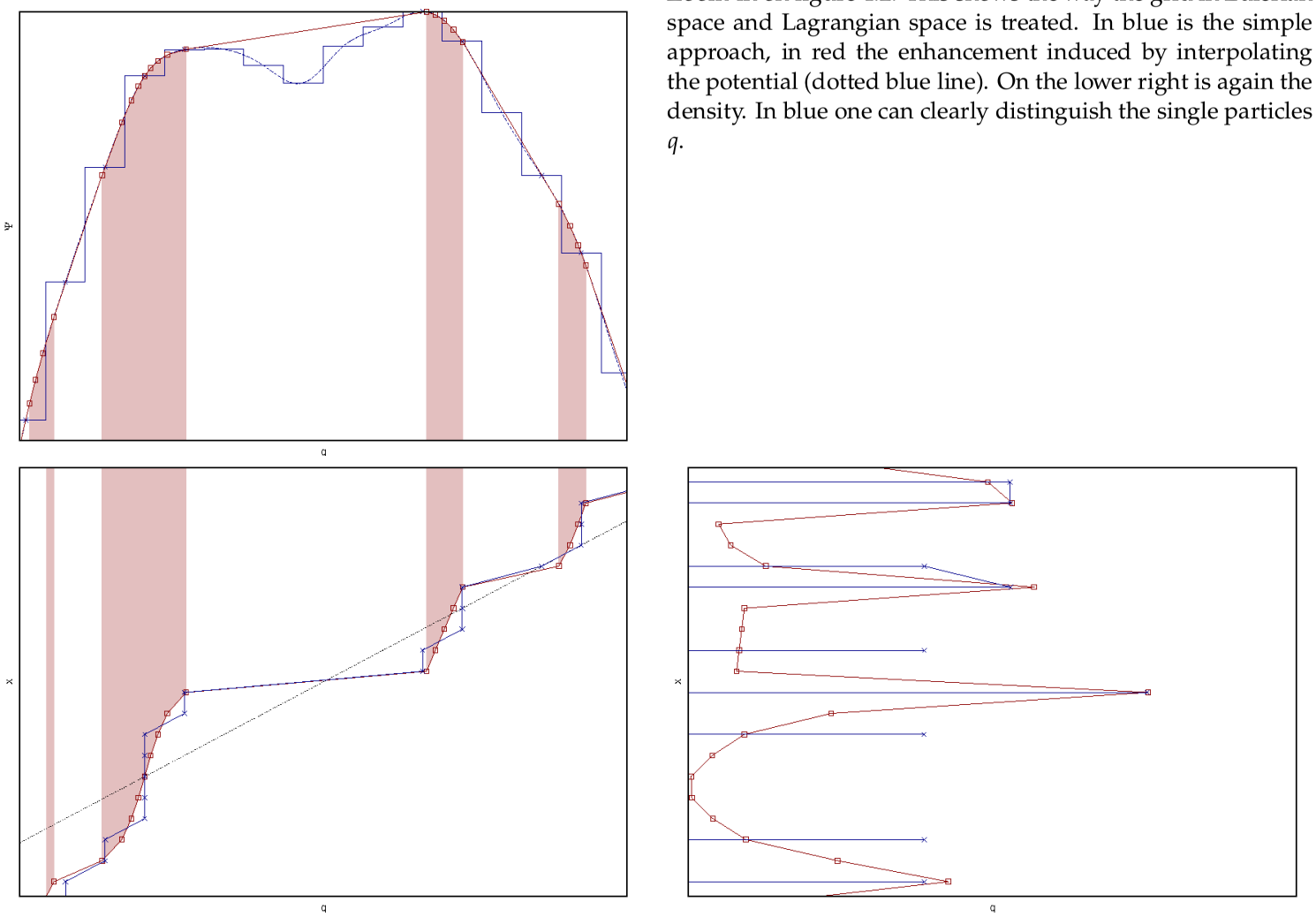

Zoom-in on figure 4.2. This shows the way the grid in Eulerian space and Lagrangian space is treated. In blue is the simple approach, in red the enhancement induced by interpolating the potential (dotted blue line). On the lower right is again the density. In blue one can clearly distinguish the single particles q.

Figure 5.2: Enhanced convex hull.

shift, but this would not work if we didn't have an interpolation routine that is continuous in the first derivative. We use a cubic spline routine which is described in the appendix.
To illustrate the effect of this step, we present the a figure in the same setup as figure 4.2. We should stress that this method is *not* fast[3] and we feel it has room for improvement in efficiency, especially in the 3D case where the interpolation involves matrix multiplications of rank 64. However, as can be seen in figure (5.4), the results are stunning.

Every N-body algorithm has a limited resolution, one way or another. Whenever a large number of particles assemble on a small area, this becomes a problem. This problem is fundamental to any model that needs to discretise mass as well as volume for performance reasons. By interpolating the potential we assume a smooth initial conditions on the smallest scales. The initial conditions of a cosmological simulation have the property that the discretisation in terms of mass is identical to that of volume. When performing a Legendre transform to get the map $\mathcal{E} : \boldsymbol{x} \mapsto \boldsymbol{q}$, we *choose* the volume-discretisation. Using the technique of sub-pixel optimisation we break the mass discretisation. Shocks however are still infinitely thin. Their location is known only at pixel precision, but their masses are accurate. The other way around we can *choose* the mass-discretisation and end up with the Lagrangian map $\mathcal{L} : \boldsymbol{q} \mapsto \boldsymbol{x}$. This will give us the exact location of a shock on a precision smaller than the pixel width, but the mass will have an uncertainty. We could raise the question of how we can know the exact location of a shock if we don't know if a certain particle belongs to the shock or not. The sticking of this particle would change the velocity of the shock slightly, thus knowing it's "exact location" becomes meaningless.

[3] a 256^3 particle model takes $\sim$ 30 min to complete the FLT on a single core. The post-optimisation stage takes 2 to 3 hours for a reasonably smooth model.

5.5 Density

Having monotonicity in the Lagrangian and Eulerian maps, means that calculating densities has become much easier than in N-body simulations. There are multiple ways of finding the density, but the best behaving seems to be to calculate the Jacobian of $\mathcal{E} : \boldsymbol{x} \mapsto \boldsymbol{q}$.

$$\frac{\rho}{\bar{\rho}} = \det J_{\mathcal{E}} \equiv \det \left[\frac{\partial q_i}{\partial x_j} \right]$$

Care needs to be taken when using the discretised version of this formula. In 2-D the determinant represents the area of the parallelogram spanned by the derivatives $\partial q_i / \partial x_j$. But on a grid this area will not be a parallelogram but a more general convex quadrilateral. In practice the effect will be *worst case* as the quadrilaterals will evolve towards triangles (the faces of the convex hull).

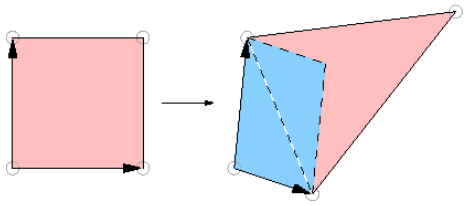

Figure 5.3: Calculating the determinant of the Jacobian gives the area of a parallelogram (blue), yet on a grid we need to have the area of a convex quadrilateral (pink).

In three dimensions the problem (as usual) gets more complicated: the general hexahedron is degenerate. There is in general no single unique polyhedron given eight points in space. There are two common choices to break this degeneracy. The *long diagonal* method splits the hexahedron into six tetrahedra. This has the downside of adding a preferential direction. The *tetrakis hexahedron* defines an additional vertex at the barycentre of each face. Efficient algorithms to calculate the volume of these polyhedra can be found in (Grandy, 1997).

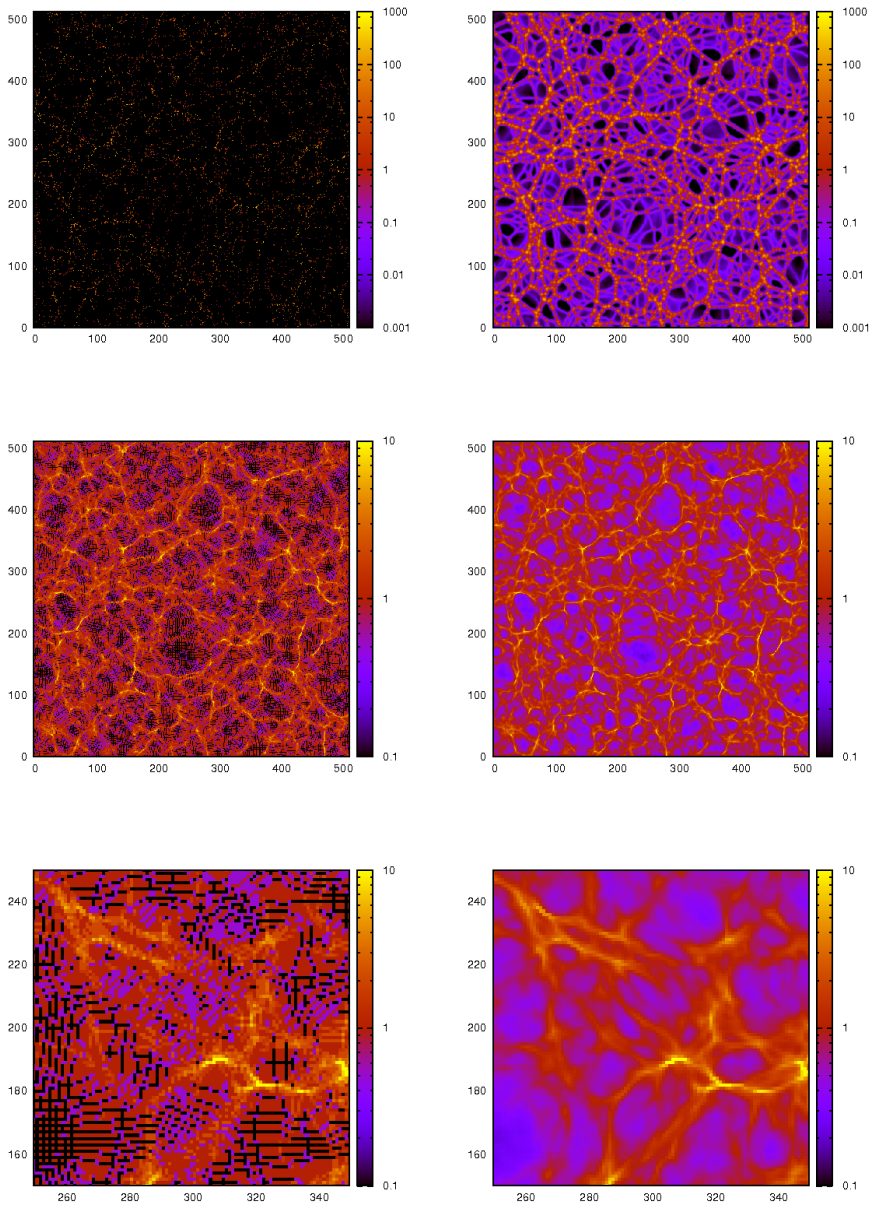

Figure 5.4: Smooth 2-D density maps: on the right we see the enhanced versions of the images on the left. From top to bottom: scale free scenario with n = 0, the enhanced version is also filtered with a Gaussian to show the clusters more clearly; in the middle an early snapshot from CDM initial conditions; on the bottom a zoom-in on the previous CDM density map.

Chapter 6

Hierarchical evolution of the Cosmic Web

We can now study the dynamics of the cosmic web from the two different perspectives, we discussed earlier. In this chapter we will qualitatively describe the phenomena seen in 2-D simulations. In three dimensions the dynamics will no doubt be more complicated, but also harder to track.
Every component (be it cluster, filament, wall or void) has its representation in Lagrangian space as well as the familiar Eulerian forms (see figure 6.1). We will look at each of these components and see what we can learn from the interplay between both representations.

6.1 From Voronoi to Adhesion

6.1.1 Voronoi model

If we make a contour plot of the potential along with the quasi Voronoi diagram, we can see the connection between the adhesion model and the Voronoi model of the LSS (Icke and van de Weijgaert, 1987). Suppose we have a potential corresponding to a sparse void sample with equal weight, then the adhesion tessellation will match the Voronoi tessellation of this point sample. In this sense adhesion can be seen as a generalisation of the Voronoi model. Scale free models with rising power slope, will evolve as a weighted Voronoi model with weights that change with time (see figure 6.2).

The link between adhesion and the Voronoi model can find an application if we compare the model of the *flow complex* (Giesen, 2008) with the work of Bogaevsky (2004). One conclusion that can be drawn from these mathematical

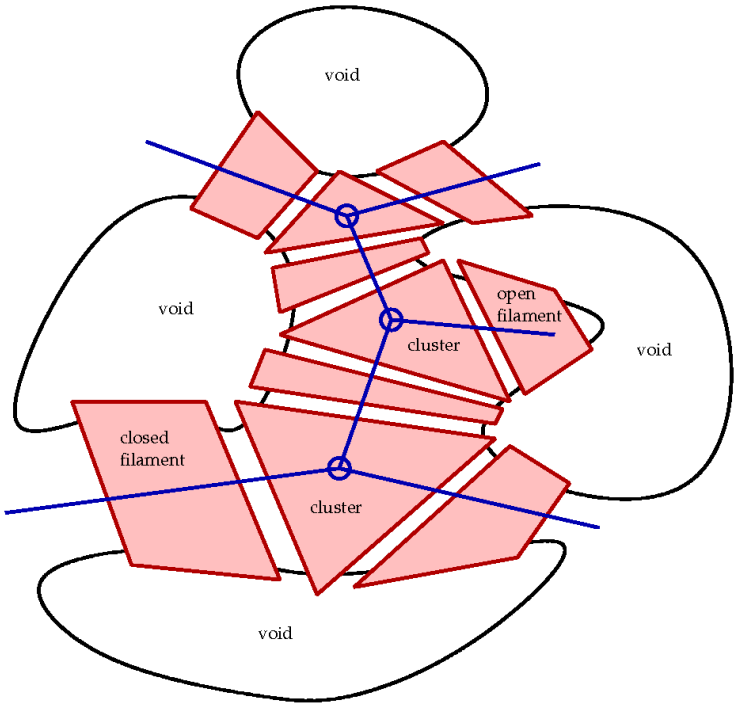

Figure 6.1: the Cosmic Web in Lagrangian view: Different elements of the cosmic web (blue) superimposed over their Lagrangian representation (red).

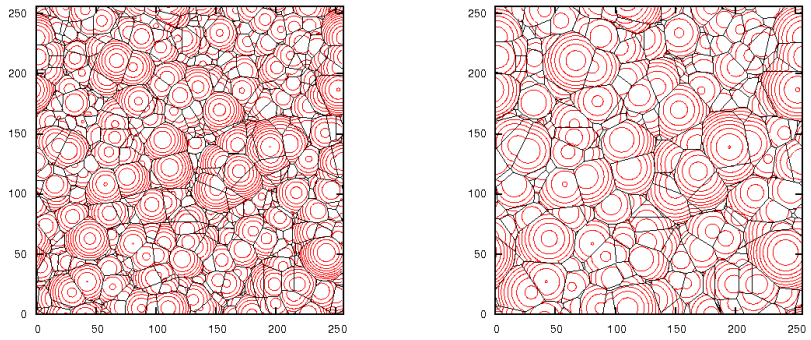

Figure 6.2: Comparison with Voronoi model: Two time frames of a scale-free model. Plotted are the adhesion tessellation over a contour plot of the potential. Note the similarity with the definition of a weighted Voronoi tessellation.

models is that there won't be a stable cluster at every vertex of the Cosmic Web. If a Voronoi node is not inside it's dual Delaunay face, it will only act as a "way-point" trafficking clumps of matter to their destination. It gets interesting when a stable cluster evolves into a way-point.

Just as the Voronoi model is equipped with a dual representation (the Delaunay triangulation), adhesion has the Legendre duality between Eulerian and Lagrangian representations.

6.1.2 $\mathcal{EL}$-Duality

We sketched a system where the transitions between Eulerian and Lagrangian space is formalised by the Legendre transform. This formalism was illustrated in one dimension, but to highlight the cosmic web, we need to move on to two spacial dimensions. The convex hull becomes three dimensional. In the mathematical language of Legendre transforms we say $\mathcal{L}$ and $\mathcal{E}$ are each others *dual*. Dual spaces have the property of turning points into planes and vice-versa (see figure 6.3).
If we look at the convex hull in the two dimensional case (this implies the construction of a 3D convex hull) we can see that a point singularity corresponds to a single face on the convex hull. All the mass (or every particle) associated with the face has collapsed to that single point. The other way around a single vertex of the convex hull in Lagrangian space corresponds to a certain volume in Eulerian space. If we plot a graph of this construction we find a Voronoi-like tessellation in $\mathcal{E}$ where the edges correspond to the filaments otherwise found in the density distribution, while in $\mathcal{L}$ we find something resembling a Delaunay triangulation. As we can see in figure 6.3, adhesion has buried in it's formalism the spine of the cosmic web. From the Voronoi model onward we can make the adhesion model more complicated by using a smooth potential.

6.1.3 Smooth potential models

In the case of a smooth potential (e.g. CDM), there are some features added to the duality relationship. There will be connected patches of the potential that are part of the convex hull; these are the free-streaming regions where the Zel'dovich approximation still holds. In the Lagrangian representation we find an "archipelago" of voids, true island universes. Also there are multiple ways the convex hull reconnects with the potential from singular regions. For example a filament is recognised on the convex hull as a region with curvature in one direction only. But contrary to the picture before, a filament does not need to connect to clusters, it can dissolve into the void. (Frisch and Bec, 2001) During decay the Lagrangian area (mass) of the voids shrink. They evolve towards point size, which brings us back to the previous models. We

see an evolution from a universe where structure starts to grow in patches asymptotically towards a fully connected Voronoi model.

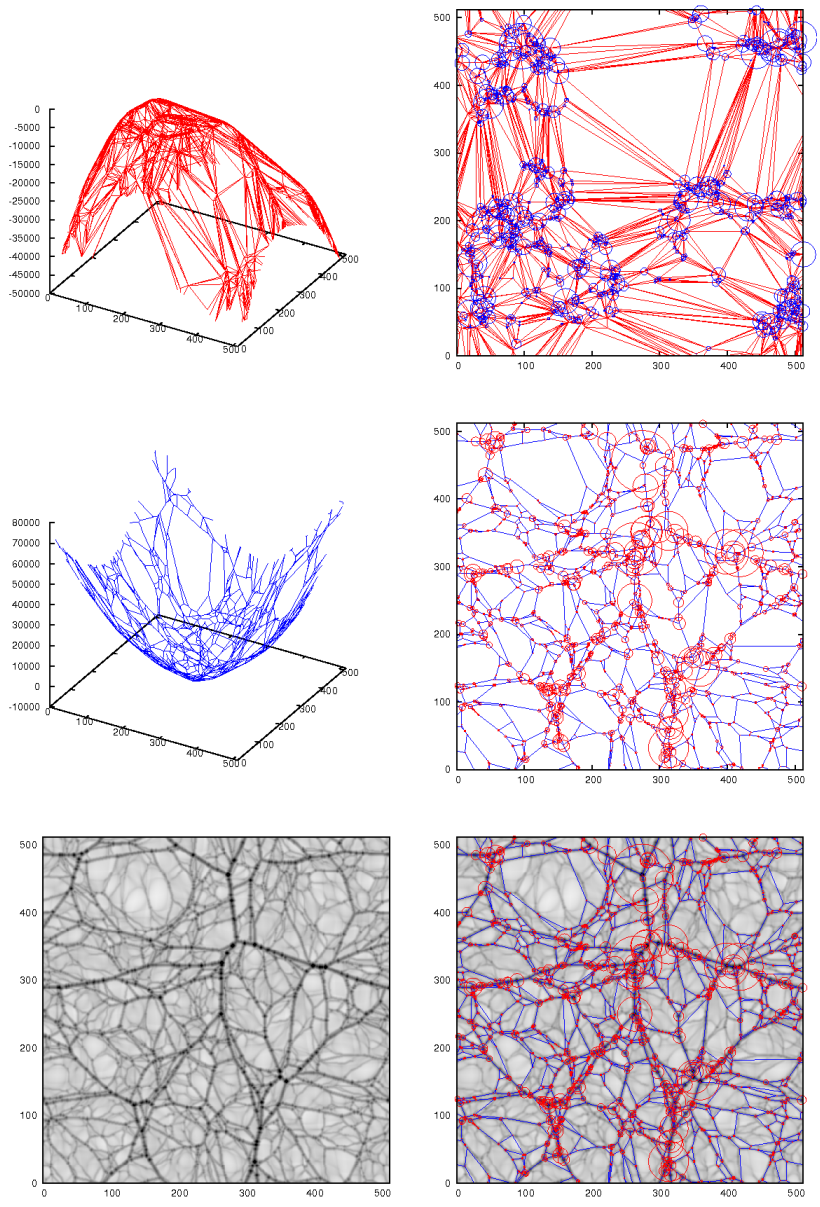

Figure 6.3: From convex hull to cosmic spine: Self-similar model with $n = -0.5$, Shown on the top are the convex hull φ_c and its triangulation, where circles are void volume. In the middle is the Legendre transform H and the belonging tessellation, where circles are cluster mass. The bottom two panels show the density with the skeleton superimposed.

6.2 Geometric analysis

We saw in the previous paragraph how the cosmic spine was embedded in the adhesion method. Actually finding all the singularities and building the web, is not a trivial task. We describe step by step how we get from the computation of a Legendre transform to the solid knowledge of the inner structure of the web, allowing us to calculate numerous statistics. This is not possible if we have merely an image or a density distribution. First we give mathematical concepts that define the spine in adhesion theory, then we illustrate these using discretised versions of these concepts on a simulation. In this we are helped by the fact that we have a sub-pixel precision Eulerian map, which enables types of analysis that are not feasible on a coarse grid.

6.2.1 Mathematical definitions

We assume Eulerian and Lagrangian spaces $E, L \subset \mathbb{R}^n$, $\boldsymbol{x} \in E$ and $\boldsymbol{q} \in L$. Previously we defined the maps

$$\mathcal{E} : \boldsymbol{x} \mapsto \boldsymbol{q}$$

and

$$\mathcal{L} : \boldsymbol{q} \mapsto \boldsymbol{x}.$$

This does not mean $\mathcal{E}$ and $\mathcal{L}$ are each others inverses, as in all interesting cases $\mathcal{L}$ is not invertible. Also in the case of sharp horned initial conditions [1] $\mathcal{E}$ is not invertible. In this case the maps can be referred to as a "Devil's Staircase" (Vergassola et al., 1994).
The range of a map gives us the set of coordinates it maps to.

Definition 1 (Range) *Given the mapping $\mathcal{M} : \boldsymbol{x} \mapsto \boldsymbol{q}$ the range of $\mathcal{M}$ is defined as*

$$R_{\mathcal{M}} = \{\boldsymbol{q} \mid \exists\, \boldsymbol{x} : \mathcal{M}(\boldsymbol{x}) = \boldsymbol{q}\}\,.$$

Note that if a particle $\boldsymbol{q} \in R_{\mathcal{E}}$, does not mean that it is a free particle, it can also lie on the boundary of the set of free particles. The range can also be expressed in terms of the convex Lagrangian potential φ_c: let $Q \subset L$ be the set of points for which $\varphi_c = \varphi$, that is, the set of "anchor points" of the convex hull. The range $R_{\mathcal{E}}$ is the closure (interior plus boundary) of Q.
Two volume elements are said to belong to the same *tile* (element of the tessellation) if there is a path connecting the two in Lagrangian space:

Definition 2 (Tile) *Let $\boldsymbol{q}_1 = \mathcal{E}(\boldsymbol{x}_1)$ and $\boldsymbol{q}_2 = \mathcal{E}(\boldsymbol{x}_2)$. If there exists a continuous path $\gamma(\boldsymbol{q}_1, \boldsymbol{q}_2) \subset R_{\mathcal{E}}$, then $\boldsymbol{x}_1$ and $\boldsymbol{x}_2$ are in the same tile.*

[1] $P(k) \propto k^n$, where $n > 0$

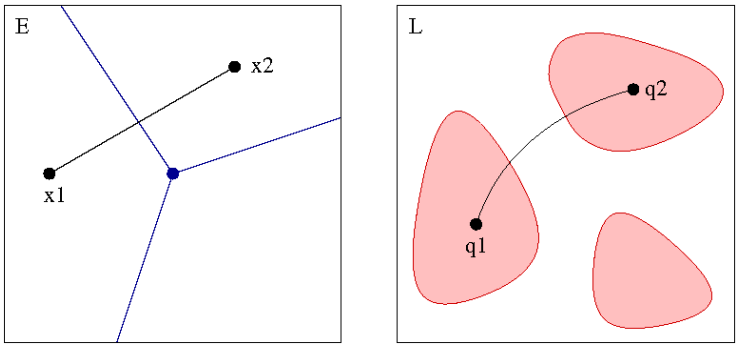

Figure 6.4: Tessellating E: there is no connected path between $\boldsymbol{q}_1$ and $\boldsymbol{q}_2$ that lies completely in $R_{\mathcal{E}}$ (pink)

Definition 3 (Tessellation) *The set of all tiles of $\mathcal{E}$ is the tessellation of $\mathcal{E}$. The tessellation is space filling. This means that every element of E is also an element of exactly one tile.*

The following definition classifies *closed singularities* as the boundary between two or more tiles: A point $\boldsymbol{x}$ belongs to a connected singularity if every neighbourhood of $\boldsymbol{x}$ has members of different tiles. However, there exists singularities that do not separate regions in $R_{\mathcal{E}}$. To classify these we need a better definition.

Definition 4 (Singularity) *Let X be an infinitesimal neighbourhood around $\boldsymbol{x}$ (say an area with radius $\epsilon > 0$ around $\boldsymbol{x}$). If $Q = \mathcal{E}(X)$ is not connected, $\boldsymbol{x}$ belongs to a singularity. The number of connected regions in $Q \cap R_{\mathcal{E}}$ indicates the dimensionality of the singularity.*

As with the range, the singularity can also be defined in terms of the convex hull. If ϕ_c has a vanishing second derivative at a point $\boldsymbol{q}$

$$\det\left[\frac{\partial^2 \phi_c}{\partial q_i \partial q_j}\right] = 0,$$

there is a singularity. In this case $\boldsymbol{q} \notin R_{\mathcal{E}}$ and $\boldsymbol{x} = \mathcal{L}(\boldsymbol{q})$ must be a singular point on $\mathcal{E}$. This time the multiplicity of the eigenvalue $\lambda = 0$ indicates the dimensionality of the singularity.

6.2.2 Numerical implementation

In practice, using derivatives to find singularities results in number loss. The best way to find the skeleton is using the map $\mathcal{E}$ directly. The definitions that are given above are easily portable to discrete maps. The main difficulty lies

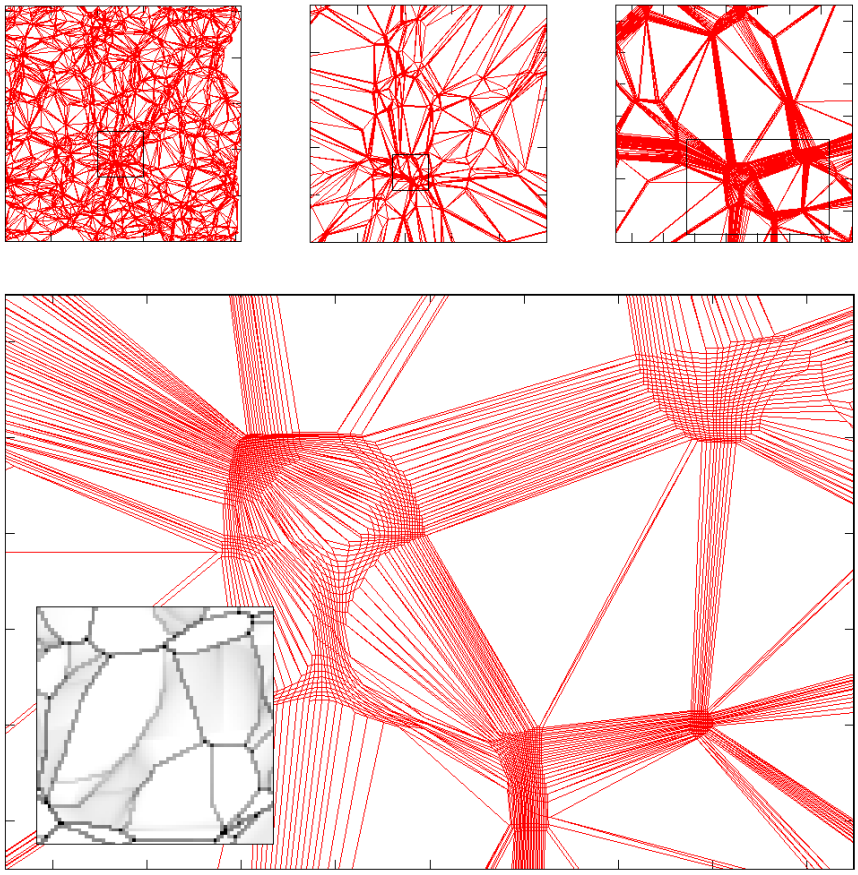

Figure 6.5: Grid deformation of $\mathcal{E}$: zooming in on the Eulerian map of a 2-D scale-free simulation, we clearly see the clusters as triangles, filaments as lines and voids as the knots where lines meet. If we zoom in further, we can see the pixel structure of the original grid. Void pixels are still more or less square, while filaments are extremely elongated and clusters pixels evolve towards near triangle quadrilaterals. We can also see that the Lagrangian structure of the voids are much more fine-grained than the pixel size. The inset shows the corresponding (logarithmic) density map.

in the concept of connectedness. In the case of a point sample, connectedness can only be defined on the basis of a certain threshold. It seems natural (and easy to implement) to pick the pixel size as a constraint. A connected region is then found using a simple *flood fill* algorithm. However as we can see in figure (6.2.2) the structure of the map is often smaller than the pixel size. Even using pixels there are multiple kinds of connectivity, two examples illustrated in figure (6.6).

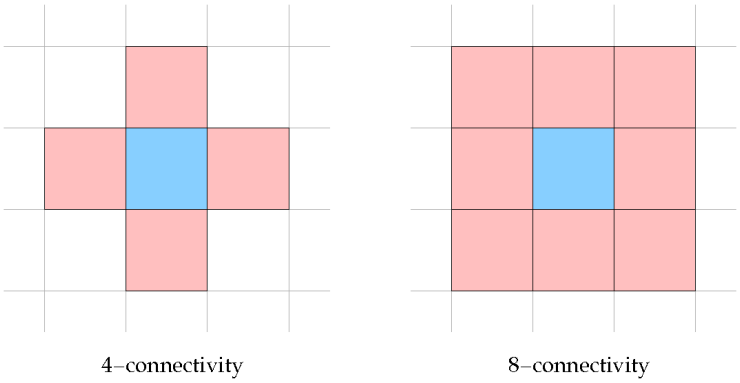

Figure 6.6: Pixel connectivity: given a grid of pixels, even the concept of a neighbour is open to discussion. The most used examples of 4- and 8-connectivity are illustrated here.

Probably the best way to find morphological features in this map, would be to look for contrasts in the shape of the quadrilaterals. For example, the two voids on the lower right part of the largest panel in figure (6.2.2) would be connected if we only look at the pixels they occupy. Yet they are separated by a decent filament. Once we agree on a method for computing connectedness, the translation of the above definitions becomes straight forward. An infinitesimal neighbourhood can be approximated by a group of four (or in 3-D: eight) points spanning a single volume element. The fact that connectedness has a flexible definition when it is applied to point samples, does not have to be a draw back. If we vary the threshold, we can study the behaviour of the outcome under this variation. An example of this can be found in *alpha shapes* (Edelsbrunner, 2010, see).
For the moment we will restrict ourselves to simple grid based connectivity. The results of the procedure (using 4-connectivity on a grid) are illustrated in figure (6.7).

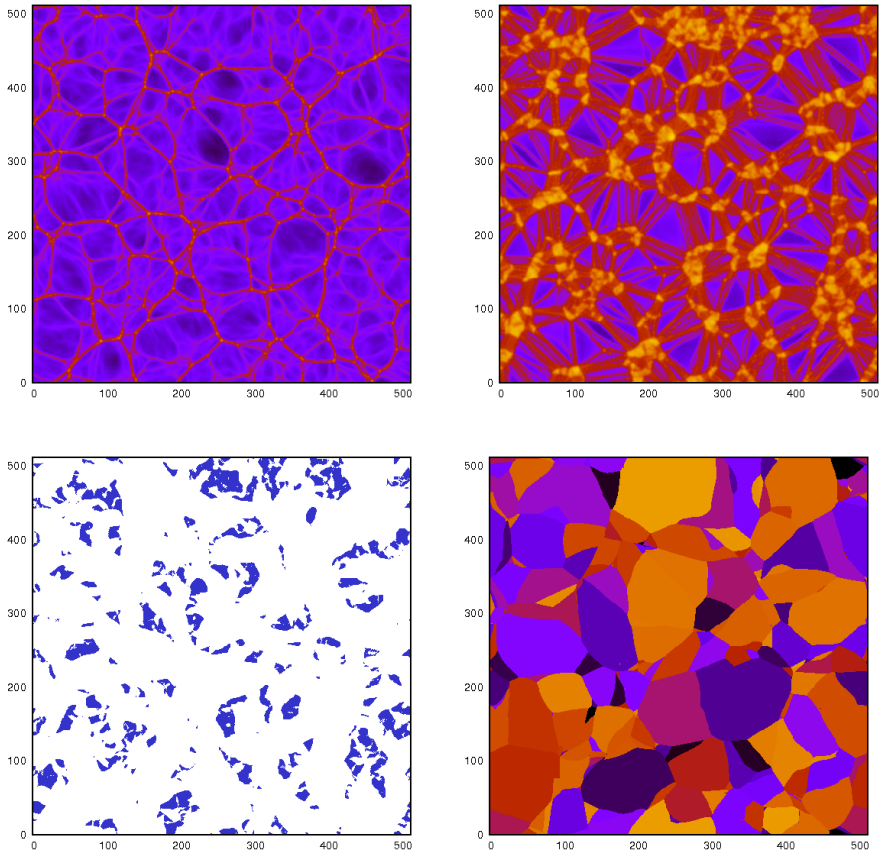

Figure 6.7: Adhesion tessellation: Using the output of a 2-D CDM simulation, we can find the adhesion tessellation. In the top-left panel is the density (logarithmic color); the top-right panel is the Lagrangian volume density. The bottom left panel shows the range function $R_{\mathcal{E}}$ and in the last panel we see the tessellation, with each tile given a random color.

6.3 Voids

Expansive voids are the dominant driver of the evolution of the Cosmic Web in adhesion. Adhesion theory naturally contains an intuitive definition of a void; simply a non-singular connected region. We might think of void as a more or less spherical under-density; while in reality voids (and as defined in adhesion) can have much more complicated shapes and non-trivial topology (Platen et al., 2007).

6.3.1 Void definitions

Voids are commonly understood to be cosmic under-densities; but the hierarchical nature of the large scale structure makes it hard to put a lower boundary on the concept of a void. Also a void embodies an important dynamical concept, that of gravitational repulsion, which would lead us to define a void in terms of divergent velocity fields. It is therefore useful to say something on the properties of voids to get an idea of the difficulties when comparing different studies into the matter.

Simple voids Simple voids have a single centre, spherical topology, divergent velocity field. This can be understood to represent the ”classic” idea of a void. Such a void is surrounded by a shell of denser matter: walls, filaments and clusters.

Extended voids Extended voids are voids with a non-trivial topology. One case would be a void in the shape of a torus, which can still have a divergent velocity field; but another case of an extended void is a void with a cluster in its centre. The velocity is no longer divergent throughout the void, but from outside the dynamical influence of the object still is that of a void. We could say that we should be able to create a shell near the boundary of the void through which the velocity field is divergent.

Super voids Super voids are the void equivalent of super clusters. They are so rich in substructure that we can identify smaller voids within the super void.

The difference between the definitions can be very important when considering void merging. In adhesion theory once a structure is collapsed it will only dissipate slowly; even worse, in the Lagrangian view, regions once separated will never rejoin. Once stuck, a particle cannot ’unstick’. We can however adapt our definition to our interpretation of what we think a void is. This has the downside of adding threshold parameters, making unbiased void detecting more difficult.

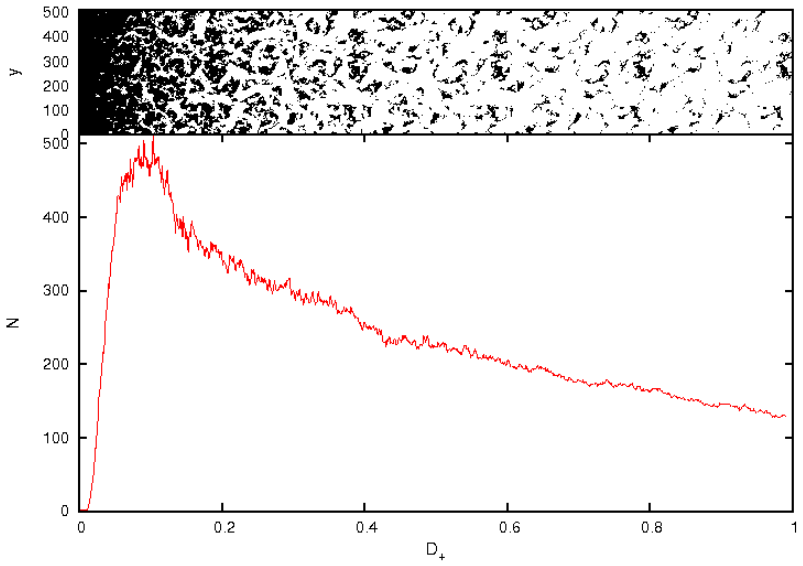

Figure 6.8: Number of voids as a function of time: On the top panel we show the Lagrangian view of collapsed vs. free particles. Free particles are shown in black.

6.3.2 Percolation theory

Percolation analysis was advocated by Shandarin (Shandarin, 1983)(Klypin and Shandarin, 1993) as a way of measuring the connectiveness of the cosmic web. The Universe starts with no structure. There are only free-streaming particles, so we consider the Universe as one big void. Then in patches structure starts to form. Slivers of filaments start to grow until they connect. We can see this happen if we look at the map of stuck/free particles in Lagrangian coordinates. We move from a universe connected by under-densities to one connected by over-densities. While this is a relatively straightforward picture in 2-D, in 3-D the connectivity of over-dense and under-dense regions don't exclude each other. Rather the topology of the cosmic web will be that of a sponge, as was shown by Gott et al. 1986 (Gott et al., 1986). This will make it more complicated to perform an analysis of the void tessellation in 3-D.

6.3.3 Void sociology

In the evolution of the cosmic web we see voids continuously expanding at the expense of weaker voids. If we look at this process in Lagrangian coordinates we see voids evaporating by mass-decretion, their particles slowly joining the surrounding filamentary structures. We can describe the life of a void from

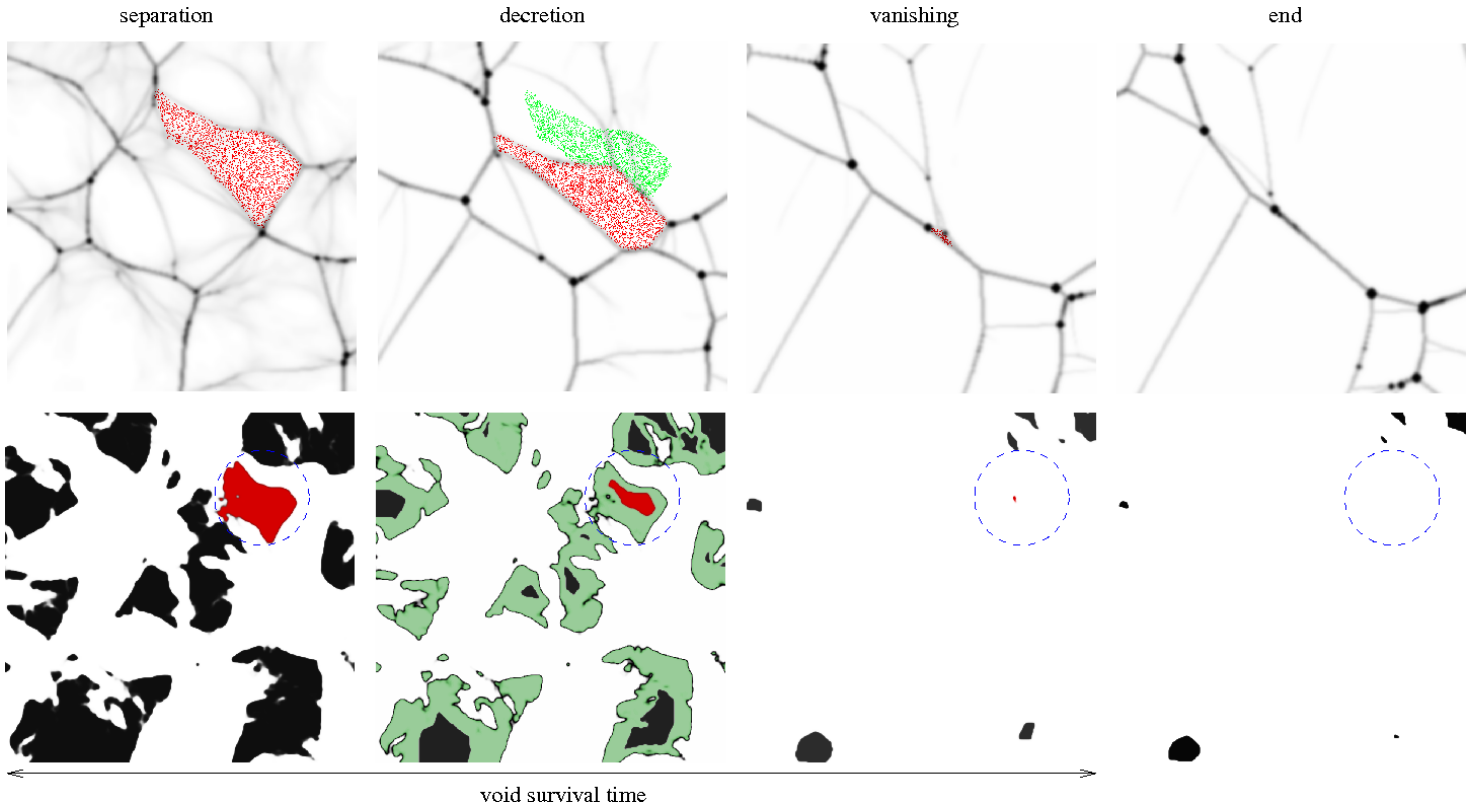

Figure 6.9: The life of a void: In this illustration we can follow the life of a void, from the first moment it uncouples from a larger void to its final death after continuous decretion, squashed by its surrounding clusters and filaments. The size of a region in Lagrangian space gives the total mass contained while the size in Eulerian space of course gives the volume.

the moment it is separated from it's parent void to it's collapse between the surrounding over-densities. This is illustrated in figure 6.9 As we see matter streaming out of voids, substructures attenuate. This could result in void merger, but we don't see this in our simulations.

6.3.4 Alignment

Also visible is the alignment of structures within larger voids. When a void gets squashed, the filament survival is greater if the filaments are oriented orthogonal to the direction of squashing. Also the other way around, substructure can get stretched by the larger scale motions, also resulting in alignment. The effect was previously discussed in (Platen et al., 2008), where it is ascribed to the large scale tidal forces.

6.4 Wall dynamics

The type of processes that occur in LSS formations depend on the dimensionality of the structure. We have identified voids as regions where particles are free-streaming in three dimensions. Then particles will hit a wall, streaming in two remaining free directions, until it is captured by a filament, after which it ends up in a cluster. This picture of environmental history can be seen most beautifully when we take three thin slices out of a simulation box that are aligned with a wall. We can see the result in figure 6.10. The slice was extracted upon visual inspection of the simulation box. In the edge-on view we see particles raining down on the wall from the surrounding voids. These then stream towards the filaments and finally end up in clusters. In this process the wall shows fragmentation into several thin filaments.

This is an example where adhesion correctly models the stream of matter from voids to clusters. It should be noted that this motion is internal to the structures that are themselves evolving much slower. It is often mentioned in the literature that adhesion breaks down inside singularities (Shandarin, 1995, for example). We must conclude that at least in this case, adhesion does give a good description of dynamics within a wall. Of course, to be sure, we would have to compare this with a real N-body simulation.

6.5 Merging and fragmentation of clusters

A prediction of Cosmic Web theory (Bond et al., 1996) is the dependence of the number of filaments connected at a cluster with its mass. In 3-D an adhesion cluster has four joining filaments by definition. In a real simulation when two clusters with four filaments each meet, they will join. The new cluster will

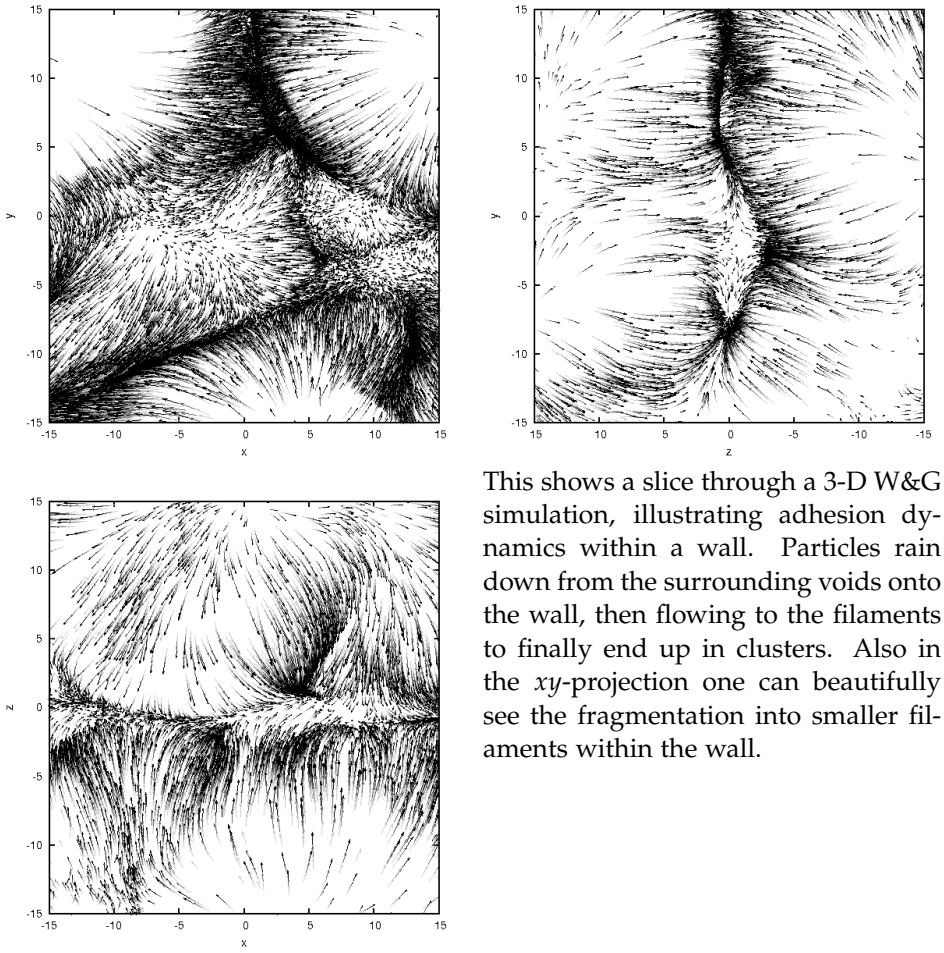

This shows a slice through a 3-D W&G simulation, illustrating adhesion dynamics within a wall. Particles rain down from the surrounding voids onto the wall, then flowing to the filaments to finally end up in clusters. Also in the *xy*-projection one can beautifully see the fragmentation into smaller filaments within the wall.

Figure 6.10: Wall dynamics in face-on and edge-on views.

have (at least temporarily) six filaments. In adhesion this won't happen. As Bernardeau and Valageas (2009) showed, if we look at a 2-D simulation, two clusters cannot join. They will merge and fragment, two new clusters going more or less opposite ways, orthogonal to the merging direction. Clusters will only merge if they are the complete set of clusters spanning a vanishing void. In 3-D, two clusters merging, will fragment into three new clusters and vice versa; four clusters (each the node of a tetrahedron shaped void) are needed to merge into a single cluster.

Chapter 7

Results

7.1 Simple statistics

The simplicity of adhesion allows us to perform statistics at resolutions that normally require supercomputers to compute. The simplest example would be the cluster mass function and the void volume function.

7.1.1 Void volume

To calculate the volume of a void, we use the Lagrangian map $\mathcal{L}$ as well as the Eulerian map $\mathcal{E}$. First we find the range function $R_{\mathcal{E}}(\boldsymbol{q})$. Then for each connected volume in $R_{\mathcal{E}}$ we calculate the volume. Shani et al. (1994) already calculated the same without having access to the more accurate sub-pixel mapping $\mathcal{L}$. Since fluid elements in voids have not entered a caustic, we can use ZA by our definition of a void. The volume is then given by

$$V_{\mathcal{E}} = \sum dV_{\mathcal{E}} = \sum_{i=1}^{N} dV_{\mathcal{L}} \prod_{j=1}^{d} \left[1 - D_{+}\lambda_j(\boldsymbol{q}_i)\right], \tag{7.1}$$

where N is the number of connected free volume elements, and d the dimension. (Sahni et al., 1994) The void volume function was calculated analytically by Sheth and van de Weygaert (2004). Using the adhesion tessellation we looked at the void volume distribution in a 3-D box with 256^3 particles, and initial conditions for a $1024h^{-1}$ Mpc simulation. This way we have enough resolution to find a cut-off in the distribution at larger scales. We fitted a Schechter function to find a characteristic scale length.

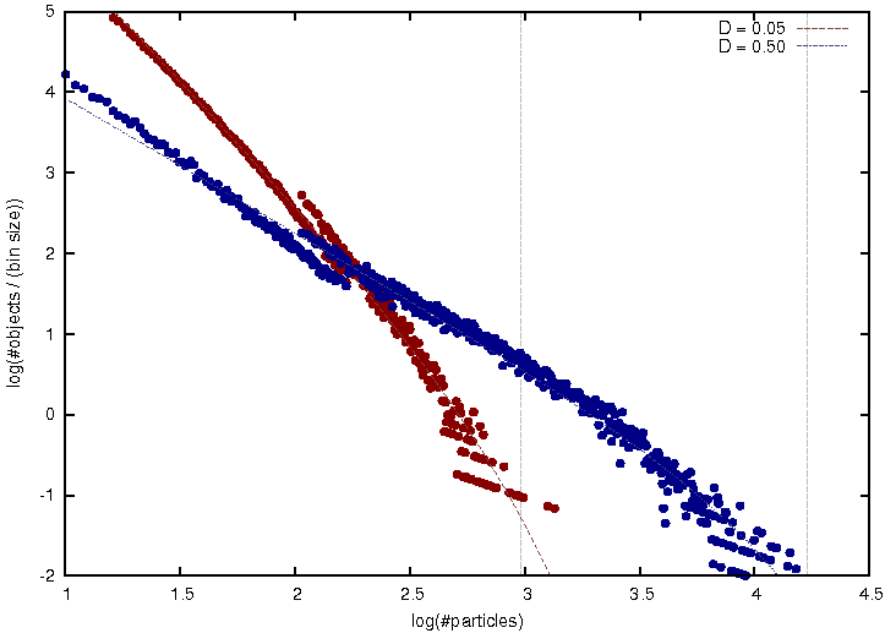

Figure 7.1: Cluster mass function at two time steps using 256^3 particles with 1024 Mpc CDM initial conditions. This graph includes all singularities without checking whether a particle is in a cluster or filament. The vertical lines indicate the characteristic masses.

7.2 Adhesion as a geometric tool

Other than using adhesion to study the evolution of the cosmic web, it can also be used to detect the web within time steps of an N-body simulation, or even on galaxy surveys like SDSS or 2dF. There are numerous algorithms available that do this (for example watershed (Platen et al.), MMF (Aragón-Calvo et al., 2007a) or skeleton finder by Sousbie et al. (2009)). Adhesion has the advantage of 'cleaning things up a bit' in the process. The down side is that adhesion can't help evolving the density distribution on large scales as well as the small scales. This could be cured by filtering the potential with a hi-pass filter. This also allows for a scale-space hierarchical approach to the problem. It is clear from figure (7.3) that the adhesion method is not able to pick out much detailed structure.

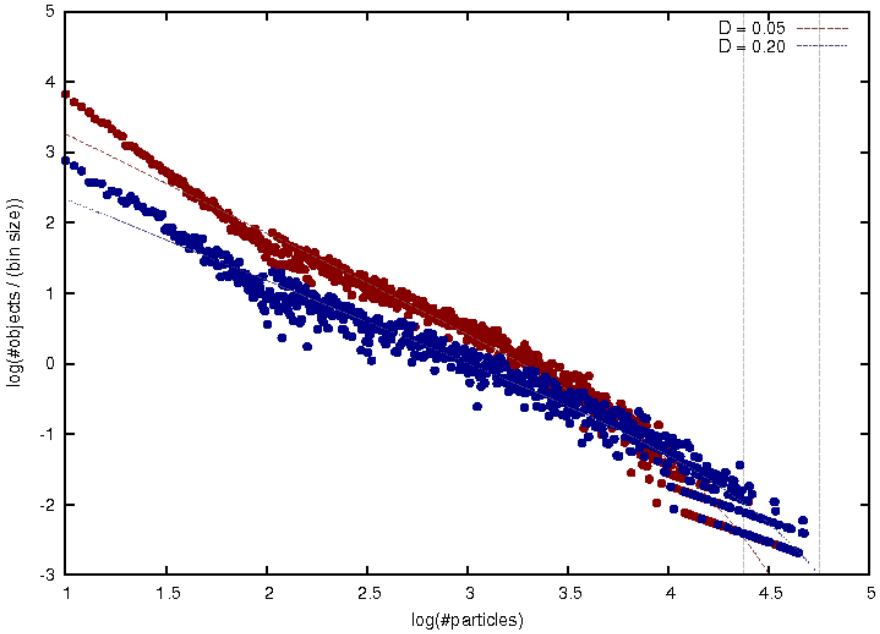

Figure 7.2: Void volume function at two time steps using 256^3 particles with 1024 Mpc CDM initial conditions. Voids become less numerous at later times, so the quality of the fit diminishes rapidly. The vertical lines indicate the characteristic volumes.

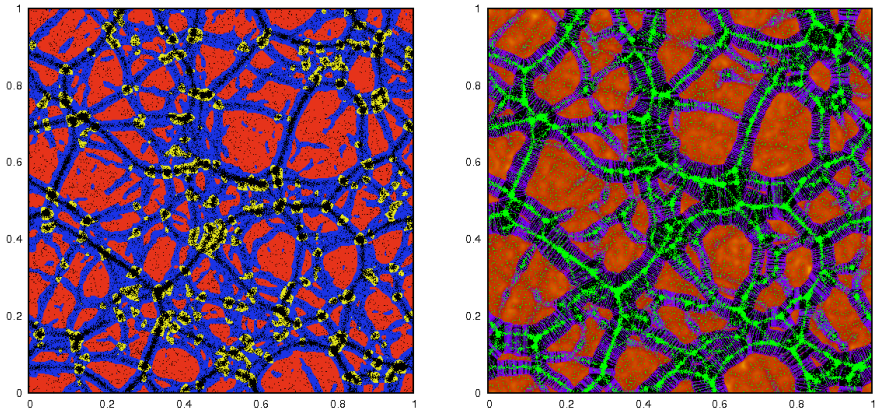

Figure 7.3: Adhesion shape finder: We created a mock sample from an adhesion time frame. On the left we coloured the area by the signature of the eigenvalues of the deformation tensor, as explained in the section on Zel'dovich approximation. On the right is shown the Lagrangian view after an appropriate time step.

7.3 Results on 2-D scale-free models

We now present some results on 2-D scale-free models. These results are illustrative for the possibilities in 3-D. We took a set of random phases and applied three different scale-free power-spectra to them. They were normalised by taking a common value of the power spectrum from the CDM spectrum at a fixed wavelength, such that the results show a nice evolution at a similar time-scale as CDM would give at that particular wavelength. We show results for three time-steps (at $D_+ = 0.1, 0.3, 0.5$). Where time-evolution is not shown we took the results for $D_+ = 0.3$. The density is plotted in figure (7.4). The colour coding is logarithmic, and the images are filtered with a small Gaussian, to show the clusters more clearly. The images clearly show the characteristic differences between the models of different power spectrum slope. The model with $n = 0.5$ shows dominant clusters and little hierarchy, where with decreasing n the filaments get more pronounced, and the large scale structure becomes more fractal. Also visible is the greater influence of large scale tidal fields in the model with $n = -0.5$. These observations are supported by the Lagrangian view of the same snapshots in figure (7.5). [1]

One of the more surprising conclusions would be, that the model with the least small scale power shows the most sub-structure. This can be explained, as models with high power in small scales will, on these scales, go non-linear much sooner. Thereby these small scale structures get destroyed by aggressively expanding voids; so to say there is a large transfer from small scale perturbations to large scale structures. On the other hand, models with dominating large scale modes will have some of their small scale structures destroyed in the collapse of larger voids, but within the surviving voids there will be richer substructure.

The most important difference with the theory of the Cosmic Web by Bond et al. (1996) is that the influence of the voids alone would be enough to recreate the Cosmic Web. Bond et al. show that the pattern of the cosmic web is already present in the initial conditions in the terms of the presence of rare events in in the medium. These events can be strong tidal configurations or Morse singularities in either the density or the potential. Based on the way adhesion builds the Cosmic web, we could say that this picture is not complete. The expansion of a set of ever stronger voids erases some of the structures that would have formed if the neighbouring void would not be there. On the other hand we have shown in the previous chapter, that the evolution of the cosmic web cannot be described by the expansion of the voids alone, as this leads to pathetic behaviour in the merging of clusters.

[1] To get a good feel for how the Cosmic Web evolves in adhesion theory, one should see the motion pictures that are available on the web: `www.astro.rug.nl/~hidding/go/go.html`. The medium of printed paper is not sufficient to capture all of the insights these videos purvey.

7.3.1 Filament strength

Cosmic web theory predicts a correlation between the length of a filament and its density. (van de Weygaert and Bond, 2005a) We did find a power-law relation between the density of a filament and the mass of the adjacent clusters in the 2-D scale-free simulations. This can be explained by the geometric configuration of the structures in Lagrangian space. Since the filament that connects two clusters share an edge with each of these in the Eulerian mapping, the density of the filament will depend on the cluster mass, by approximately a square root law. This correlation can be seen in figure (7.6), where we measure a power slope of $\gamma \approx 0.6$. This number stays constant for all models at all times. However we find no correlation at all between filament density and length, which we plotted in figure (7.7). Since this relation is a well tested prediction of Cosmic Web theory (van de Weygaert and Bond, 2005a; Colberg et al., 2005), we must conclude that adhesion theory is at flaw here, at least in the two dimensional case.
The correlation between cluster mass and filament density is reproduced by adhesion, but we have to ask ourselves if the mathematical reason behind it is indeed comparable with the physical reason it should have. Both the mass of the cluster and the density of the filament come from the strength of the neighbouring void.

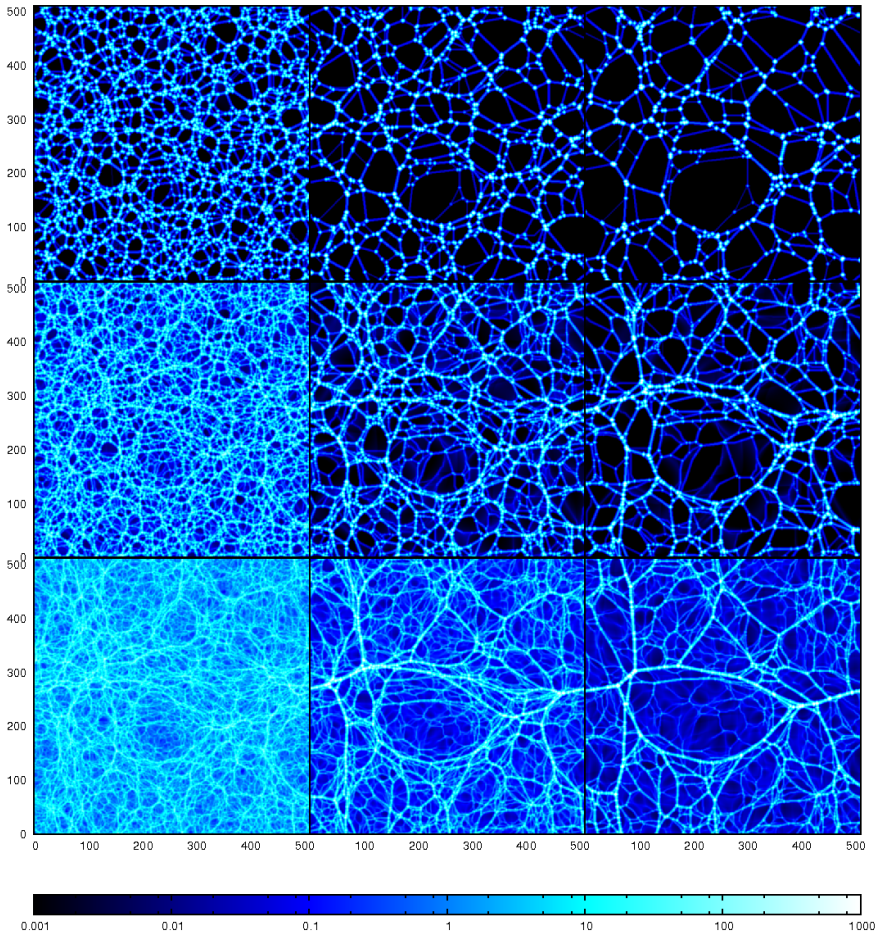

Figure 7.4: Mass density for scale-free models: Three different scale-free models (from top to bottom: $n = 0.5, 0.0, -0.5$, using the same random phases). We plotted the density filtered with a small Gaussian to bring out the clusters. From left to right there are three time-steps. Notice that the model with $n = 0.5$ has dominant clusters, and the large scale structure is dominated by features expanded from small scale initial perturbations, giving voids that tend to be spherically shaped. The $n = -0.5$ has more prominent filaments and the large scale structure is dominated by the tidal field of large scale initial perturbations.

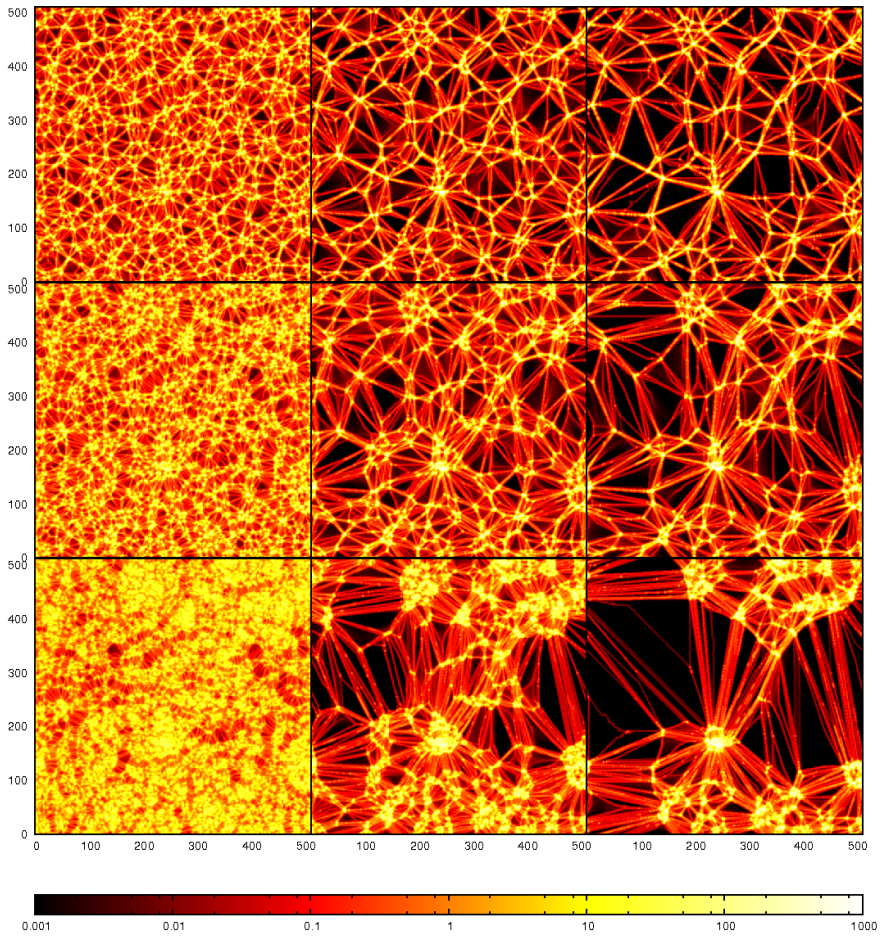

Figure 7.5: 2-D Volume density for scale-free models: this figure shows the same three models as in figure (7.4), now in Lagrangian "volume density" view. We see that though the $n = -0.5$ model has less clusters than the $n = 0.5$, they are heavier.

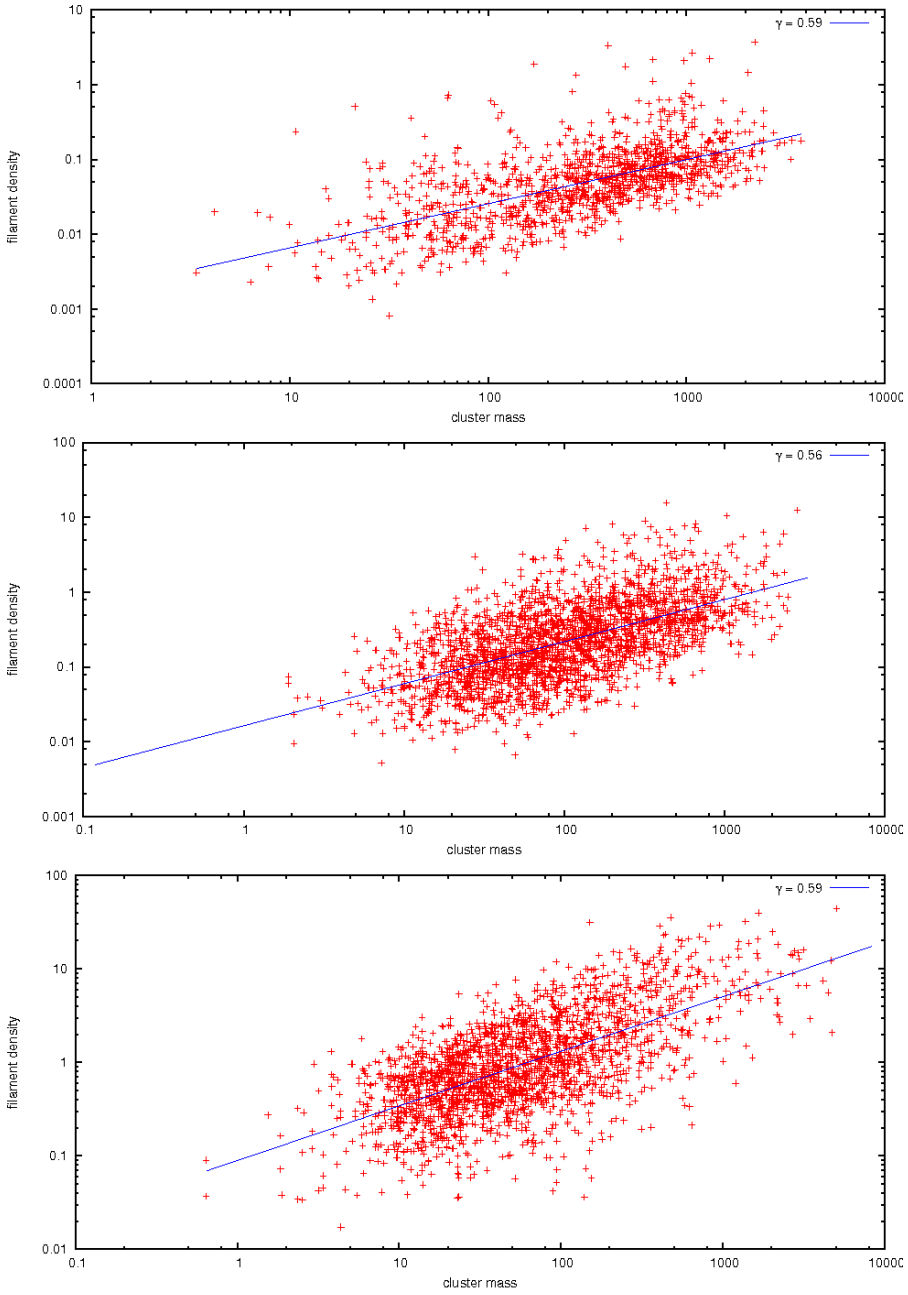

Figure 7.6: Correlation of filament density with cluster mass: We find a clear correlation between filament density and cluster mass. The slope of the power-law is similar for all three models ($n = 0.5, 0.0, -0.5$ from top to bottom). Also this slope does not change significantly with time.

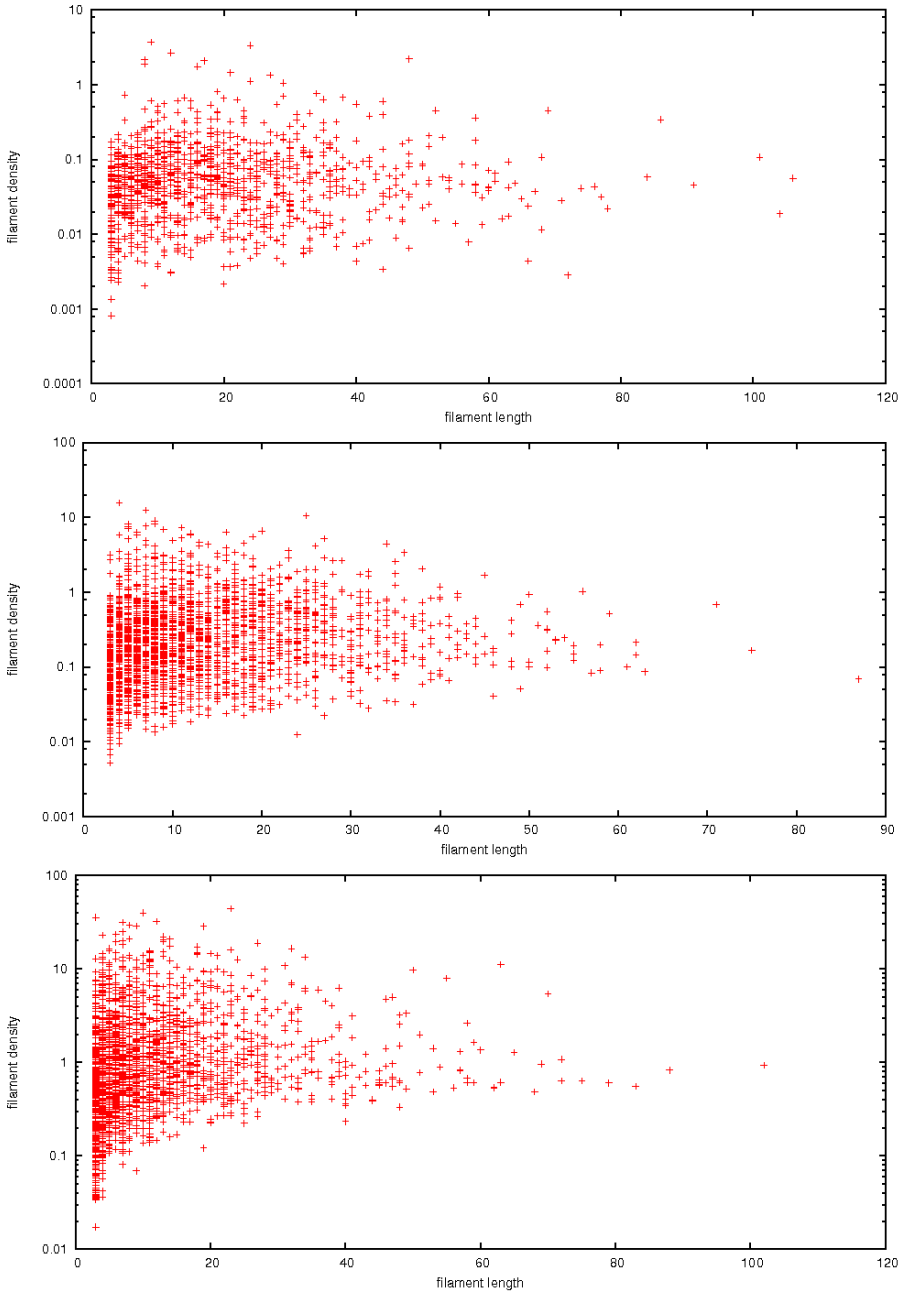

Figure 7.7: Non-correlation of filament density with filament length: We find no correlation between filament length and density what so ever ($n = 0.5, 0.0, -0.5$ from top to bottom). We do see the increase in filament density towards negative n, this can be seen also in density maps in figure (7.4)

7.3.2 Quadrilateral deformation

From the quadrilaterals that we obtain from the Eulerian map, density is not the only parameter that we can retrieve. We saw that the quadrilaterals evolve towards triangles in the case of clusters, and to elongated bars in the case of filaments, while remaining mostly square in the case of voids. To segregate these shapes we look for a set of discriminating scalar shape parameters. We investigated two such parameters.

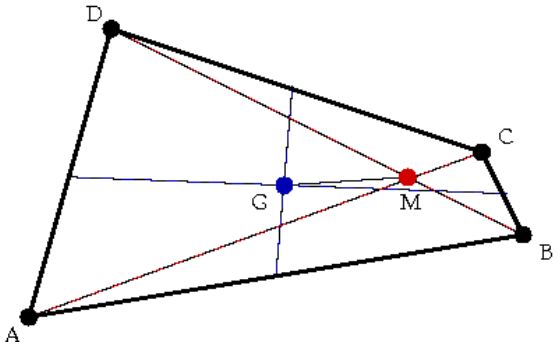

Figure 7.8: Quadrilateral deformation:In this quadrilateral we show the geometric centre G, which can be found using the average of the four corner points; and the intersection of the two diagonals M. The distance between these two points can be used as a parameter for deformation.

The most obvious candidate as a measure of *elongation* is the fraction between circumference and the square root of the surface of the quadrilateral ϵ. To measure the *deformation* we find the difference between the geometric centre and the intersection of the two diagonals of the quadrilateral Δ. This quantity too has to be divided by the square root of density to make it dimensionless.

We applied these measures to the three different scale-free models presented earlier this chapter. The results are presented in figures (7.9), (7.10) and (7.11). The three colours correspond to the independent detection of the morphological elements using the adhesion tessellation. The voids are red, filaments blue and clusters green. We see that the parameters work as expected. Especially in the model with positive n, the three morphologies are clearly separated using any combination of two of the parameters. There is some pollution in the filamentary structures from the voids. This originates from the filaments that escape detection in the tessellation because they do not form the borders between two distinct voids. In the same way there is pollution in the clusters from the filaments. The best combination of statistics seems to be the density with the elongation. Each morphological element is neatly put in one of three corners of a triangle on this plane.

In the model with $n = 0.5$ we can see two dimensional substructures with the voids and linear "smears" with the filaments. This suggests that the shape parameters are spatially correlated. This effect disappears in the model with negative power slope. This can be explained, as in the first model small scale perturbations dominate, the tidal distortions are dominated by the local environment (each void to its own). In the latter there is much more cross-talk from the larger scales down. This erases any spatial coherence there might be in the shape parameters.
In the $n = -0.5$ model the distinction between voids, filaments and clusters are getting less pronounced. This implies it will be harder to track the more fine-grained structures in these models.
The shape parameters promise to be a good way to track the finer structures in the Eulerian map directly. Also this method could be applicable to a broader family of Lagrangian codes.

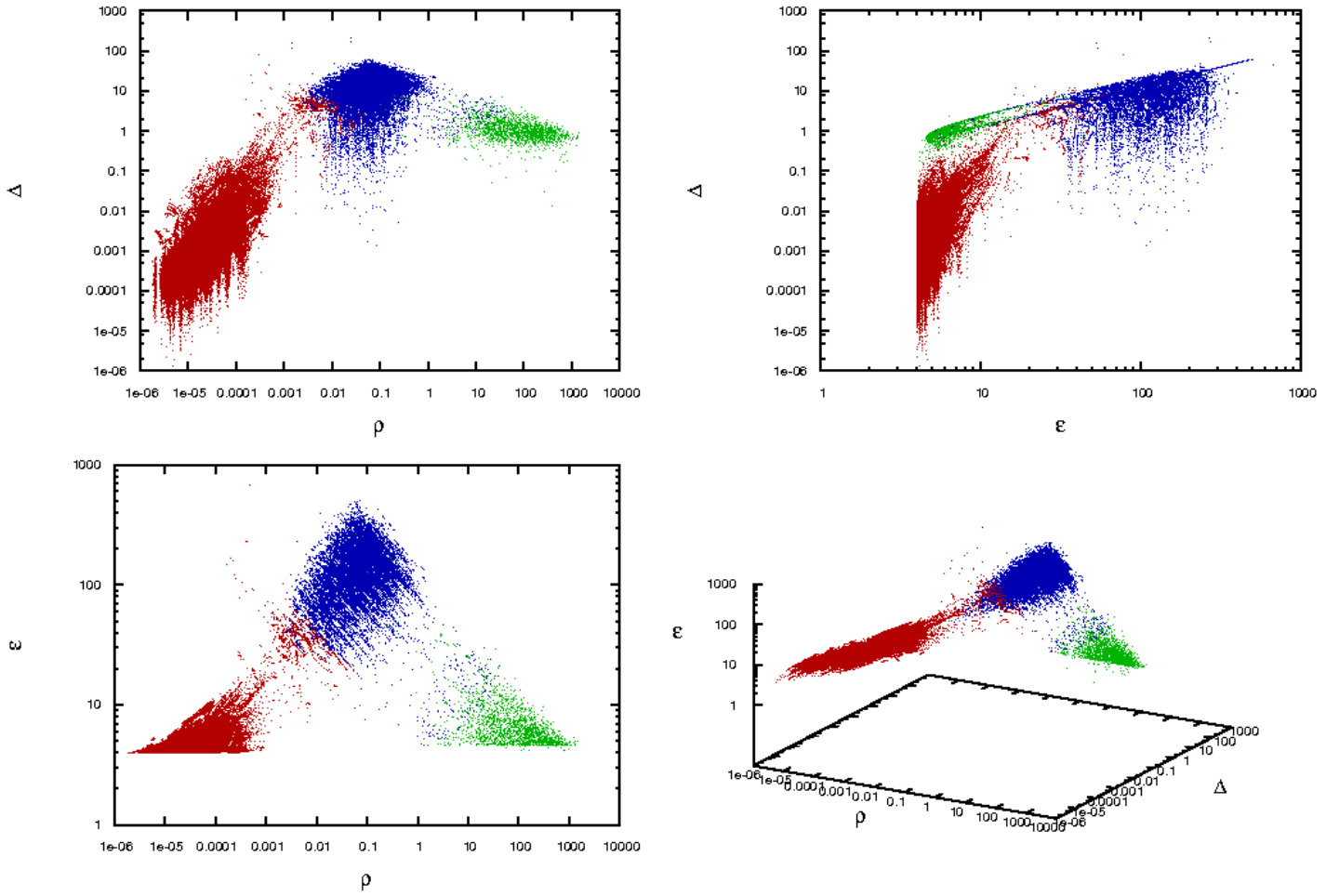

Figure 7.9: Quadrilateral deformation for $n = 0.5$: For explanation, see text.

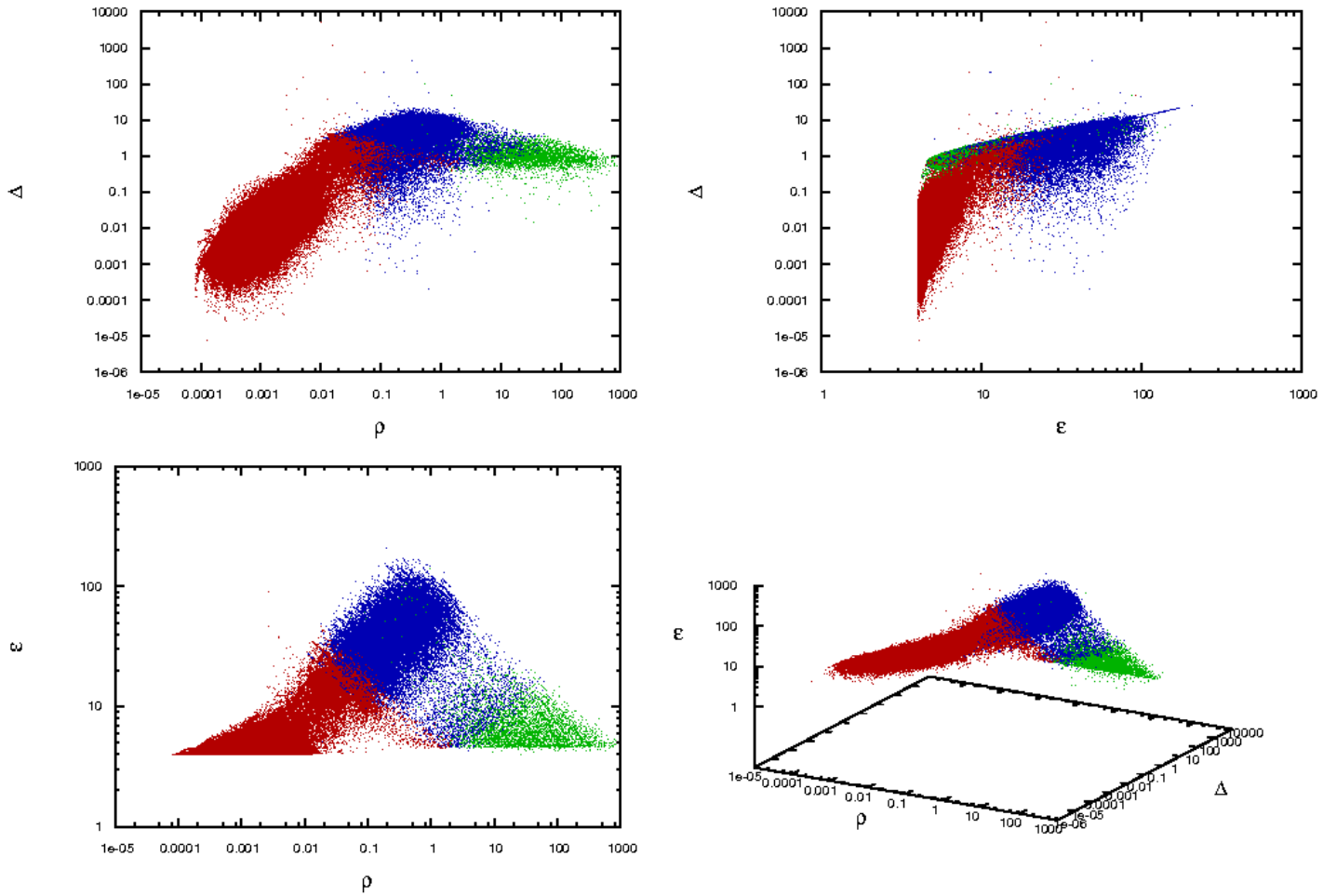

Figure 7.10: Quadrilateral deformation for $n = 0.0$: For explanation, see text.

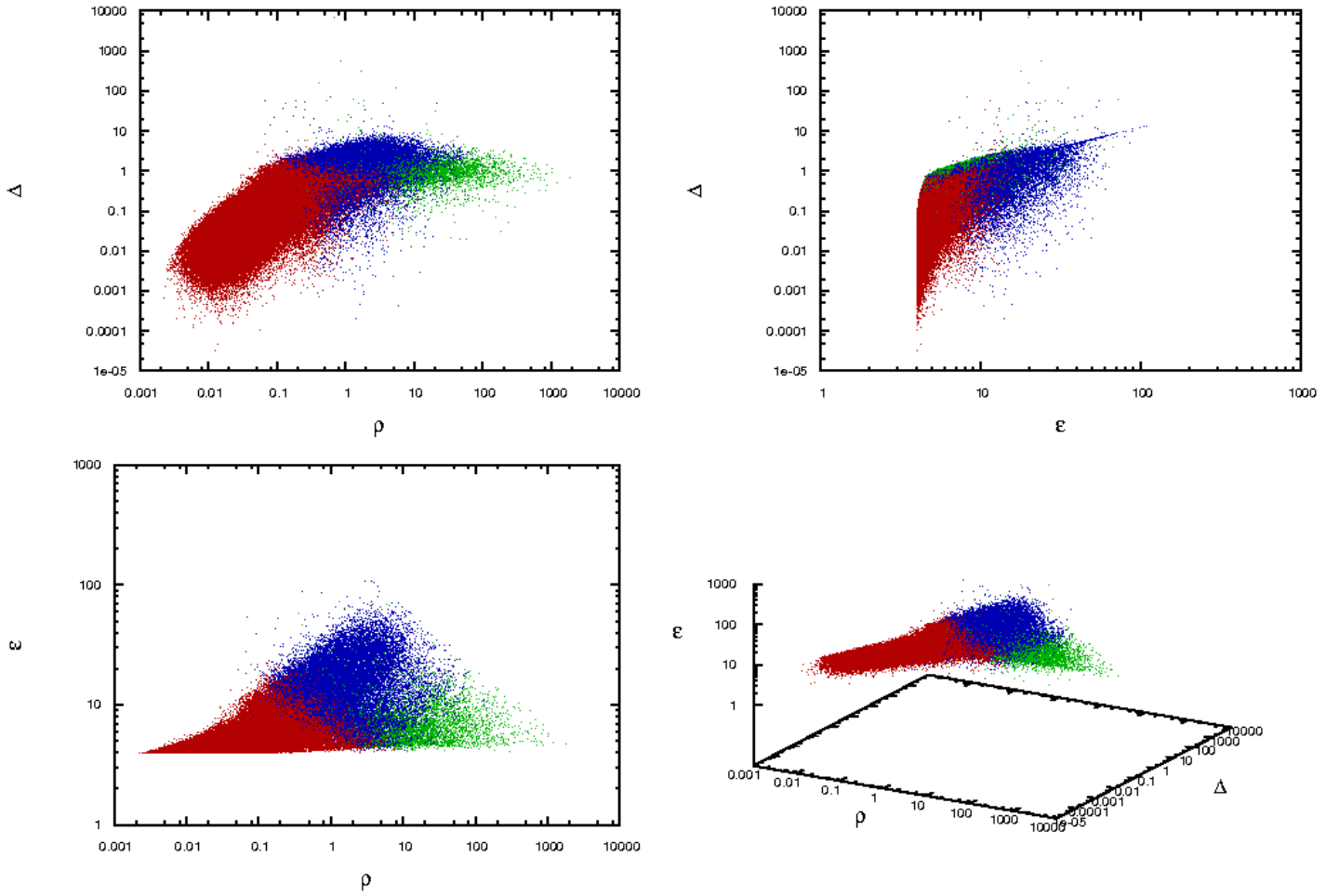

Figure 7.11: Quadrilateral deformation for $n = -0.5$: For explanation, see text.

7.3.3 Tidal fields

The tidal field gives a measure of shear distortion induced by the gravitational field. It is the symmetric traceless part of Hessian matrix of the potential.

$$T_{ij} = \frac{\partial^2 \phi}{\partial x_i \partial x_j} - \frac{1}{3}\delta^D_{ij} \boldsymbol{\nabla}^2 \phi \tag{7.2}$$

Using the eigenvectors and values of the tidal field, we can map the strength and direction of this field and correlate it with the local density. The tidal field is a central quantity in the theory of the Cosmic Web. (Bond et al., 1996; van de Weygaert and Bond, 2005a) It is generally known that the tides are correlated with the density peaks. Outside the peaks the tidal strength should be the greatest in the filaments. Adhesion allows us to check this by segregating the density correlation by morphology. Indeed we see tidal bridges between the clusters, where the filaments are. This effect is enhanced by the fact that filaments are over-densities themselves. For the different 2-D scale-free models under discussion, we plotted the magnitude of the tidal field in figure (7.12).

In figures (7.13), (7.14) and (7.15), the tidal field is plotted over the density. The field has been smooth with a radius of 8 pixels. The length of the bars is the strength of the field, the direction the compressional component. The strongest points have been left out to keep the images tidy. Again it is clear that most of the tidal influence originates in the clusters. We were unable to reproduce the results from Platen et al. (2008), as the filaments seem to be too weak, at least in this 2-D model.
The correlation between tidal field strength and density is plotted in figure (7.16) for the different scale-free models. We can distinguish the different behaviours of the tidal strength for the morphological components. There is no correlation in the voids; where they have stronger tidal fields, it is because the proximity of a cluster. We can see the tidal field getting stronger inside denser filaments, and a very tight correlation with the mass of the clusters.

Although this application of adhesion seems more or less trivial, it shows us the power of having an independent classification of the morphology of the cosmic web. Another way to perform this analysis would be to take an N-body simulation and find the elements using structure finding algorithms. However a lot of these algorithms (not counting the watershed method) depend on the analysis of the Hessian of the potential (MMF for example), which we used to calculate the tidal field.

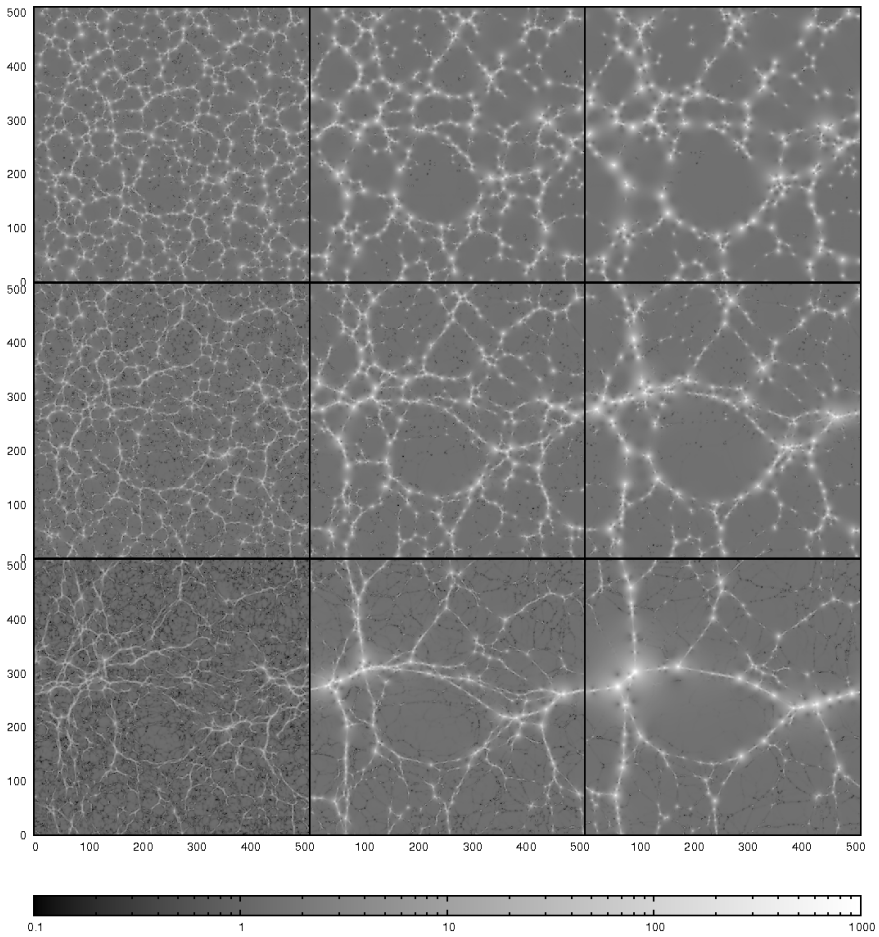

Figure 7.12: Tidal field strength: this figure shows the tidal field strength (colour-coded logarithmically) for the same nine 2-D snapshots as in figure (7.4) (from top to bottom: $n = 0.5, 0, -0.5$). We clearly see the difference in terms of dominating clusters in the top row and stronger filaments at the bottom. Also visible is the quadrupole character of the field. The tidal influence of the clusters is the greatest directly in between them, showing tidal bridges in the filaments.

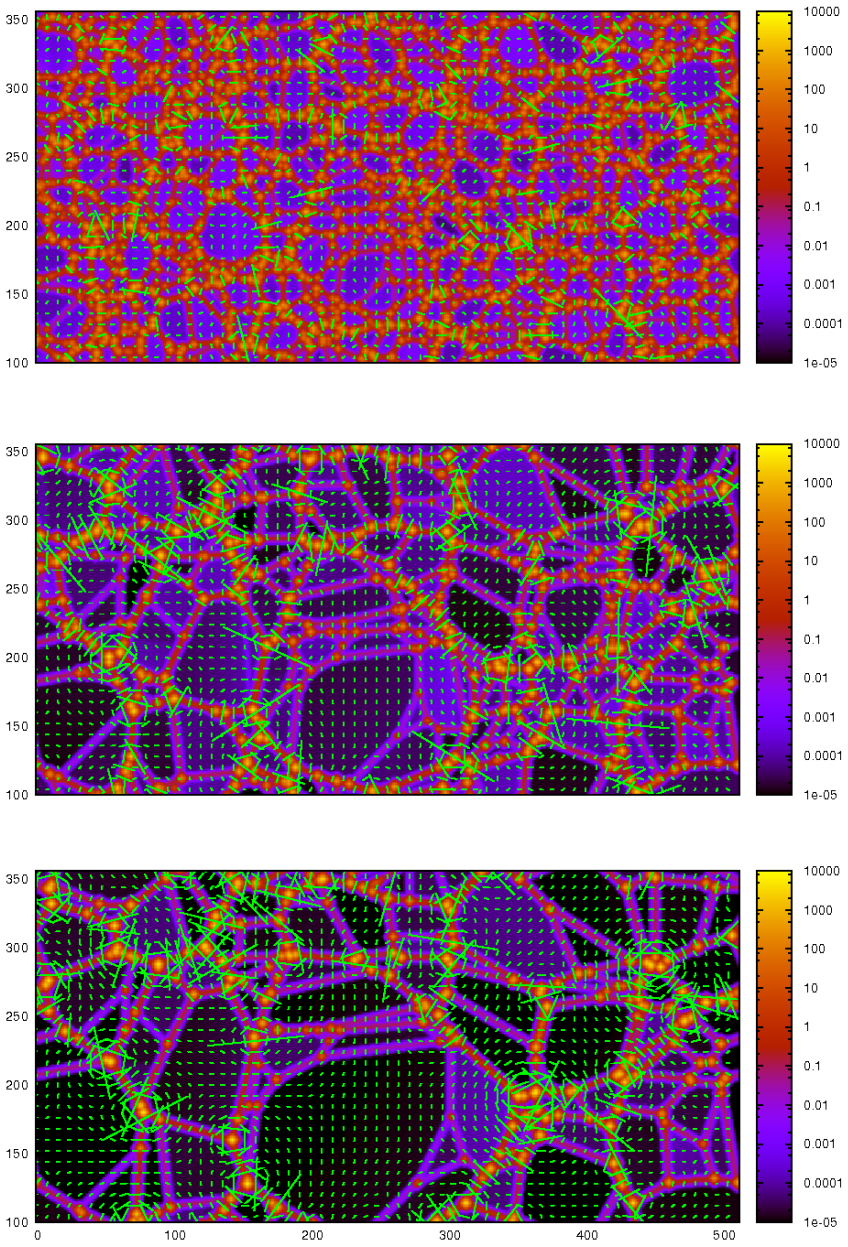

Figure 7.13: Tidal field for $n = 0.5$.

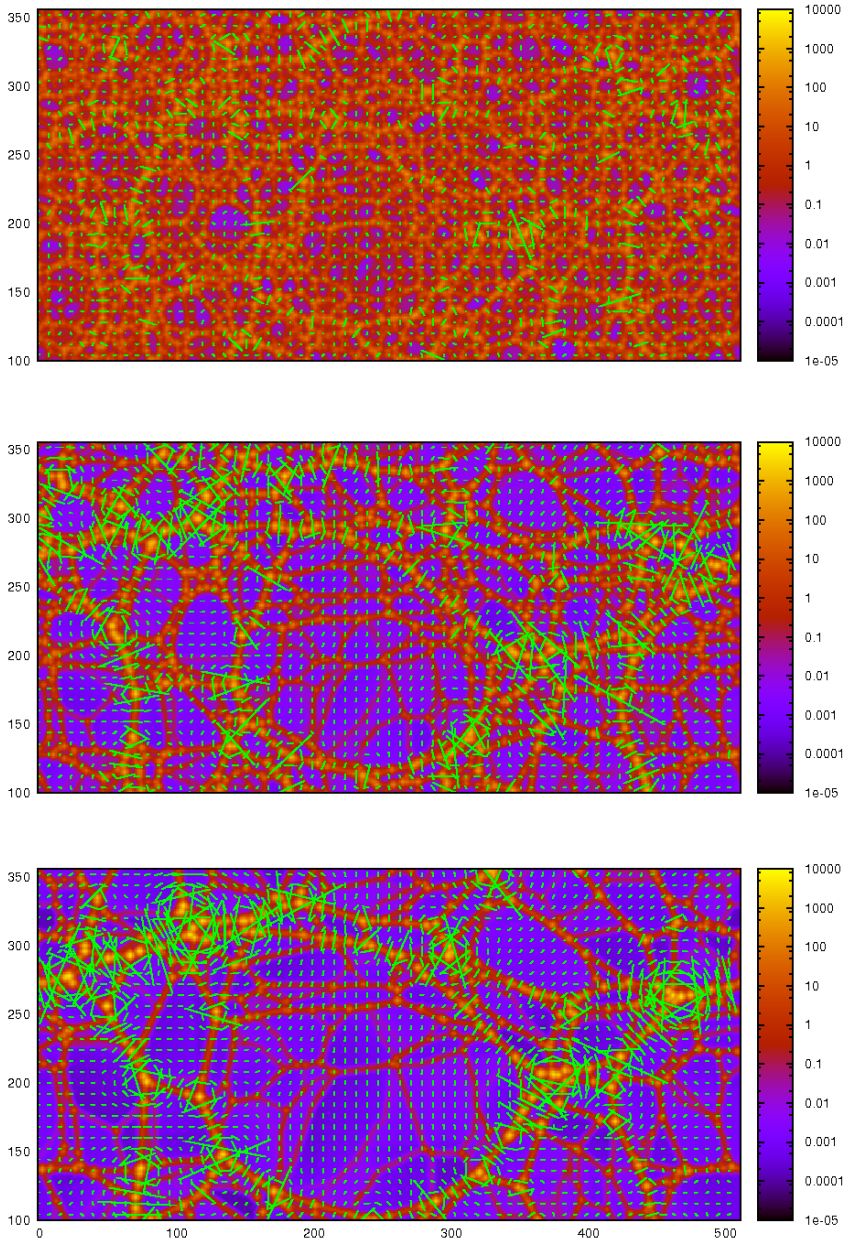

Figure 7.14: Tidal field for $n = 0.0$.

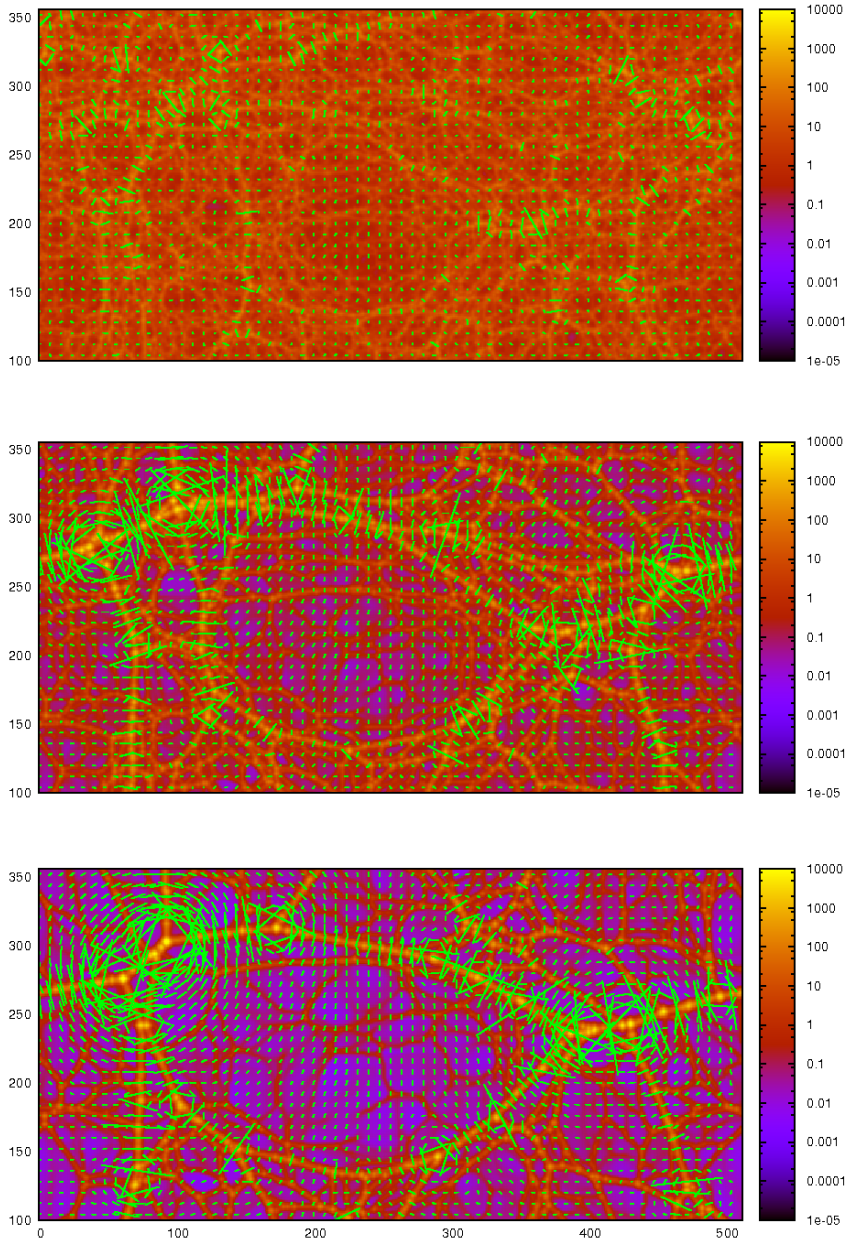

Figure 7.15: Tidal field for $n = -0.5$.

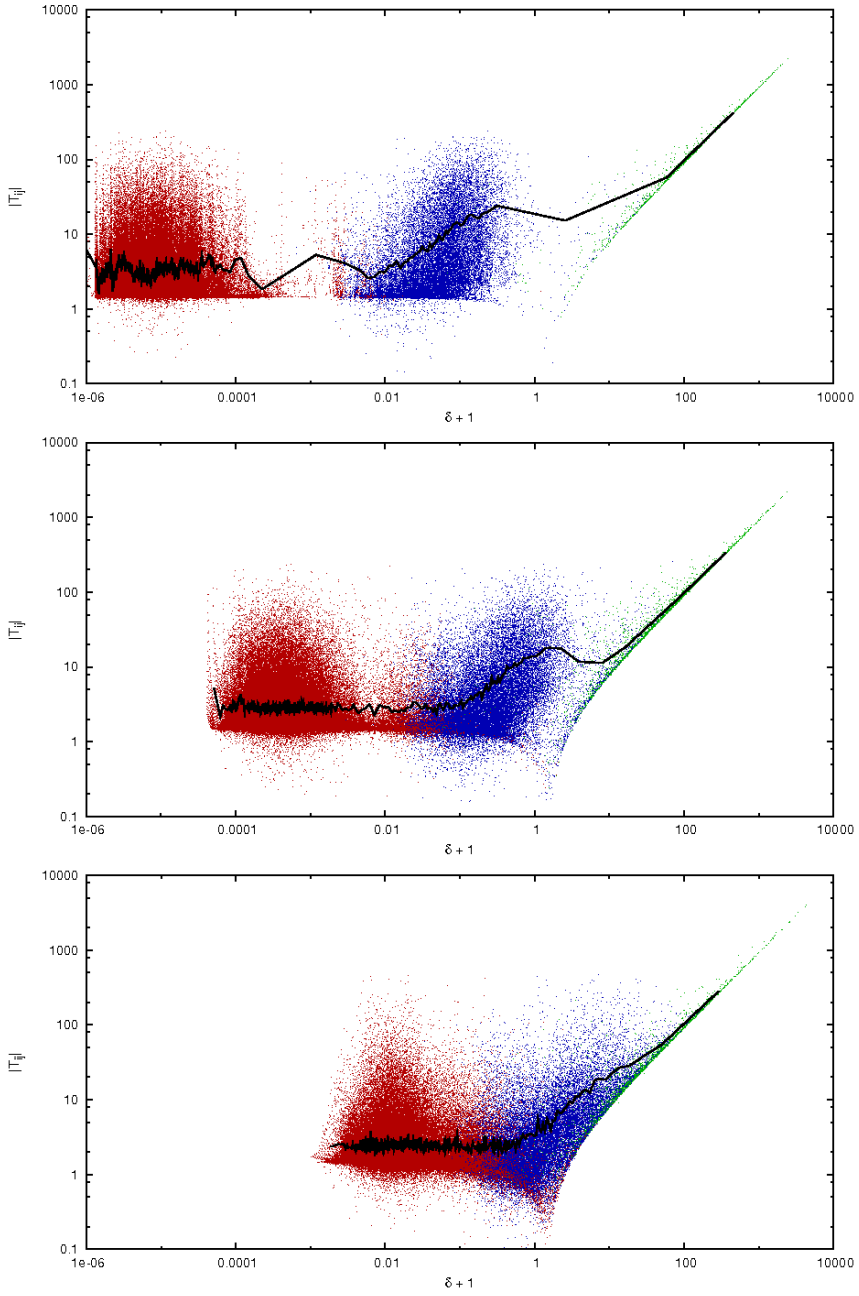

Figure 7.16: Correlation between tidal strength and density: the black line shows the average over each 512 points. The three models show similar behaviour in the correlation. There is a very tight linear correlation in the clusters and no correlation in the voids. The filaments show stronger tidal strength than clusters for the same density.

Chapter 8

Discussion

We have seen several separate examples, where adhesion theory can teach us how the cosmic web evolves. Also there were some cases where adhesion did not behave as expected. It should be clear that adhesion has severe limitations. We will put these loose examples together, and find some areas where future research is useful.

8.1 Large scale evolution of the cosmic web

Adhesion allows us to define a new language for discussing the evolution of the cosmic web. This language is enhanced by the formalism of the complementary Lagrangian and Eulerian view points. We can separate the evolution into internal and external.

Internal Describes the motion of individual particles within a structure. Any sort of fragmentation or dilution is considered to be internal. For example, two voids can only merge when a wall dissolves; which means that matter within the wall has to stream out of the wall.

External Describes the motion of an entire identifiable structure. For example, a void getting crushed between walls.

External processes are described in the $\mathcal{EL}$-dual formalism. With internal processes this is harder. Once formed, structures are impossible to delete using just internal processes. However in principle, walls and filaments can get infinitely stretched. At some point along the way we have to give up the notion that there is a wall, because it would never be detected in a real situation. Also, from the geometric Lagrangian point of view, walls can only dissolve if the neighbouring voids are nearly completely empty. This means processes

like void merger (Sheth & van de Weijgaert 2004 **??**) will not be seen in the adhesion formalism. It would be an interesting exercise to see which of the two processes (external or internal) dominate at any time. An overdose of the one makes the other insignificant.

Adhesion can only give an accurate model for the formation of large scale structure if the gravitational relaxation time-scale is short compared to the Hubble time. We could also turn this argument around and say that if adhesion gives the right answers on external structure, relaxation time-scales must be short, which might constrain properties of the internal structure.

8.2 Validity of adhesion

We should stretch that the dynamics in adhesion is completely dominated by the voids. The entire shape of the convex Lagrangian potential is determined by the patches that correspond to the voids. Because of this, clusters show strange behaviour. It is often mentioned in the literature that adhesion ceases to be valid inside singularities. We have seen the internal dynamics of a wall being well modelled, as well as the external dynamics of clusters being flawed in adhesion. Also the mass distribution in filaments was not as expected. We could say adhesion breaks down wherever clusters have a conflicting and dominant dynamical influence over that of the voids.

8.3 Future work

8.3.1 Caustics

There used to be two major competing schemes for the formation of galaxies. The theory of Hot Dark Matter (in the form of massive neutrinos) predicted galaxies forming from fragmenting pancakes in a top-down process. Cold Dark Matter gave the bottom-up process that we use today. To use caustics to describe large scale coherence in the framework of hierarchical galaxy formation would have been contraband in both camps (which were divided by the Iron curtain).

Recent observations have given tentative hints at the influence of large scale motions on galaxy formation; in particular correlations in star formation histories of galaxies thought to be in the same wall or filament. (Fleenor and Johnston-Hollitt, 2009; Ceccarelli et al., 2008; Zitrin and Brosch, 2008) Also predictions of spin alignment (Aragón-Calvo et al., 2007b) and their observation (Godłowski and Flin, 2010) leads us to conclude that large scale dynamics of the cosmic web can be an important driver of galaxy evolution.

Adhesion based algorithms can give us the locations and classifications of shocks in a simulation. At the same time more physically realistic high resolution simulations can give us information on the physical processes within different classes of caustics. Resolving shocks is typically a weak point in SPH codes, so this line of research might yield some unexpected results.

8.3.2 Legendre transforms

Our current implementation of the Legendre transform is not optimised for parallel processing. A parallel implementation makes fast Legendre transforms for bigger 3-D simulations feasible. Even bigger optimisations could be achieved in the sub-pixel enhancement phase of the calculation.

8.3.3 Dynamics within nodes

The work by Bogaevsky (Bogaevsky, 2004, 2002) distinguishes two kinds of nodes in the cosmic network. Stable nodes which accumulate matter, and unstable ones which act as way-points in the network. These nodes can change behaviour during the evolution of the cosmic web. It would be extremely interesting if this could be observed in simulations.

8.3.4 Forced Burgers dynamics

To include the influence of clusters, we need to include gravity. This could possibly be done by performing the solution of the Burgers equation sequentially, updating the potential after each step. More formally we would have to include a force term in Burgers equation. This is described in Bec and Khanin (2007) as well as Frisch and Bec (2001). Also these results should be compared with N-body simulations.

8.4 Conclusion

In the introduction we set out three goals. We wanted to obtain a tool that creates a test sample for morphological algorithms. The data the Legendre transform based code puts out, is extremely well suited to do this. Also we can vary the detection difficulty, in terms of hierarchy and larger spans in density contrast, by changing the initial conditions.
We have tried to reproduce some results from the theory of the Cosmic Web. This attempt was largely hampered by the fact that clusters merge badly in adhesion. Comparison with models that do include a dynamical gravitational component, can tell us which properties should be attributed to the complex interplay of tidal forces, and which can be explained by kinematics from the

initial conditions only.
The morphological segregation that adhesion offers, gives us a powerful tool to study the dynamical influence of the different components separately. We have seen an example of this in the tidal field of the evolved density.
The dual approach of Eulerian and Lagrangian views has given us a perspective on adhesion that allowed us to understand some of the complex processes that occur inside the simulations.

8.5 Acknowledgements

I would like to thank my supervisor Rien van de Weijgaert for his unrelenting support not only during this project, but also in the years before; Thanks also to my fellow students Wendy and Sandra for their helpful remarks and Hans for the lively discussions; Jarno for his plot; Patrick for his never ending source of Dark Energy; Keimpe for FLT and help on my poster; Jouke for Frysian brotherhood; Esra, thank you for writing an article with me and Erwin for helping me. During the course of this project I have had enlightening conversations with Bernard Jones, Ravi Sheth and Roman Juszkiewicz and Gert Vegter. Everyone I forgot, please forgive me. This work was funded by a parental research grant.

Bibliography

CGAL, Computational Geometry Algorithms Library. http://www.cgal.org.

K. N. Abazajian, J. K. Adelman-McCarthy, M. A. Agüeros, S. S. Allam, C. Allende Prieto, D. An, K. S. J. Anderson, S. F. Anderson, J. Annis, N. A. Bahcall, C. A. L. Bailer-Jones, J. C. Barentine, B. A. Bassett, A. C. Becker, T. C. Beers, E. F. Bell, V. Belokurov, A. A. Berlind, E. F. Berman, M. Bernardi, S. J. Bickerton, D. Bizyaev, J. P. Blakeslee, M. R. Blanton, J. J. Bochanski, W. N. Boroski, H. J. Brewington, J. Brinchmann, J. Brinkmann, R. J. Brunner, T. Budavári, L. N. Carey, S. Carliles, M. A. Carr, F. J. Castander, D. Cinabro, A. J. Connolly, I. Csabai, C. E. Cunha, P. C. Czarapata, J. R. A. Davenport, E. de Haas, B. Dilday, M. Doi, D. J. Eisenstein, M. L. Evans, N. W. Evans, X. Fan, S. D. Friedman, J. A. Frieman, M. Fukugita, B. T. Gänsicke, E. Gates, B. Gillespie, G. Gilmore, B. Gonzalez, C. F. Gonzalez, E. K. Grebel, J. E. Gunn, Z. Györy, P. B. Hall, P. Harding, F. H. Harris, M. Harvanek, S. L. Hawley, J. J. E. Hayes, T. M. Heckman, J. S. Hendry, G. S. Hennessy, R. B. Hindsley, J. Hoblitt, C. J. Hogan, D. W. Hogg, J. A. Holtzman, J. B. Hyde, S.-i. Ichikawa, T. Ichikawa, M. Im, Ž. Ivezić, S. Jester, L. Jiang, J. A. Johnson, A. M. Jorgensen, M. Jurić, S. M. Kent, R. Kessler, S. J. Kleinman, G. R. Knapp, K. Konishi, R. G. Kron, J. Krzesinski, N. Kuropatkin, H. Lampeitl, S. Lebedeva, M. G. Lee, Y. S. Lee, R. F. Leger, S. Lépine, N. Li, M. Lima, H. Lin, D. C. Long, C. P. Loomis, J. Loveday, R. H. Lupton, E. Magnier, O. Malanushenko, V. Malanushenko, R. Mandelbaum, B. Margon, J. P. Marriner, D. Martínez-Delgado, T. Matsubara, P. M. McGehee, T. A. McKay, A. Meiksin, H. L. Morrison, F. Mullally, J. A. Munn, T. Murphy, T. Nash, A. Nebot, E. H. Neilsen, H. J. Newberg, P. R. Newman, R. C. Nichol, T. Nicinski, M. Nieto-Santisteban, A. Nitta, S. Okamura, D. J. Oravetz, J. P. Ostriker, R. Owen, N. Padmanabhan, K. Pan, C. Park, G. Pauls, J. Peoples, W. J. Percival, J. R. Pier, A. C. Pope, D. Pourbaix, P. A. Price, N. Purger, T. Quinn, M. J. Raddick, P. R. Fiorentin, G. T. Richards, M. W. Richmond, A. G. Riess, H.-W. Rix, C. M. Rockosi, M. Sako, D. J. Schlegel, D. P. Schnei-

der, R.-D. Scholz, M. R. Schreiber, A. D. Schwope, U. Seljak, B. Sesar, E. Sheldon, K. Shimasaku, V. C. Sibley, A. E. Simmons, T. Sivarani, J. A. Smith, M. C. Smith, V. Smolčić, S. A. Snedden, A. Stebbins, M. Steinmetz, C. Stoughton, M. A. Strauss, M. Subba Rao, Y. Suto, A. S. Szalay, I. Szapudi, P. Szkody, M. Tanaka, M. Tegmark, L. F. A. Teodoro, A. R. Thakar, C. A. Tremonti, D. L. Tucker, A. Uomoto, D. E. Vanden Berk, J. Vandenberg, S. Vidrih, M. S. Vogeley, W. Voges, N. P. Vogt, Y. Wadadekar, S. Watters, D. H. Weinberg, A. A. West, S. D. M. White, B. C. Wilhite, A. C. Wonders, B. Yanny, D. R. Yocum, D. G. York, I. Zehavi, S. Zibetti, and D. B. Zucker. The Seventh Data Release of the Sloan Digital Sky Survey. ApJS, 182:543–558, June 2009. doi: 10.1088/0067-0049/182/2/543.

M. A. Aragón-Calvo, B. J. T. Jones, R. van de Weygaert, and J. M. van der Hulst. The multiscale morphology filter: identifying and extracting spatial patterns in the galaxy distribution. A&A, 474:315–338, October 2007a. doi: 10.1051/0004-6361:20077880.

M. A. Aragón-Calvo, R. van de Weygaert, B. J. T. Jones, and J. M. van der Hulst. Spin Alignment of Dark Matter Halos in Filaments and Walls. ApJ, 655:L5–L8, January 2007b. doi: 10.1086/511633.

M. A. Aragon-Calvo, R. van de Weygaert, P. A. Araya-Melo, E. Platen, and A. S. Szalay. Unfolding the hierarchy of voids. MNRAS, 404:L89–L93, May 2010. doi: 10.1111/j.1745-3933.2010.00841.x.

V. I. Arnold, S. F. Shandarin, and I. B. Zeldovich. The large scale structure of the universe. I - General properties One- and two-dimensional models. *Geophysical and Astrophysical Fluid Dynamics*, 20:111–130, 1982. doi: 10.1080/03091928208209001.

J. M. Bardeen, J. R. Bond, N. Kaiser, and A. S. Szalay. The statistics of peaks of Gaussian random fields. ApJ, 304:15–61, May 1986. doi: 10.1086/164143.

Bec and Khanin. Burgers turbulence. *Physics Reports*, 447:1–66, 2007.

A. V. Belikov and D. Hooper. How dark matter reionized the Universe. Phys. Rev. D, 80(3):035007–+, August 2009. doi: 10.1103/PhysRevD.80.035007.

Bernardeau and Valageas. Merging and fragmentation in the burgers dynamics. *arXiv*, astro-ph.CO:0912.3603v1, 2009.

Bogaevsky. Matter evolution in burgulence. *arXiv*, math-ph:0407073v1, 2004.

Ilya A. Bogaevsky. Perestroikas of shocks and singularities of minimum functions. *Physica D: Nonlinear Phenomena*, 173(1-2):1 – 28, 2002. ISSN 0167-2789. doi: DOI:10.1016/S0167-2789(02)00652-8. URL

http://www.sciencedirect.com/science/article/B6TVK-472J3CV-2/2/9ecd5f5b%25a42224726778082f4bfc10.

J. R. Bond, L. Kofman, and D. Pogosyan. How filaments of galaxies are woven into the cosmic web. Nature, 380:603–606, April 1996. doi: 10.1038/380603a0.

L. Ceccarelli, N. Padilla, and D. G. Lambas. Large-scale modulation of star formation in void walls. MNRAS, 390:L9–L13, October 2008. doi: 10.1111/j.1745-3933.2008.00520.x.

T. Clifton, P. G. Ferreira, and K. Land. Living in a Void: Testing the Copernican Principle with Distant Supernovae. *Physical Review Letters*, 101(13):131302–+, September 2008. doi: 10.1103/PhysRevLett.101.131302.

J. M. Colberg, K. S. Krughoff, and A. J. Connolly. Intercluster filaments in a ΛCDM Universe. MNRAS, 359:272–282, May 2005. doi: 10.1111/j.1365-2966.2005.08897.x.

Peter Coles, Adrian L. Melott, and Sergei F. Shandarin. Testing approximations for non-linear gravitational clustering. MNRAS, 260:765–776, February 1993.

W. J. G. de Blok. The Core-Cusp Problem. *Advances in Astronomy*, 2010, 2010. doi: 10.1155/2010/789293.

A. G. Doroshkevich. Spatial structure of perturbations and origin of galactic rotation in fluctuation theory. *Astrophysics*, 6:320–330, October 1970. doi: 10.1007/BF01001625.

C. C. Ebbesmayer, W. J. Ingraham, T. C. Royer, and C. E. Grosch. Tub toys orbit the pacific subarctic gyre. *EOS, transactions, American Geophysical Union*, Vol. 88, No. 1:1–12, January 2007.

H. Edelsbrunner. Alpha shapes - a survey. In Rien van de Weijgaert, Gert Vegter, Jelle Ritzerveld, and Vincent Icke, editors, *Tesselations in the Siences; Virtues, Techniques and Applications of Geometric Tilings*. Springer Verlag, 2010.

D. J. Eisenstein, I. Zehavi, D. W. Hogg, R. Scoccimarro, M. R. Blanton, R. C. Nichol, R. Scranton, H.-J. Seo, M. Tegmark, Z. Zheng, S. F. Anderson, J. Annis, N. Bahcall, J. Brinkmann, S. Burles, F. J. Castander, A. Connolly, I. Csabai, M. Doi, M. Fukugita, J. A. Frieman, K. Glazebrook, J. E. Gunn, J. S. Hendry, G. Hennessy, Z. Ivezić, S. Kent, G. R. Knapp, H. Lin, Y.-S. Loh, R. H. Lupton, B. Margon, T. A. McKay, A. Meiksin, J. A. Munn, A. Pope, M. W. Richmond, D. Schlegel, D. P. Schneider, K. Shimasaku, C. Stoughton, M. A. Strauss, M. SubbaRao, A. S. Szalay, I. Szapudi, D. L. Tucker, B. Yanny, and D. G. York. Detection of the Baryon Acoustic Peak in the Large-Scale

Correlation Function of SDSS Luminous Red Galaxies. ApJ, 633:560–574, November 2005. doi: 10.1086/466512.

M. C. Fleenor and M. Johnston-Hollitt. Megaparsec-Scale Triggers for Star Formation: Clusters and Filaments of Galaxies in the Horologium-Reticulum Supercluster. *ArXiv*, astro-ph:0909.0232v1, September 2009.

Frisch and Bec. Burgulence. *arXiv*, nlin:0012033v2, 2001.

R. Gavazzi, R. Mohayaee, and B. Fort. Probing dark matter caustics with weak lensing. A&A, 445:43–49, January 2006. doi: 10.1051/0004-6361:20053557.

Joachim Giesen. The flow comlpex: a data structure for geometric modeling. *Computational geometry*, 39:178–190, 2008.

W. Godłowski and P. Flin. The Orientations of Galaxy Groups and Formation of the Local Supercluster. ApJ, 708:920–926, January 2010. doi: 10.1088/0004-637X/708/2/920.

J. R. Gott, III, M. Dickinson, and A. L. Melott. The sponge-like topology of large-scale structure in the universe. ApJ, 306:341–357, July 1986. doi: 10.1086/164347.

J. Grandy. Efficient computation of volume of hexahedral cells, 1997.

S. N. Gurbatov and A. I. Saichev. Probability distribution and spectra of potential hydrodynamic turbulence. *Radiophysics and Quantum Electronics*, 27: 303–313, April 1984. doi: 10.1007/BF01036611.

S. N. Gurbatov, A. I. Saichev, and S. F. Shandarin. The large-scale structure of the universe in the frame of the model equation of non-linear diffusion. MNRAS, 236:385–402, January 1989.

A. H. Guth. Inflationary universe: A possible solution to the horizon and flatness problems. Phys. Rev. D, 23:347–356, January 1981. doi: 10.1103/PhysRevD.23.347.

C. J. Hogan. Particle annihilation in cold dark matter micropancakes. Phys. Rev. D, 64(6):063515–+, September 2001. doi: 10.1103/PhysRevD.64.063515.

Eberhard Hopf. The partial differential equation $u_t + uu_x = \mu_{xx}$. *Communications on Pure and Applied Mathematics*, Vol. 3, No. 3:201–230, 1950. doi: 10.1002/cpa.3160030302. URL `http://dx.doi.org/10.1002/cpa.3160030302`.

V. Icke and R. van de Weijgaert. Fragmenting the universe. A&A, 184:16–32, 1987.

A. Klypin and S. F. Shandarin. Percolation technique for galaxy clustering. ApJ, 413:48–58, August 1993. doi: 10.1086/172975.

A. Klypin, A. V. Kravtsov, O. Valenzuela, and F. Prada. Where Are the Missing Galactic Satellites? ApJ, 522:82–92, September 1999. doi: 10.1086/307643.

L. Kofman and D. Pogosyan. Dynamics of gravitational instability is nonlocal. ApJ, 442:30–38, March 1995. doi: 10.1086/175419.

L. Kofman, D. Pogosyan, and S. F. Shandarin. Structure of the universe in the two-dimensional model of adhesion. MNRAS, 242:200–208, 1990.

L. Kofman, D. Pogosyan, S. F. Shandarin, and A. L. Melott. Coherent structures in the universe and the adhesion model. ApJ, 393:437–449, July 1992. doi: 10.1086/171517.

E. Komatsu, A. Kogut, M. R. Nolta, C. L. Bennett, M. Halpern, G. Hinshaw, N. Jarosik, M. Limon, S. S. Meyer, L. Page, D. N. Spergel, G. S. Tucker, L. Verde, E. Wollack, and E. L. Wright. First-Year Wilkinson Microwave Anisotropy Probe (WMAP) Observations: Tests of Gaussianity. ApJS, 148: 119–134, September 2003. doi: 10.1086/377220.

E. Komatsu, J. Dunkley, M. R. Nolta, C. L. Bennett, B. Gold, G. Hinshaw, N. Jarosik, D. Larson, M. Limon, L. Page, D. N. Spergel, M. Halpern, R. S. Hill, A. Kogut, S. S. Meyer, G. S. Tucker, J. L. Weiland, E. Wollack, and E. L. Wright. Five-Year Wilkinson Microwave Anisotropy Probe Observations: Cosmological Interpretation. ApJS, 180:330–376, February 2009. doi: 10.1088/0067-0049/180/2/330.

A. D. Linde. A new inflationary universe scenario: A possible solution of the horizon, flatness, homogeneity, isotropy and primordial monopole problems. *Physics Letters B*, 108:389–393, February 1982. doi: 10.1016/0370-2693(82)91219-9.

T. Lindeberg. Scale-space for discrete signals. *IEEE Transactions of Pattern Analysis and Machine Intelligence*, Vol. 12, No. 3:234–254, 1990.

A. L. Melott, S. F. Shandarin, and D. H. Weinberg. A test of the adhesion approximation for gravitational clustering. ApJ, 428:28–34, June 1994. doi: 10.1086/174216.

J. F. Navarro, C. S. Frenk, and S. D. M. White. The Structure of Cold Dark Matter Halos. ApJ, 462:563–+, May 1996. doi: 10.1086/177173.

A. Noullez and M. Vergassola. A fast legendre transform algorithm and applications to the adhesion model. *Journal of Scientific Computing*, Vol 9. No. 3:259–281, 1994.

P. J. E. Peebles. The Void Phenomenon. ApJ, 557:495–504, August 2001. doi: 10.1086/322254.

P. J. E. Peebles. *Large-Scale Structure of the Universe*. Princeton University Press, 1980.

L. Perivolaropoulos. Six Puzzles for LCDM Cosmology. *ArXiv e-prints*, November 2008.

S. Perlmutter, G. Aldering, G. Goldhaber, R. A. Knop, P. Nugent, P. G. Castro, S. Deustua, S. Fabbro, A. Goobar, D. E. Groom, I. M. Hook, A. G. Kim, M. Y. Kim, J. C. Lee, N. J. Nunes, R. Pain, C. R. Pennypacker, R. Quimby, C. Lidman, R. S. Ellis, M. Irwin, R. G. McMahon, P. Ruiz-Lapuente, N. Walton, B. Schaefer, B. J. Boyle, A. V. Filippenko, T. Matheson, A. S. Fruchter, N. Panagia, H. J. M. Newberg, W. J. Couch, and The Supernova Cosmology Project. Measurements of Omega and Lambda from 42 High-Redshift Supernovae. ApJ, 517:565–586, June 1999. doi: 10.1086/307221.

E. Platen, R. van de Weygaert, and B. J. T. Jones. A cosmic watershed: the WVF void detection technique. MNRAS, 380:551–570, September 2007. doi: 10.1111/j.1365-2966.2007.12125.x.

E. Platen, R. van de Weygaert, and B. J. T. Jones. Alignment of voids in the cosmic web. MNRAS, 387:128–136, June 2008. doi: 10.1111/j.1365-2966.2008.13019.x.

A. G. Riess, A. V. Filippenko, P. Challis, A. Clocchiatti, A. Diercks, P. M. Garnavich, R. L. Gilliland, C. J. Hogan, S. Jha, R. P. Kirshner, B. Leibundgut, M. M. Phillips, D. Reiss, B. P. Schmidt, R. A. Schommer, R. C. Smith, J. Spyromilio, C. Stubbs, N. B. Suntzeff, and J. Tonry. Observational Evidence from Supernovae for an Accelerating Universe and a Cosmological Constant. AJ, 116:1009–1038, September 1998. doi: 10.1086/300499.

V. Sahni and P. Coles. Approximation methods for non-linear gravitational clustering. Phys. Rep., 262:1–135, November 1995. doi: 10.1016/0370-1573(95)00014-8.

V. Sahni, B. S. Sathyaprakash, and S. F. Shandarin. The evolution of voids in the adhesion approximation. ApJ, 431:20–40, August 1994. doi: 10.1086/174464.

D. N. Schramm and M. S. Turner. Big-bang nucleosynthesis enters the precision era. *Reviews of Modern Physics*, 70:303–318, January 1998. doi: 10.1103/RevModPhys.70.303.

S. Shandarin. Theory of Adhesion for Large-Scale Structure. In D. W. Latham & L. A. N. da Costa, editor, *Large-scale Structures and Peculiar Motions in*

the Universe, volume 15 of *Astronomical Society of the Pacific Conference Series*, pages 189–+, 1991.

S. F. Shandarin. Percolation Theory and the Cell Lattice Structure of the Universe. *Soviet Astronomy Letters*, 9:104–+, February 1983.

S. F. Shandarin. Theories of Large Scale Structure. In J. Audouze, M.-C. Pelletan, & S. Szalay, editor, *Large Scale Structures of the Universe*, volume 130 of *IAU Symposium*, pages 273–+, 1988.

S. F. Shandarin. Three-dimensional Burgers' Equation as a Model for the Large-Scale Structure Formation in the Universe. *ArXiv Astrophysics e-prints*, July 1995.

S. F. Shandarin and Y. B. Zeldovich. The large-scale structure of the universe: Turbulence, intermittency, structures in a self-gravitating medium. *Reviews of Modern Physics*, 61:185–220, April 1989. doi: 10.1103/RevModPhys.61.185.

R. K. Sheth and R. van de Weygaert. A hierarchy of voids: much ado about nothing. MNRAS, 350:517–538, May 2004. doi: 10.1111/j.1365-2966.2004.07661.x.

T. Sousbie, S. Colombi, and C. Pichon. The fully connected N-dimensional skeleton: probing the evolution of the cosmic web. MNRAS, 393:457–477, February 2009. doi: 10.1111/j.1365-2966.2008.14244.x.

R. van de Weygaert and J. R. Bond. Clusters and the theory of the cosmic web. *Lectures at Summerschool Guillermo Haro*, 1:–, 2005a. URL `http://www.astro.rug.nl/~weygaert/tim1publication/weybondgh2005.paper1.%pdf`.

R. van de Weygaert and J. R. Bond. Observations and morphology of the cosmic web. *Lectures at Summerschool Guillermo Haro*, 2:–, 2005b. URL `http://www.astro.rug.nl/~weygaert/tim1publication/weybondgh2005.paper2.%pdf`.

M. Vergassola, B. Dubrulle, U. Frisch, and A. Noullez. Burgers' equation, Devil's staircases and the mass distribution for large-scale structures. A&A, 289:325–356, September 1994.

D. H. Weinberg and J. E. Gunn. Largescale Structure and the Adhesion Approximation. MNRAS, 247:260–+, November 1990.

Y. B. Zel'Dovich. Gravitational instability: An approximate theory for large density perturbations. A&A, 5:84–89, March 1970.

A. Zitrin and N. Brosch. The NGC 672 and 784 galaxy groups: evidence for galaxy formation and growth along a nearby dark matter filament. MNRAS, 390:408–420, October 2008. doi: 10.1111/j.1365-2966.2008.13786.x.

Appendix A

Conventions

In the literature there are a lot of different conventions on the naming of variables; especially when dealing with the amount of different coordinate systems and potentials, this can be quite confusing. In this appendix we hope to clarify our own choices.

$\boldsymbol{r}$ Physical coordinate

$\boldsymbol{x}$ Comoving coordinate

$\boldsymbol{q}$ Comoving Lagrangian coordinate

t Time

a Hubble expansion factor

D_+ Growing mode solution

$\boldsymbol{u}$ In section 2 this is the physical velocity $\partial_t \boldsymbol{r}$, in section 3 & 4 the comoving velocity with respect to the growth factor $\partial_D \boldsymbol{x}$.

$\boldsymbol{v}$ Comoving velocity $a\partial_t \boldsymbol{x}$.

ρ Density

δ Density perturbation

Φ Gravitational potential, later on the linear velocity potential

ϕ Gravitational potential perturbation

$\boldsymbol{u}_0$ Zel'dovich displacement field

Φ_0 Zel'dovich displacement potential $\boldsymbol{u}_0 = -\boldsymbol{\nabla}_q \Phi_0(\boldsymbol{q})$

d_{ij} Zel'dovich deformation tensor

Appendix B

Newtonian Friedman equations and the Einstein-de Sitter universe

A lot of cosmology text books start with an introduction into general relativity, while in fact Newton's laws are all we need if we don't bother about pressure terms or the cosmological constant. We start with the Poisson equation, assuming spherical symmetry, $\ddot{x} = \dot{x} = 0$ and $\rho \propto a^{-3}$.

$$\nabla^2 \Phi_u = \frac{1}{r^2}\left(\frac{\partial}{\partial r}\left(r^2 \frac{\partial}{\partial r}\right)\Phi_u\right) = 4\pi G\rho$$

$$\Phi_u = \frac{2\pi G}{3}\rho r^2$$

$$\ddot{\boldsymbol{r}} = \ddot{a}\boldsymbol{x} = -\frac{\boldsymbol{\nabla}_x}{a}\Phi_u$$

$$\boxed{\frac{\ddot{a}}{a} = -\frac{4\pi G}{3}\rho} \tag{B.1}$$

which is the acceleration equation.

Continuity equation in the case of matter

$$3\rho\dot{a} = -\dot{\rho}a$$

$$2\ddot{a}\dot{a} = -\frac{8\pi G}{3}\rho a\dot{a}$$

then using partial integration

$$\int \rho a\dot{a}\ dt = a^2\rho - \int a(\dot{\rho}a + \rho\dot{a})\ dt = a^2\rho + 2\int \rho a\dot{a}\ dt$$

$$\int \rho a\dot{a}\ dt = -a^2\rho + C$$

then

$$\boxed{\left(\frac{\dot{a}}{a}\right)^2 = \frac{8\pi G}{3}\left(\rho + \frac{C}{a^2}\right)} \tag{B.2}$$

The Einstein-de Sitter model has the integration constant $C = 0$. If we make the ansatz $a = (t/t_0)^n$ and have $\rho = \rho_0 a^{-3}$ then

$$\left(\frac{\dot{a}}{a}\right)^2 = \frac{8\pi G}{3}\rho_0 a^{-3}$$

$$\dot{a}^2 a = \text{Const.}, \quad n = \frac{2}{3}$$

$$a = \left(\frac{t}{t_0}\right)^{\frac{2}{3}}$$

At $t = t_0$, $a = 1$ and $H \equiv \dot{a}/a$ that is

$$t_0 = \frac{2}{3}H_0^{-1}$$

Also we can now calculate the density in such a Universe

$$\rho_0 = \frac{3H_0^2}{8\pi G}$$

and we see that this Universe can only be the case if $\rho = \rho_{\text{crit}}$.

Appendix C

Comoving equations of motion

C.1 Euler equation

The Euler equation is the embodiment of Newtons law of inertia in a fluid. We will neglect pressure terms from now on since we're dealing with scenarios that are "dark matter only".
If we put together equations 2.9 and 2.10 we obtain the comoving version

$$\frac{d(a\boldsymbol{v})}{dt} = -\boldsymbol{\nabla}_{\boldsymbol{x}}\phi \tag{C.1}$$

Writing this out in full

$$\frac{\partial(a\boldsymbol{v})}{\partial t} + \frac{1}{a}\boldsymbol{v}\cdot\boldsymbol{\nabla}_x(a\boldsymbol{v}) = -\boldsymbol{\nabla}_x\phi \tag{C.2}$$

then using $d(a\boldsymbol{v})/dt = \dot{a}\boldsymbol{v} + a\frac{\partial \boldsymbol{v}}{\partial t}$

$$\frac{\partial \boldsymbol{v}}{\partial t} + \frac{\dot{a}}{a}\boldsymbol{v} + \frac{1}{a}\boldsymbol{v}\cdot\boldsymbol{\nabla}_x(\boldsymbol{v}) = -\frac{\boldsymbol{\nabla}_x}{a}\phi \tag{C.3}$$

The term $H\boldsymbol{v}$ is the most important change with respect to the version in physical coordinates, which is known as the *Hubble drag*.

C.2 Continuity equation

Continuity takes care of the conservation of mass: the change of density is equal to the rate of inflow.

$$\dot{\rho} + \boldsymbol{\nabla}_r \cdot \rho\boldsymbol{u} = 0$$

$$\dot{\delta} + \frac{\boldsymbol{\nabla}_x}{a}(\delta+1)\boldsymbol{v} + (\frac{\dot{\bar{\rho}}}{\bar{\rho}} + 3\frac{\dot{a}}{a})(\delta+1) = 0$$

using that $\rho \propto a^{-3}$ (assuming matter only) we see that

$$\frac{\dot{\bar{\rho}}}{\bar{\rho}} = -3\frac{\dot{a}}{a}$$

and we lose the last term

$$\dot{\delta} + \frac{\boldsymbol{\nabla}_x}{a}(\delta + 1)\boldsymbol{v} = 0 \tag{C.4}$$

C.3 Poisson equation

The last equation adds gravity to our system

$$\nabla_r^2 \Phi = 4\pi G\rho$$

$$\nabla_r^2(\phi + \Phi_u) = 4\pi G(\delta\bar{\rho} + \bar{\rho})$$

This we then separate into two equations (the assumption that we can do this was discussed earlier)

$$\nabla_r^2 \Phi_u = -\frac{\nabla_x^2}{a^2}\frac{1}{2}a\ddot{a}x^2 = -3\frac{\ddot{a}}{a} = 4\pi G\bar{\rho}$$

and

$$\nabla_r^2 \phi = \frac{\nabla_x^2}{a^2}\phi = 4\pi G\delta\bar{\rho}$$

The first equation is the Newtonian variant (differing by the pressure terms) of the Friedman equation. The second is the one we're interested in

$$\nabla_x^2 \phi = 4\pi G a^2 \bar{\rho}\delta \tag{C.5}$$

A full treatment of these equations can be found in Peebles (1980) (Peebles, 1980).

Appendix D

Cubic splines

To do the interpolation we need a cubic spline since the derivatives should vary smoothly for the minimization to work.

$$\sum_{i,j,\cdots=0}^{3} a_{ij\ldots} x^i y^j \ldots$$

Cubic interpolation has the benefit that it works in k-dimensions; the number of free parameters $p = 4^k$ which we can fit to the values at 2^k points at 2^k different configurations of derivatives (i.e. f, f_x, f_y, f_{xy} for $k = 2$). This always gives an isotropic interpolation. The values of $a_{ij\ldots}$ are then calculated by solving a matrix equation (with a nice integer valued inverse) which is worked out in the appendix. To do the actual minimization we use a multi-dimensional Broyden-Fletcher-Goldfarb-Shanno routine from the GNU Scientific Library. This is then initialized with the location found in the FLT. The cubic spline has the benefit of having a unique isotropic interpolation scheme for any dimension. The function we have to fit is

$$\sum_{i,j,\cdots=0}^{3} a_{ij\ldots} x^i y^j \ldots$$

In d-dimensions this gives us $N = 4^d$ free paramaters. These have to be fit to every combination 2^d of derivatives on 2^d corner points. We will work out the example for $d = 2$.

$$f(x, y) = \sum_{i,j}^{3} a_{ij} x^i y^j$$

Corners of the interpolation cube will be denoted by combinations of 0 and 1.

$$f(0, 0) = a_{00}$$

$$f(0,1) = \sum_{j=0}^{3} a_{0j}$$

$$f(1,0) = \sum_{i=0}^{3} a_{i0}$$

$$f(1,1) = \sum_{i=0}^{3}\sum_{j=0}^{3} a_{ij}$$

$$\frac{d}{dx}f(0,0) = a_{10}$$

$$\frac{d}{dx}f(0,1) = \sum_{j=0}^{3} a_{1j}$$

$$\frac{d}{dx}f(1,0) = \sum_{i=1}^{3} ia_{i0}$$

$$\frac{d}{dx}f(1,1) = \sum_{i=1}^{3}\sum_{j=0}^{3} ia_{ij}$$

$$\frac{d}{dy}f(0,0) = a_{01}$$

$$\frac{d}{dy}f(0,1) = \sum_{j=1}^{3} ja_{0j}$$

$$\frac{d}{dy}f(1,0) = \sum_{i=0}^{3} a_{i1}$$

$$\frac{d}{dy}f(1,1) = \sum_{i=0}^{3}\sum_{j=1}^{3} ja_{ij}$$

$$\frac{d}{dx}\frac{d}{dy}f(0,0) = a_{11}$$

$$\frac{d}{dx}\frac{d}{dy}f(0,1) = \sum_{j=1}^{3} ja_{1j}$$

$$\frac{d}{dx}\frac{d}{dy}f(1,0) = \sum_{i=1}^{3} ia_{i1}$$

$$\frac{d}{dx}\frac{d}{dy}f(1,1) = \sum_{i=1}^{3}\sum_{j=1}^{3} ija_{ij}$$

This can be expressed in the matrix equation $x = [f(0,0),\ f(0,1),\ f(1,0),\ f(1,1), f_x(0,0), f_x(0,1), f_x(1,0), f_x(1,1), f_y(0,0), f_y(0,1), f_y(1,0), f_y(1,1), f_xy(0,0),$

$f_x y(0,1)$, $f_x y(1,0)$, $f_x y(1,1)]^T$ and $\alpha = [a_{00}, a_{10}, a_{20}, a_{30}, a_{01}, a_{11}, a_{21}, a_{31}, a_{02}, a_{12}, a_{22}, a_{32}, a_{03}, a_{13}, a_{23}, a_{33}]^T$

$$A\alpha = x$$

with

$$A = \begin{pmatrix}
1&0&0&0&0&0&0&0&0&0&0&0&0&0&0&0\\
1&1&1&1&0&0&0&0&0&0&0&0&0&0&0&0\\
1&0&0&0&1&0&0&0&1&0&0&0&1&0&0&0\\
1&1&1&1&1&1&1&1&1&1&1&1&1&1&1&1\\
0&1&0&0&0&0&0&0&0&0&0&0&0&0&0&0\\
0&1&2&3&0&0&0&0&0&0&0&0&0&0&0&0\\
0&1&0&0&0&1&0&0&0&1&0&0&0&1&0&0\\
0&1&2&3&0&1&2&3&0&1&2&3&0&1&2&3\\
0&0&0&0&1&0&0&0&0&0&0&0&0&0&0&0\\
0&0&0&0&1&1&1&1&0&0&0&0&0&0&0&0\\
0&0&0&0&1&0&0&0&2&0&0&0&3&0&0&0\\
0&0&0&0&1&1&1&1&2&2&2&2&3&3&3&3\\
0&0&0&0&0&1&0&0&0&0&0&0&0&0&0&0\\
0&0&0&0&0&1&2&3&0&0&0&0&0&0&0&0\\
0&0&0&0&0&1&0&0&0&2&0&0&0&3&0&0\\
0&0&0&0&0&1&2&3&0&2&4&6&0&3&6&9
\end{pmatrix}$$

It is fortunate that this matrix has a nice integer valued inverse. When $d = 3$ this procedure results in a matrix multiplication of rank 64 which is not printed here. This kind of operation might become faster when performed on a graphical processing unit.

Appendix E

About the code

The code supplies several smaller routines based on the same ”numerical tower”. The entire program is made in C++ with the exception of several helper scripts in Python (mainly used for file-format conversion). The software will be available under the GPL licence at `http://www.astro.rug.nl/~hidding`.